

OCEAN

ENGINEERING

GROUP

Numerical Modeling of
Supercavitating and Surface–Piercing Propellers

Yin Lu Young

May 2002

Report No. 02–1

ENVIRONMENTAL AND WATER RESOURCES ENGINEERING

DEPARTMENT OF CIVIL ENGINEERING

THE UNIVERSITY OF TEXAS AT AUSTIN

Austin, TX 78712

Copyright
by
Yin Lu Young
2002

The Dissertation Committee for Yin Lu Young
Certifies that this is the approved version of the following dissertation:

**Numerical Modeling of Supercavitating and Surface-Piercing
Propellers**

Committee:

Spyros A. Kinnas, Supervisor

John L. Tassoulas

Howard M. Liljestrang

David G. Bogard

Kamy Sepehrnoori

**Numerical Modeling of Supercavitating and Surface-Piercing
Propellers**

by

Yin Lu Young, B.S., M.S.

DISSERTATION

Presented to the Faculty of the Graduate School of
The University of Texas at Austin
in Partial Fulfillment
of the Requirements
for the Degree of

DOCTOR OF PHILOSOPHY

THE UNIVERSITY OF TEXAS AT AUSTIN

May 2002

Dedicated to my parents and my sister.

Acknowledgments

Although this dissertation bears my name, it would not have been possible to complete this work without the encouragement and guidance of many individuals. First and foremost, I would like to thank my advisor, Professor Spyros A. Kinnas. He patiently guided me and supported me through the entire length of this project. His enthusiasm, wisdom, and thoughtfulness inspired me to always put forth my very best.

I would also like to express my deepest gratitude to Professor John L. Tsoulas for his invaluable advice and endless support. I am also indebted to Professors Howard M. Liljestrand, David G. Bogard, and Kamy Sepehrnoori for their continuing assistance and encouragements.

Many thanks goes to Professors Jose M. Roesset and Kenneth H. Stokoe, II, for their recommendations and guidance.

A special thanks goes to Dr. Niclas Olofsson, who provided me with experimental data to verify my numerical predictions.

I would also like to thank all my friends at UT Austin for their friendship and assistance. In addition, I would like to recognize the support from the staff in the Civil Engineering Department at UT Austin.

Finally, I would like to thank all of the individuals and organizations who supported me in this work. They include:

- The National Science Foundation for the National Science Foundation Graduate Fellowship.
- The College of Engineering at The University of Texas at Austin and Mr. and Mrs. Ned Burns for the Burns/Fontaine Endowed Graduate Fellowship in Engineering.
- The University of Texas at Austin for the University Continuing Fellowship.
- Phase II and Phase III Members of the “Consortium on Cavitation Performance of High Speed Propulsors”: AB Volvo Penta, American Bureau of Shipping, David Taylor Model Basin, Daewoo Shipbuilding & Heavy Machinery, El Pardo Model Basin, Hyundai Maritime Research Institute, Wärtsilä Propulsion Norway AS, Kamewa AB, Michigan Wheel Corporation, Naval Surface Warfare Center Carderock Division, Office of Naval Research (contract no. N000140110225), Rolla SP Propellers SA, Ulstein Propeller AS, and VA Tech Escher Wyss GMBH.

Numerical Modeling of Supercavitating and Surface-Piercing Propellers

Publication No. _____

Yin Lu Young, Ph.D.

The University of Texas at Austin, 2002

Supervisor: Spyros A. Kinnas

A three-dimensional low-order potential-based boundary element method for the nonlinear analysis of unsteady sheet cavitation on fully submerged and partially submerged propellers subjected to time-dependent inflow is presented. The emphasis is placed on the modeling of supercavitating and surface-piercing propellers. The unsteady cavity surface is determined in the framework of a moving mixed boundary-value problem. For a given cavitation number, the extent and thickness of the cavity surface is determined in an iterative manner at each time step until both the prescribed pressure and flow tangency conditions are satisfied. The cavity detachment location is also determined in an iterative manner by satisfying the Villat-Brillouin smooth detachment condition. The current method is able to predict complex types of cavitation patterns on both sides of the blade surface, as well as the extent and thickness of the separated region behind non-zero thickness trailing edges. For surface-piercing propellers, the linearized free surface boundary condition is applied along with the assumption of infinite Froude number, both of

which are enforced by the negative image method. The method is shown to converge quickly with grid size and time step size. The predicted cavity planforms and propeller loadings also compare well with experimental observations and measurements. Finally, a 2-D study to investigate the effects of jet sprays at the moment of blade entry is presented.

Table of Contents

Acknowledgments	vi
Abstract	viii
List of Tables	xiv
List of Figures	xv
Nomenclature	xxi
Chapter 1. Introduction	1
1.1 Background	1
1.2 Motivation	9
1.3 Supercavitating Propellers	9
1.4 Surface-Piercing Propellers	10
1.5 Objectives	14
1.6 Organization	14
Chapter 2. Fully Submerged Cavitating Propellers	15
2.1 Previous Work	15
2.1.1 2-D Hydrofoil Flows	15
2.1.2 3-D Hydrofoil Flows	17
2.1.3 3-D Conventional Propeller Flows	18
2.1.4 3-D Supercavitating Propeller Flows	19
2.2 Objectives	21
2.3 Formulation	21
2.3.1 Fundamental Assumptions	22
2.3.2 Problem Definition	23
2.3.3 Green's Formula	25

2.3.4	Boundary Conditions	29
2.4	Numerical Implementation	36
2.4.1	Solution Algorithm	36
2.4.2	Split-Panel Technique	37
2.4.3	Cavity Detachment Search Criterion	39
2.5	Face and Back Cavitation	42
2.5.1	Numerical Algorithm	43
2.5.2	Numerical Validation	49
2.6	Supercavitating Propellers	54
2.6.1	Numerical Validation	60
2.7	Convergence Studies	67
2.7.1	Propeller DTMB N4148 - Traditional Propeller with Back Cavitation	67
2.7.2	Propeller SRI - Supercavitating Propeller	70
2.8	Validation with Experiments and other Numerical Methods	78
2.8.1	Propeller DTMB 5168 - Five Bladed, Highly-Skewed Propeller	78
2.8.2	Propeller DTMB 4119 - Three Bladed, Zero-Skew and Zero- Rake Propeller	79
2.8.3	Propeller DTMB 4148 - Three Bladed, Zero-Skew and Zero- Rake Propeller	81
2.8.4	Propeller 4382 - Five Bladed, Non-Zero Skew and Non-Zero Rake Propeller	83
2.8.5	Propeller SRI - Three Bladed, Non-Zero Skew and Non-Zero Rake Supercavitating Propeller	88
2.9	Results	91
2.10	Summary	94
 Chapter 3. Partially Submerged Propellers		97
3.1	Previous Work	97
3.1.1	Experimental Methods	97
3.1.2	Numerical Methods	99
3.2	Objectives	101
3.3	Formulation	101
3.3.1	Fundamental Assumptions	102

3.3.2	Green's Formula	103
3.3.3	Boundary Conditions	104
3.4	Numerical Implementation	108
3.4.1	Negative Image Method	108
3.4.2	Solution Algorithm	111
3.4.3	Ventilated Cavity Detachment Search Criterion	112
3.5	Convergence Studies	114
3.5.1	Convergence with Number of Revolutions	114
3.5.2	Convergence with Time Step Size	114
3.5.3	Convergence with Grid Size	115
3.6	Validation with Experiments	119
3.6.1	Summary of Experiment by Olofsson	119
3.6.2	Test Conditions Selected for Comparisons	121
3.6.3	Comparison of Numerical Predictions with Experimental Measurements	122
3.6.4	Discussion of Results	125
3.7	Summary	140

Chapter 4. Surface-Piercing Hydrofoils 141

4.1	Introduction	141
4.2	Objectives	143
4.3	Previous Work	143
4.4	Formulation	144
4.4.1	Problem Definition	144
4.4.2	Boundary Conditions	146
4.5	Numerical Implementation	149
4.5.1	Time-Integration Scheme	151
4.5.2	Pressure and Impact Force Calculation	153
4.6	Preliminary Results	154
4.6.1	Vertical Entry of a Symmetric Wedge	154
4.6.2	Oblique Entry of a Flat Plate	154
4.7	Summary	158

Chapter 5. Conclusions	159
5.1 Conclusions	159
5.2 Discussions and Recommendations	160
5.2.1 Alternating or Simultaneous Face and Back Cavitation	160
5.2.2 Supercavitating Propellers	161
5.2.3 Surface-Piercing Propellers	162
Vita	184

List of Tables

- 2.1 Approximate CPU time required on a COMPAQ DS20E with 2-833 MHz Processor (approximately 3-times as fast as an 1-GHz Pentium PC) for propeller SRI subjected to steady inflow. 3 blades. $J_A=1.3$. $\sigma_n=0.676$. $\Delta\theta = 6^\circ$. 8 cavitating revolutions. The comparisons of the cavity shape and cavitating forces for the different grid discretization are shown in Fig. 2.44. Taken from [Young et al. 2001b]. 96
- 2.2 Approximate CPU time required on a COMPAQ DS20E with 2-833 MHz Processor (approximately 3-times as fast as an 1-GHz Pentium PC) for propeller 4148 subjected to unsteady inflow. 3 blades. 3 blades. $J_s=0.954$. $\sigma_n=2.576$. $F_r=9.159$. 5 wetted revolutions and 6 cavitating revolutions. The comparisons of the cavity shape and cavitating forces for the different grid and time discretization are shown in Figs. 2.26 to 2.29. Taken from [Young et al. 2001b]. . . . 96

List of Figures

1.1	Saturated vapor pressure of water	2
1.2	Photograph of liquid jet formation during the collapse of a cavitation bubble. Taken from [Coleman 1987].	3
1.3	Photograph of a partial cavity on a 3-D hydrofoil. The experiment was conducted at MIT's Marine Hydrodynamics Water Tunnel. Taken from [Brewer and Kinnas 1997].	4
1.4	Photograph of a supercavity on a 3-D hydrofoil. The experiment was conducted at MIT's Marine Hydrodynamics Water Tunnel. Taken from [Kinnas and Mazel 1992].	5
1.5	Different types of cavitation on a marine propeller. Taken from [Kinnas 1998].	6
1.6	Graphical illustration of a supercavitating hydrofoil, a ventilated hydrofoil, and a surface-piercing hydrofoil.	8
1.7	Approximate maximum installed efficiency envelopes for different propellers. Taken from [Allison 1978].	12
2.1	Propeller subjected to a general inflow wake. The blade fixed (x, y, z) and ship fixed (x_s, y_s, z_s) coordinate systems are shown.	24
2.2	(a) Definition of the exact surface. (b) Definition of the approximated cavity surface	26
2.3	Definition of the cavity height on the blade and on the supercavitating wake.	33
2.4	An example showing how the cavity closure condition is satisfied for a 2-D hydrofoil. Left: Plot of predicted cavity shape for different guess of cavity length l . Right: Plot showing convergence of cavity trailing edge thickness δ with l . Taken from [Kinnas and Fine 1993].	35
2.5	Left: The split panel technique applied to the cavity trailing edge in 3-D. Right: The extrapolated values for $\partial\phi/\partial n$ into two parts of the split panel. Taken from [Kinnas and Fine 1993].	38
2.6	A graphical depiction of the cavity detachment search algorithm.	40
2.7	Application of the dynamic boundary condition on the face and the back of a cavitating blade section.	44

2.8	Extrapolation of the potential at the cavity leading edge on the face and the back of a cavitating blade section.	45
2.9	Schematic of cavity height calculation.	47
2.10	Top: Initial cavity shape for a 3-D hydrofoil section with detachment locations based on the shown wetted pressure distributions. Bottom: The converged cavity shape and cavity pressure distributions.	50
2.11	Cavitation patterns on conventional propellers which can be predicted by the present method.	51
2.12	Validation of simultaneous face and back cavitation on an asymmetric rectangular hydrofoil. 50X10 panels. $\alpha = \pm 0.3^\circ$. $f_o/C = \pm 0.018$ (NACA a=0.8). $\tau_o/C = 0.05$ (RAE). $\sigma_v = 0.15$	52
2.13	Validation of simultaneous face and back cavitation on an asymmetric rectangular hydrofoil. 50X10 panels. $\alpha = \pm 0.5^\circ$. $f_{max}/C = \pm 0.018$ (NACA a=0.8). $T_{max}/C = 0.05$ (NACA66). $\sigma_v = 0.08$	53
2.14	Treatment of supercavitating blade sections.	56
2.15	Application of the dynamic boundary condition for a supercavitating blade section.	57
2.16	Extrapolation of the potential at the blade trailing edge for a fully wetted or partially cavitating supercavitating blade section.	58
2.17	Pressure integration over a blade section with non-zero trailing edge thickness.	60
2.18	Cavitation patterns on supercavitating propellers that can be predicted by the present method.	61
2.19	Validation for treatment of blade sections with non-zero thickness subjected to fully wetted conditions. $\sigma_v=0.15$, $T_{max}/C=0.05$, $T_{TE}/C = 0.02$, $f_{max}/C=0$, $\alpha=0^\circ$. Uniform inflow.	62
2.20	Validation for treatment of blade sections with non-zero thickness subjected to partially cavitating conditions. $\sigma_v=0.10$, $T_{max}/C = 0.05$, $T_{TE}/C=0.02$, $f_{max}/C=0$, $\alpha=0^\circ$. Uniform inflow.	63
2.21	Validation for treatment of blade sections with non-zero thickness subjected to supercavitating conditions. $\sigma_v=0.07$, $T_{max}/C = 0.05$, $T_{TE}/C=0.02$, $f_{max}/C=0$, $\alpha=0^\circ$. Uniform inflow.	64
2.22	Validation for treatment of blade sections with non-zero thickness subjected to mixed cavitation patterns. $\sigma_v=0.11$, $T_{max}/C = 0.05$, $T_{TE}/C=0.02$, $f_{max}/C=\pm 0.02$, $\alpha=\pm 1^\circ$. Uniform inflow.	65

2.23	The influence of the closing zone length on the pressure and cavity shape for a supercavitating blade section. XSR is the ratio of the lengths of the closing zone and the chord. $NSR2$ is the number of panels on each side of the closing zone per each radial strip. $\sigma_v=0.15$, $T_{max}/C = 0.05$, $T_{TE}/C = 0.02$, $f_{max}/C=0$, $\alpha=0^\circ$. Uniform inflow.	66
2.24	Geometry and inflow wake of propeller DTMB4148.	68
2.25	Convergence of individual blade forces with number of propeller revolutions for propeller DTMB4148. 60x20 panels. $\Delta\theta = 6^\circ$. $\sigma_n = 2.576$. $J_s = 0.954$. $F_r = 9.159$	69
2.26	Convergence of cavitating blade force coefficients (per blade) with blade angle increments for propeller DTMB N4148. 60x20 panels. $\sigma_n = 2.576$. $J_s = 0.954$. $F_r = 9.159$	70
2.27	Convergence of cavity planforms with blade angle increments for propeller DTMB N4148. 60x20 panels. $\sigma_n = 2.576$. $J_s = 0.954$. $F_r = 9.159$	72
2.28	Convergence of cavitating blade force coefficients (per blade) with mesh size for propeller DTMB N4148. $\Delta\theta = 6^\circ$. $\sigma_n = 2.576$. $J_s = 0.954$. $F_r = 9.159$	73
2.29	Convergence of cavity planforms with mesh size for propeller DTMB N4148. $\Delta\theta = 6^\circ$. $\sigma_n = 2.576$. $J_s = 0.954$. $F_r = 9.159$	74
2.30	Left: Discretized propeller geometry. Right: Blade section and closing zone geometry. Propeller SRI. uniform inflow.	75
2.31	Convergence of thrust coefficient (per blade) with number of revolutions. Propeller SRI. $\sigma_n=0.784$. $J_s=1.4$. $F_r=5.0$. 3° inclination. 60x20 panels. $\Delta\theta = 6^\circ$	75
2.32	Convergence of thrust and torque coefficient (per blade) with blade angle increment. Propeller SRI. $\sigma_n=0.784$. $J_s=1.4$. $F_r=5.0$. 3° inclination. 70x30 panels.	76
2.33	Convergence of thrust and torque coefficient (per blade) with grid discretization. Propeller SRI. $\sigma_n=0.784$. $J_s=1.4$. $F_r=5.0$. 3° inclination. $\Delta\theta = 8^\circ$	77
2.34	Geometry of propeller DTMB5168. Also shown are the predicted and measured K_T and K_Q for different advance coefficients. PROPCAV: 80x60 Panels. MPUF-3A: 20x18 panels.	79
2.35	Geometry and inflow wake of propeller DTMB4119. Also shown are the predicted and measured K_T and K_Q for different blade harmonics. PROPCAV: 80x50 Panels. MPUF-3A: 40x27 panels	80
2.36	Comparison of PROPCAV's prediction (bottom) to experimental observations (top) for propeller DTMB4148. $J_s = 0.954$, $\sigma_n = 2.576$, $F_r = 9.159$, 70x30 panels, $\Delta\theta = 6^\circ$	82

2.37	Propeller DTMB 4382 with paneled blades, hub, and trailing wake.	84
2.38	Open water performance predicted by PROPCAV, MPUF3A, and measured in experiments by [Boswell 1971]	85
2.39	Predicted and measured thrust (K_T) and torque (K_Q) coefficients as a function of cavitation number (σ_v) at the design advance ratio ($J_A = 0.889$).	86
2.40	Predicted and measured thrust (K_T) and torque (K_Q) coefficients as a function of cavitation number (σ_v) and advance ratio (J_A).	87
2.41	Predicted cavity planform at $J_A = 0.7$ and $\sigma_v = 3.5$ by PROPCAV and MPUF3A.	87
2.42	Comparison of the predicted and versus measured K_T , K_Q , and η_p for different advance coefficients.	89
2.43	Predicted cavity shape and cavitating pressures for propeller SRI at $J_A = 1.3$. 50x20 panels. Uniform inflow.	89
2.44	Convergence of cavity shape and force coefficients with number of panels for $J_A = 1.3$. Uniform inflow.	90
2.45	Predicted cavity planforms at two different blade angles. Propeller SRI. $\sigma_n=0.784$. $J_s=1.4$. $F_r=5$. 3° inclination. 60x20 panels. $\Delta\theta = 6^\circ$. 92	
2.46	Predicted cavity pressure distributions for various radii at two different blade angles. Propeller SRI. $\sigma_n=0.784$. $F_r=5$. $J_s=1.4$. 3° inclination. 60x20 panels. $\Delta\theta = 6^\circ$	92
2.47	Predicted cavity pressure contours. Propeller SRI. $\sigma_n=0.784$. $J_s=1.4$. $F_r=5$. 3° inclination. 60x20 panels. $\Delta\theta = 6^\circ$	93
3.1	Definition of “exact” and approximated flow boundaries around a surface-piercing blade section	104
3.2	Reduction of the cross-flow term in the kinematic boundary condition on the ventilated blade cavity surface, $S_{CB}(t)$	106
3.3	Linearized free surface boundary condition and the infinite Froude number assumption.	107
3.4	Schematic example of the negative image method on a partially submerged blade section.	109
3.5	Graphic illustration of ventilated cavity patterns that satisfy the cavity detachment condition on a partially submerged blade section. In addition, the cavities are assumed to vent to the atmosphere.	113
3.6	Convergence of thrust (K_T) and torque (K_Q) coefficients (per blade) with number of revolutions. Propeller model 841-B. $J_A = 1.2$. 70x30 panels. $\Delta\theta = 6^\circ$	116

3.7	Convergence of thrust (K_T) and torque (K_Q) coefficients (per blade) with time step size. Propeller model 841-B. $J_A = 1.2$. 70x30 panels. 6 propeller revolutions.	117
3.8	Convergence of thrust (K_T) and torque (K_Q) coefficients (per blade) with panel discretization. Propeller model 841-B. $J_A = 1.2$. $\Delta\theta = 6^\circ$. 6 propeller revolutions.	118
3.9	Photograph of propeller model 841-B shown in [Olofsson 1996], with corresponding BEM model on the right.	119
3.10	The data and outline of the KaMeWa free surface cavitation tunnel. Taken from [Olofsson 1996].	127
3.11	The flexure-unit used to measure the reaction load. Taken from [Olofsson 1996].	127
3.12	Test conditions that simultaneously satisfy cavitation and Froude number scaling. Note that the non-dimensional constants are defined as follows: $F_{nD} = V/\sqrt{gD}$. $\sigma = \sigma_v = (P_o - P_v)/(0.5\rho V^2)$. $R_n = nD^2/\nu$. $W_n = nD/\sqrt{\sigma_k/\rho D}$. σ_k is the capillarity constant of water, and $V = V_A$. Taken from [Olofsson 1996].	128
3.13	Axial velocity distribution at the propeller plane. Propeller model 841-B. $h/D = 0.33$. Reproduced from a similar figure presented in [Olofsson 1996].	129
3.14	Blade section geometry of propeller model 841-B. Note that the fish tail design at the blade trailing edge is to facilitate backing conditions.	130
3.15	Predicted pressure contours for $J_A = 0.8$. Propeller model 841-B. 4 Blades. $h/D = 0.33$. 60x20 panels. $\Delta\theta = 6^\circ$	131
3.16	Predicted ventilated cavity patterns for $J_A = 0.8$. Propeller model 841-B. 4 Blades. $h/D = 0.33$. 60x20 panels. $\Delta\theta = 6^\circ$	132
3.17	Comparison of predicted (P) and measured (E) blade forces for $J_A = 0.8$. Propeller model 841-B. 4 Blades. $h/D = 0.33$. 60x20 panels. $\Delta\theta = 6^\circ$	133
3.18	Predicted pressure contours for $J_A = 1.0$. Propeller model 841-B. 4 Blades. $h/D = 0.33$. 60x20 panels. $\Delta\theta = 6^\circ$	134
3.19	Comparison of predicted (P) and measured (E) blade forces for $J_A = 1.0$. Propeller model 841-B. 4 Blades. $h/D = 0.33$. 60x20 panels. $\Delta\theta = 6^\circ$	135
3.20	Comparison of the observed (top) and predicted (bottom) ventilated cavity patterns for $J_A = 1.2$. Propeller model 841-B. 4 Blades. $h/D = 0.33$. 60x20 panels. $\Delta\theta = 6^\circ$	136
3.21	Comparison of the observed (top) and predicted (bottom) ventilated cavity patterns for $J_A = 1.2$. Propeller model 841-B. 4 Blades. $h/D = 0.33$. 60x20 panels. $\Delta\theta = 6^\circ$	137

3.22	Comparison of the observed (top) and predicted (bottom) ventilated cavity patterns for $J_A = 1.2$. Propeller model 841-B. 4 Blades. $h/D = 0.33$. 60x20 panels. $\Delta\theta = 6^\circ$	138
3.23	Comparison of predicted (P) and measured (E) blade forces for $J_A = 1.2$. Propeller model 841-B. 4 Blades. $h/D = 0.33$. 60x20 panels. $\Delta\theta = 6^\circ$	139
4.1	Planned progression of the 2-D nonlinear study for the water entry and exit problem of a surface-piercing hydrofoil.	142
4.2	Definition of coordinate system and control surface for the water entry problem of a 2-D rigid hydrofoil.	148
4.3	A schematic representation of the known and unknown for the 2-D rigid foil entry problem.	150
4.4	Predicted free surface elevation and pressure distribution during water entry of a 2-D wedge. $\alpha = 9^\circ$	155
4.5	Pressure distribution on the wetted body surface predicted by the present method and by the method of [Savineau and Kinnas 1995]. Flat plate. $\alpha = 5^\circ$	156
4.6	Pressure distribution on the wetted body surface predicted by the present method and by the method of [Savineau and Kinnas 1995]. Flat plate. $\alpha = 8^\circ$	157

Nomenclature

Latin Symbols

C_p	pressure coefficient, $C_p = (P - P_o)/(0.5\rho n^2 D^2)$
D	propeller diameter, $D = 2R$
f_{max}/C	maximum camber to chord ratio
F_{nD}	Froude number based on V_A , $F_{nD} = V_A/\sqrt{gD}$
F_r	Froude number based on n , $F_r = n^2 D/g$
g	gravitational acceleration
G	Green's function
h	cavity thickness over the blade surface, or blade tip immersion for partially submerged propellers
h_{sr}	cavity thickness over the separated region
h_w	cavity thickness over the wake surface
J_A	advance ratio based on V_A , $J_a = V_A/nD$
J_s	advance ratio based on V_s , $J_s = V_s/nD$
K_{Fx}, K_{Fy}, K_{Fz}	dynamic blade force coefficients in ship fixed coordinates
K_{Mx}, K_{My}, K_{Mz}	dynamic blade moment coefficients in ship fixed coordinates
K_Q	torque coefficient, $K_Q = Q/\rho n^2 D^5$
K_T	thrust coefficient, $K_T = T/\rho n^2 D^4$

l	cavity length
l_{sr}	separated region length
n	propeller rotational frequency (rev/s)
P	pressure
P_{atm}	atmospheric pressure
P_o	pressure far Upstream, at the propeller axis
P_v	vapor pressure of water
\vec{q}	total velocity
\vec{q}_c	total cavity velocity
\vec{q}_{in}	local inflow velocity (in the propeller fixed system)
\vec{q}_w	wake inflow velocity (in the ship fixed system)
Q	propeller torque
r	radius of propeller blade section
R	propeller radius
R_n	Reynolds number, $R_n = nD^2/\nu$
$\vec{s}, \vec{v}, \vec{n}$	non-orthogonal unit vectors along the local grid directions
S_B	blade surface, $S_B = S_{CB} + S_{WB}$
S_C	cavitating surface, $S_C = S_{CB} + S_{CW}$
S_{CB}	cavitating portion of blade surface
S_{CW}	cavitating portion of wake surface
S_F	free surface
S_∞	infinite boundary surface for foil entry problem
S_{WB}	wetted portion of blade surface
S_W	wake surface

t	time
T	propeller thrust
T_{max}/C	maximum thickness to chord ratio
T_{TE}/C	trailing edge thickness to chord ratio
\vec{V}	velocity of 2-D surface-piercing hydrofoil
V_A	advance speed of propeller, or inflow speed for 3-D hydrofoil
V_s	ship speed
W_n	Webber number, $W_n = nD/\sqrt{\sigma_k/\rho D}$
x, y, z	propeller fixed coordinates
x_s, y_s, z_s	ship fixed coordinates
XSR	separated region length to chord ratio

Greek Symbols

α	angle of attack for 3-D hydrofoil
β	shaft yaw angle
η	vertical coordinate of free surface
δ	cavity trailing edge thickness
δ_{sr}	separated region trailing edge thickness
Δt	time step size
$\Delta\theta$	blade angle increment, $\Delta\theta = \omega\Delta t$
η_p	propeller efficiency, $\eta_p = \frac{K_T J_s}{K_Q 2\pi}$
γ	shaft inclination angle
λ	ratio of full-scale diameter to model-scale diameter
ω	propeller angular velocity
ν	kinematic viscosity of water
ϕ	perturbation potential
Φ	total potential
ψ	angle between \vec{s} and \vec{v}
ρ	fluid density
σ_k	capillarity constant of water
σ_n	cavitation number based on n , $\sigma_n = (P_o - P_v)/(0.5\rho n^2 D^2)$
σ_v	cavitation number based on V_A , $\sigma_v = (P_o - P_v)/(0.5\rho V_A^2)$
ζ	horizontal coordinate of free surface

Superscripts

- + upper cavity, separated region, or wake surface
- lower cavity, separated region, or wake surface

Acronyms

BEM	boundary element method
CPU	central processing unit (time)
DTMB	David Taylor Model Basin
MIT	Massachusetts Institute of Technology
NACA	National Advisory Committee for Aeronautics
RAE	foil sections designed by [Treadgold et al. 1979]
VLM	vortex-lattice method

Computer Program Names

MPUF-3A	cavitating propeller potential flow solver based on VLM
PROPCAV	cavitating propeller potential flow solver based on BEM

Chapter 1

Introduction

1.1 Background

The word *Cavitation* derives from its Latin origin *cavus*, which means hollow. It is defined in Merriam-Webster's Dictionary as the formation of partial vacuums in a liquid by a swiftly moving solid body (hydrodynamic cavitation) or by high-intensity sound waves (acoustic cavitation). This research studies the effect of hydrodynamic cavitation, which occurs when pressure drops below the saturated vapor pressure, consequently resulting in the formation of gas filled or gas and vapor filled bubbles (or cavities) [Batchelor 1967]. A common phenomenon known as *boiling* also describes the phase change from liquid to vapor. Boiling is different from cavitation in that it is driven by increase in temperature, instead of decrease in pressure. To help explain the difference between boiling and cavitation, the saturated vapor pressure curve for water is shown in Fig. 1.1.

Cavitation can occur in any hydrodynamic device that operates in liquid. Cavities form in areas of low pressure and are often harmless. However, serious structural damage and/or decrease in device efficiency may occur when the cavities collapse. During the collapse, a long thin jet (shown in Fig. 1.2) with velocity between 100 and 200 m/s develops and directs toward the solid surface it is in

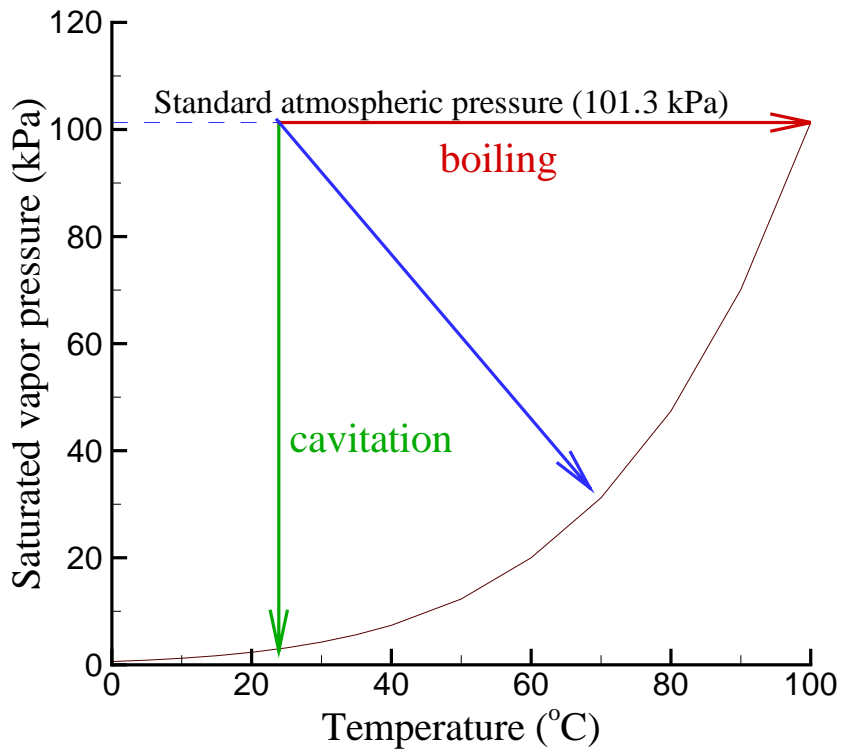


Figure 1.1: Saturated vapor pressure of water

contact with [Lauterborn and Bolle 1975]. If this action is continuous and with high frequency, it can damage even high quality steel.

The effect of cavitation on propellers was first investigated by [Reynolds 1873] in the laboratory, and by [Parson 1897] and [Barnaby 1897] using full scale trials of the destroyer *Daring*. They found that the formation of vapor bubbles on the blades reduced the power of the propeller. Later investigators also found that cavitation can lead to undesirable effects such as blade surface erosion, increased

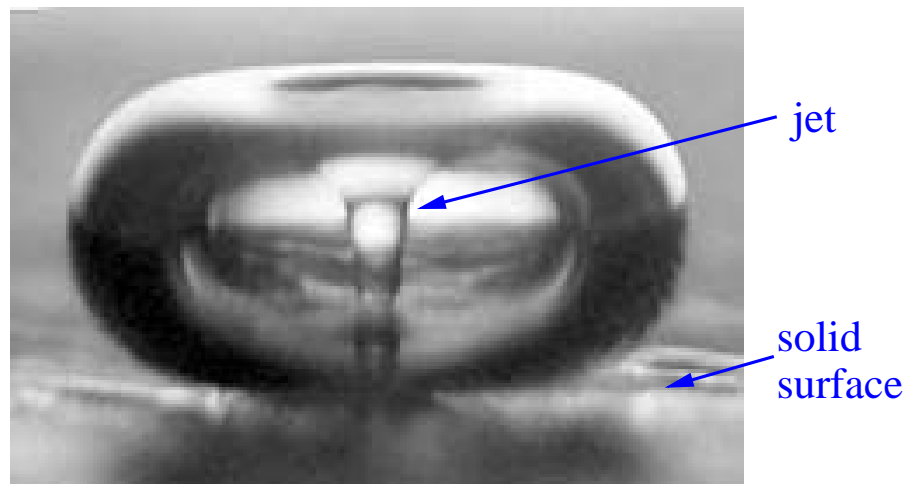


Figure 1.2: Photograph of liquid jet formation during the collapse of a cavitation bubble. Taken from [Coleman 1987].

hull pressure fluctuations and vibrations, acoustic energy radiation, and blade vibration. Thus, in the past, the goal in the design of propellers was to avoid cavitation. However, as stated in [Allison 1978], few propellers in practice can operate entirely without cavitation due to the non-axisymmetric inflow or unsteady body motion. Furthermore, propellers without cavitation would need to be larger and slower than necessary [Allison 1978]. Application of cavitation-resistant propeller materials (e.g. titanium alloys or stainless steels) or coatings (e.g. elastomeric covering systems or epoxide formulations) can be used to reduce cavitation and erosion damage [Angell et al. 1979; Allison 1978; Foster 1989]. Nevertheless, the presence of cavitation is difficult to avoid at very high speeds. Thus, the development of reliable, versatile, and robust computational tools to predict propeller cavitation for general blade geometries is crucial to the design and assessment of marine propulsors.

A type of cavitation that is very common on marine propulsors is *sheet* cavitation . It is characterized by a “continuous” liquid/vapor interface which is “attached” to the blade surface. Sheet cavitation is further divided into two main categories: partial cavitation and supercavitation. A *partial cavity* is a cavity that is shorter than the chord length of the blade, such as shown in Fig. 1.3. A *supercavity* , on the other hand, is a cavity that is longer than the chord length of the blade, such as shown in Fig. 1.4. Other types of cavitation which can also occur include cloud and bubble cavitation. Tip and hub vortex cavitation are also very common for propellers. A schematic drawing of the different types of cavitation is shown in Fig. 1.5. A general description on the different types of cavitation can be found in [Kato 1996].

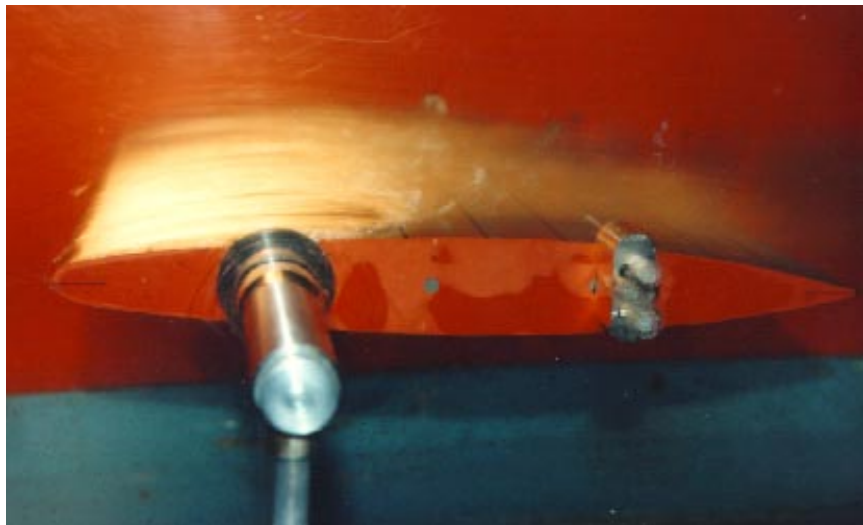


Figure 1.3: Photograph of a partial cavity on a 3-D hydrofoil. The experiment was conducted at MIT’s Marine Hydrodynamics Water Tunnel. Taken from [Brewer and Kinnas 1997].

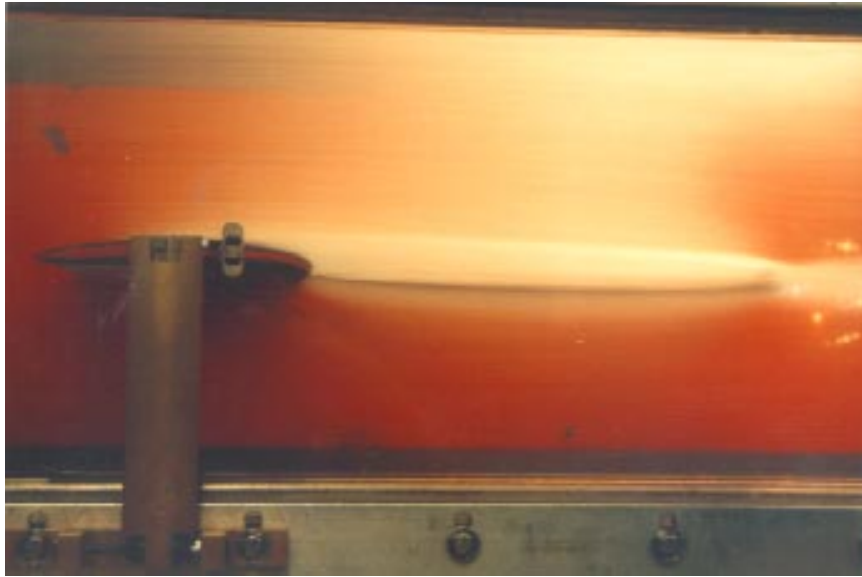


Figure 1.4: Photograph of a supercavity on a 3-D hydrofoil. The experiment was conducted at MIT's Marine Hydrodynamics Water Tunnel. Taken from [Kinnas and Mazel 1992].

In this work, the cavity on a propeller blade is treated strictly as sheet cavitation. The pressure inside the sheet cavity is assumed to be constant and equal to the vapor pressure. The rationale behind using the sheet cavity model include:

- It provides a relatively simple mathematical model where potential flow theory can be applied;
- [Tulin 1980] found that sheet cavity is the first-order contributor to dynamically varying blade loads; and
- Other forms of cavitation (such as tip or hub vortex cavitation) and other neglected phenomena (such as wake roll-up) can be added as refinements to

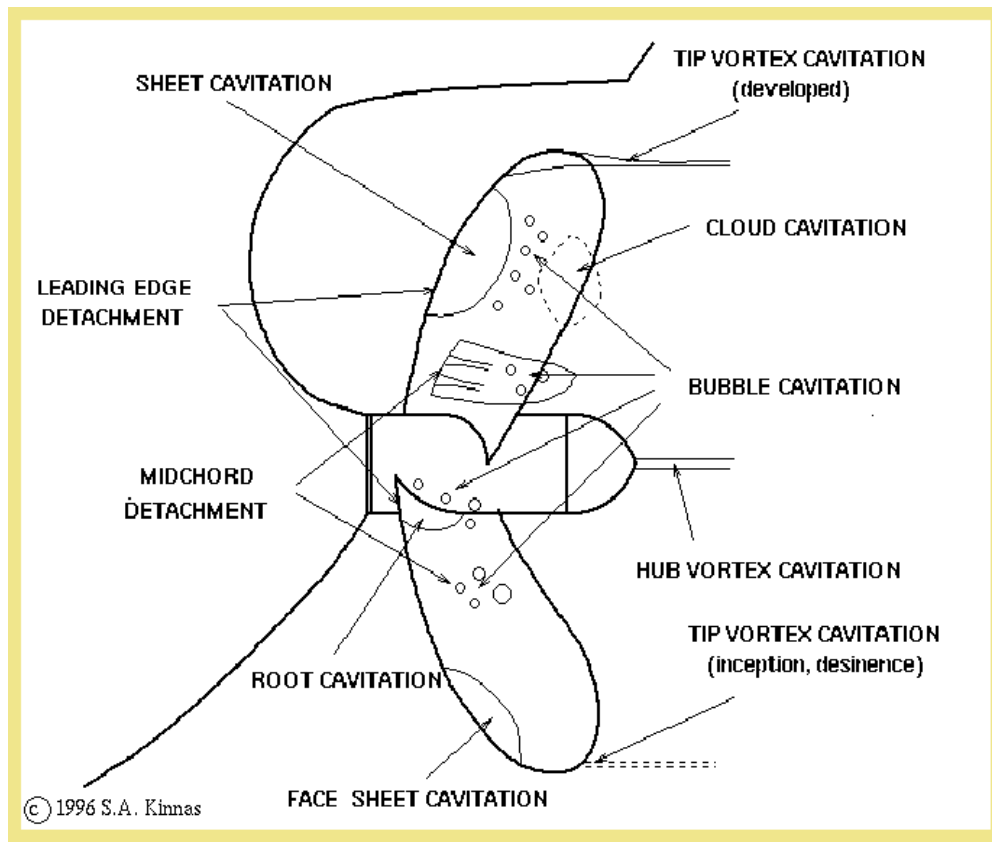


Figure 1.5: Different types of cavitation on a marine propeller. Taken from [Kinnas 1998].

the current model.

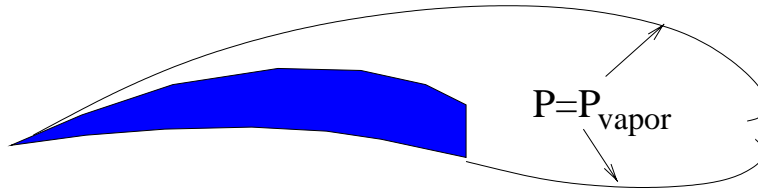
The main difficulty in the analysis of sheet cavitation is in determining the cavity surface (i.e. free streamline) where the pressure is prescribed. The problem is nonlinear because the extent and thickness of the cavity is unknown. In this work, the cavity surface is determined in the framework of a moving mixed boundary-value problem. For a given cavitation number, the extent and thickness of the cavity

surface at a given time step is determined in an iterative manner until both the prescribed pressure and flow tangency condition are satisfied.

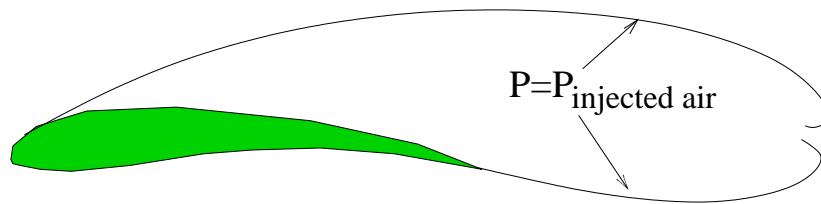
In addition to cavitation, another common phenomena for hydrofoils and propellers is *ventilation*. Ventilation occurs when surface air or exhaust gases are drawn into the lifting surface. To help explain the difference between cavitation and ventilation, a schematic diagram showing a supercavitating hydrofoil, a ventilated hydrofoil¹, and a surface-piercing hydrofoil is presented in Fig. 1.6. Notice that the pressure on the ventilated surface is constant but equal to a value that is different from the vapor pressure. Therefore, the ventilated surface can be modeled like a cavity surface but with a different prescribed pressure. Moreover, the same method can be used to determine the flow detachment locations, as well as the extent and thickness of the ventilated surfaces.

¹A system where air is continuously injected to the upper foil surface to force ventilation. The objective is to increase the lift to drag ratio at high-speeds.

a) supercavitating hydrofoil



b) ventilated hydrofoil



c) surface-piercing hydrofoil

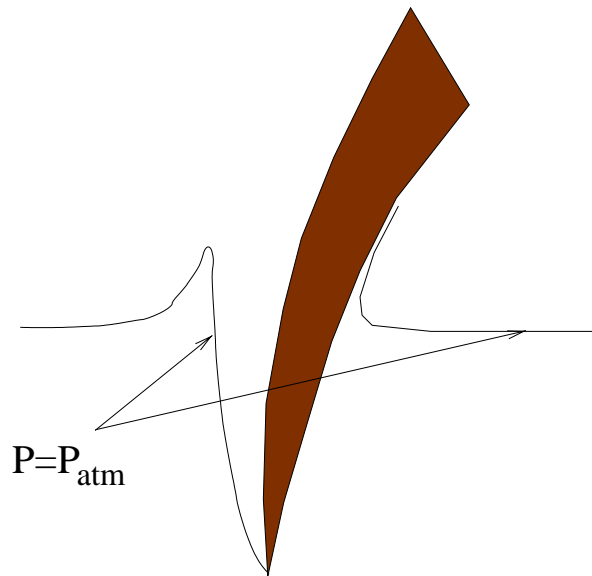


Figure 1.6: Graphical illustration of a supercavitating hydrofoil, a ventilated hydrofoil, and a surface-piercing hydrofoil.

1.2 Motivation

The motivation for this research is to develop a robust, reliable, and computationally efficient tool to predict unsteady sheet cavitation on fully submerged and partially submerged propellers subjected to time-dependent inflow. The emphasis is placed on the modeling of supercavitating or surface-piercing propellers.

1.3 Supercavitating Propellers

For conventional subcavitating propellers², the speed limit is approximately 20-25 knots. They do not perform well at higher speeds because considerable amount of cavitation is unavoidable. Furthermore, high shaft inclination is necessary for subcavitating propellers to accommodate the large diameter or provide propulsion for hydrofoil boats. Consequently, the drag of the exposed shaft and struts increases with increasing speed [Allison 1978]; the propeller generates a force normal to its shaft, which will significantly reduce the thrust of the propeller in the direction of boat advance [Peck and H. 1974]; and the extra upward velocity component in the inflow leads to periodic fluctuations in angle of attack, which worsens cavitation damage [Kehr 1999].

Supercavitating propellers, on the other hand, operate in fully cavitating conditions. They are characterized by very sharp leading edges and very blunt trailing edges. Supercavitating propellers are often believed to be the most fuel efficient propulsive device for high speed vessels. Major advantages in comparison

²A subcavitating propeller is a propeller without any cavitation

to conventional subcavitating or partially cavitating propellers include:

- reduction in viscous drag due to the un-wetted suction side as a result of the supercavity, and
- reduction in noise and blade surface erosion as a result of smaller volume change and cavities that collapse downstream of the blade trailing edge.

Supercavitating propellers were first used for racing motor-boats and have been used in hydroplanes since early 1900's [Allison 1978]. However, most designs were based on experience, and their action were little understood until theoretical investigations initiated by Tulin [Tulin 1962]. Following his work, [Tachmindji and Morgan 1958] developed the first design method of supercavitating propellers. However, improvements on supercavitating propellers have been slow due to the unknown physics following the blunt trailing edge. In the present days, original supercavitating propellers are not as commonly used compared to their modifications such as surface-piercing propellers [Achkinadze and Fridman 1995]. This is in part due to the fact that supercavitating propellers are still exposed to increasing appendage drag as speed increases.

1.4 Surface-Piercing Propellers

A surface-piercing (also called partially submerged) propeller is a special type of supercavitating propeller which operates at partially submerged conditions. Surface-piercing propellers are more efficient than submerged supercavitating propellers because:

1. Reduction of appendage drag due to shafts, struts, propeller hub, etc.;
2. Larger propeller diameter since its size is not limited by the blade tip clearance from the hull or the maximum vessel draft;
3. Reduction of blade surface friction and erosion since cavitation is replaced by ventilation ³.

A comparison of the maximum installed efficiency for different propulsors (taken from [Allison 1978]) is shown in Fig. 1.7. According to [Hadler and Hecker 1968], the first U.S. patent for a surface-piercing propeller was issued in 1869 to C. Sharp of Philadelphia. It was designed for shallow-draft boat propulsion. As time progressed, surface-piercing propellers were also used for hydroplane boats, and later for high-speed surface effect ships [Allison 1978]. In 1976, a large scale experiment, U.S. Navy SES-100B, confirmed that partially submerged propellers can achieve efficiencies comparable to fully submerged propellers [Allison 1978]. That experiment involved the use of an 100-ton surface effect ship propelled by two partially submerged controllable-pitch propellers at speeds up to 90 knots [Allison 1978]. Due to the superior propulsive characteristics of surface-piercing propellers, they are extensively used today in offshore racing, where speeds often exceed 100 knots [Olofsson 1996]. Recently, the commercial marine industry have shown an increased interest for large surface-piercing propellers. They are to be used in the next generation ferries with service speeds in the range of 70 to 80 knots at shaft

³Ventilation refers to air entering the blade area due to the presence of the free surface.

powers of about 20 MW [Olofsson 2001]. Hence, there is a high demand from the marine industry to develop a reliable method that can predict the performance of surface-piercing propellers.

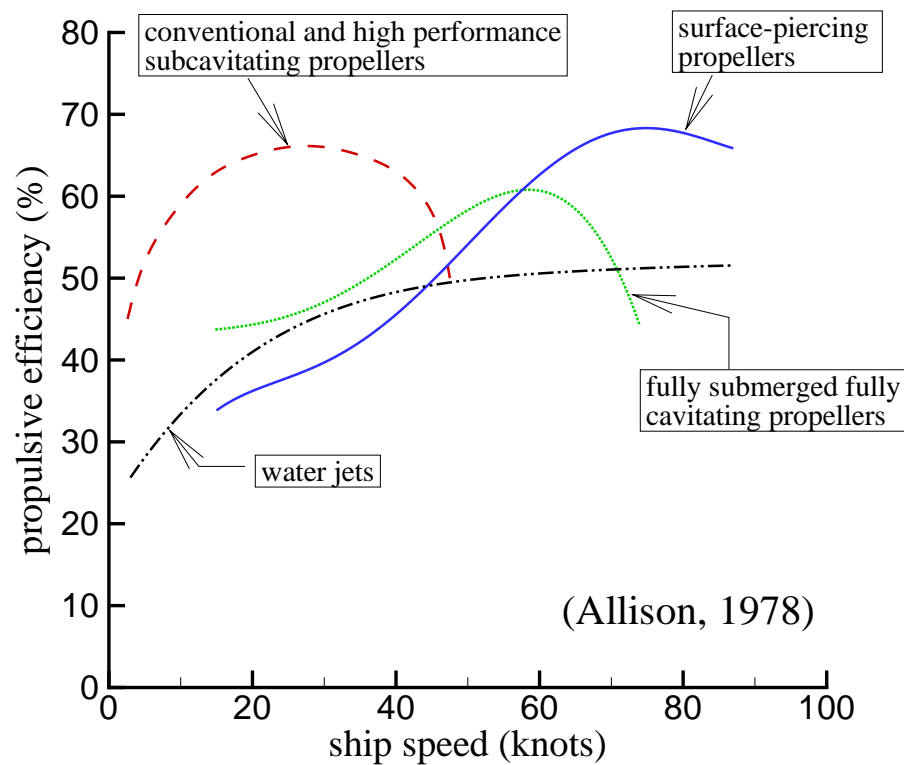


Figure 1.7: Approximate maximum installed efficiency envelopes for different propellers. Taken from [Allison 1978].

In the past, the design of surface-piercing propellers often involved trial-and-error procedures using measured performance of test models in free-surface tunnels or towing tanks. However, most of the trial-and-error approaches do not

provide information about the dynamic blades loads nor the average propeller forces [Olofsson 1996]. Model tests are extremely expensive, and often hampered by scaling effects [Shen 1975] [Scherer 1977] and influenced by test techniques [Morgan 1966] [Suhrbier and Lecoffre 1986]. Numerical methods, on the other hand, were not able to model the real phenomena. Difficulties in modeling surface-piercing propellers include:

- Insufficient understanding of the physical phenomena at the blade's entry to, and exit from, the free surface.
- Insufficient understanding of the dynamic loads accompanying a propeller piercing the water at high speed.
- The modeling of very thick and very long ventilated cavities, which are also interrupted by the free surface.
- The modeling of water jets and associated change in the free surface elevations at the time of the blade's entry to, and exit from, the free surface.
- The effect of blade vibrations due to the cyclic loading and unloading of the blades associated with the blade's entry to, and exit from, the free surface.

1.5 Objectives

The objective of this research is to extend a 3-D boundary element method, which has been developed in the past for the prediction of unsteady partial back cavitation on conventional fully submerged propellers, to predict the performance of supercavitating and surface-piercing propellers.

1.6 Organization

This dissertation is organized into five parts: introduction (Chapter 1), fully submerged propellers (Chapter 2), partially submerged propellers (Chapter 3), surface-piercing hydrofoils(Chapter 4), and conclusions (Chapter 5). A review of previous works, formulation, numerical implementation, convergence and validation studies, and results are first presented for fully submerged propellers in Chapter 2, and then for partially submerged propellers in Chapter 3. A systematic 2-D study of surface-piercing hydrofoils using the exact free surface boundary conditions is presented in Chapter 4. Summaries are also provided at the ends of Chapters 2 to 4. Finally, the overall summary, discussions, conclusions, and recommendations for future research are presented in Chapter 5.

Chapter 2

Fully Submerged Cavitating Propellers

2.1 Previous Work

This section presents a brief review of the development of numerical methods for the analysis of fully submerged propellers. It is divided into four subsections: 2-D hydrofoil flows, 3-D hydrofoil flows, 3-D conventional propeller flows, and 3-D supercavitating propeller flows.

2.1.1 2-D Hydrofoil Flows

- *Hodograph Technique*

Cavitating, or free-streamline, flows were first investigated in nonlinear theory by [Birkhoff and Zarantonello 1957]. Exact solutions for flows around two-dimensional (2-D) bodies at zero cavitation number were obtained using the hodograph technique. The method was extended to treat arbitrary geometries by [Wu and Wang 1964]. It was also applied to the analysis of supercavitating hydrofoils in the presence of a free surface by [Furuya 1975a].

- *Linear Cavity Theory*

A linearized theory for the analysis of 2-D cavity flows around general geometries at zero and non-zero cavitation number was introduced by [Tulin 1953,

1955]. It assumed the thickness of the cavity and the foil to be thin relative to the foil chord length, and applied boundary conditions on the projected foil surface along the free-stream axis. The method was also applied to partially cavitating hydrofoil flows by [Acosta 1955; Geurst and Timman 1956]. However, it predicted that the cavity extent and thickness should increase with increasing foil thickness under the same flow conditions, which is contrary to experimental evidence. To account for the breakdown of linear cavity theory, a nonlinear leading edge correction was introduced by [Kinnas 1985, 1991].

● *Boundary Element Methods*

Due to the above mentioned defect of linear cavity theory, various boundary element methods (BEMs) have emerged. Velocity-based BEMs include those developed by [Uhlman 1987; Lemonnier and Rowe 1988] for partially cavitating hydrofoils, and by [Uhlman 1989; Pellone and Rowe 1981] for supercavitating hydrofoils. They all assumed the cavity extent to be known, and solved for the unknown cavitation number and cavity thickness in an iterative matter. The process involved applying the dynamic boundary condition on the approximate cavity surface and using the kinematic boundary condition to update the cavity surface. A potential-based BEM with a similar iterative scheme was introduced by [Kinnas and Fine 1990] for partially and supercavitating hydrofoils. It demonstrated much faster convergence characteristics than velocity-based BEMs. In particular, the solution from the first nonlinear iteration where the cavity panels are placed on the foil surface beneath the cavity was found to be very close to the converged nonlinear solution [Kinnas and Fine 1990].

2.1.2 3-D Hydrofoil Flows

- *Strip-Theory*

The flow around 3-D cavitating hydrofoils was first addressed in strip-theory by [Nishiyama 1970; Leehey 1971; Furuya 1975b; Uhlman 1978; Van Houten 1982]. Analytical solutions were obtained by matching the inner solution (from either linear or non-linear theory) with the solution from lifting line theory in the outer domain. However, this method is only applicable for hydrofoils with high aspect ratios.

- *Lifting Surface Methods*

In [Widnall 1966], a pressure doublet and source lifting surface technique was introduced for the study of 3-D flow effects on supercavitating hydrofoils. Later, [Jiang and Leehey 1977] employed a vortex and source lattice lifting surface method (VLM) to determine the cavity planform on supercavitating hydrofoils. He also introduced an iterative scheme to determine the extent of the cavity by requiring the cavitation number to be constant in both span-wise and chord-wise directions.

- *Boundary Element Methods*

Velocity-based [Pellone and Rowe 1981] and potential-based [Kinnas and Fine 1993] BEMs were also extended to treat cavitating 3-D hydrofoils. In addition to faster convergence, the potential based BEM developed by [Kinnas and Fine 1993] was also able to predict mixed (partial and super) cavitation patterns on 3-D hydrofoils. Similar techniques were also developed by [Lee et al. 1992] for steady inflows and by [Kim et al. 1994; Pellone and Peallat 1995] for unsteady inflows.

2.1.3 3-D Conventional Propeller Flows

• *Vortex-Lattice Methods*

A VLM was first applied for the analysis of unsteady, fully wetted propeller flows by [Kerwin and Lee 1978]. It was later extended to treat partial sheet cavitation by [Lee 1979] [Breslin et al. 1982]. However, the method cannot capture the effect of blade thickness on cavities due to the application of the linearized boundary conditions. Thus, [Kerwin et al. 1986] implemented the leading edge correction introduced by [Kinnas 1985, 1991] to the VLM, and named the propeller code PUF-3A. The method placed vortex and source lattices on the mean camber surface¹ and applied a robust arrangement of singularities and control point spacings to produce accurate results [Kinnas and Fine 1989]. Recently, the method has been re-named MPUF-3A for its added ability to search for midchord cavitation² [Griffin et al. 1998] [Kosal 1999] [Lee and Kinnas 2001b]. The latest version of MPUF-3A [Lee et al. 2001] also includes the effect of hub, simplified wake alignment using circumferentially averaged velocities, arbitrary shaft inclination [Kinnas and Pyo 1999], and non-linear thickness-loading coupling [Kinnas 1992]. However, flow details at the blade leading edge and tip cannot be captured accurately due to the breakdown of either the linear cavity theory or the employed leading edge and thickness-loading coupling corrections. In addition, the current version of MPUF-3A does not include the effect of cavity sources in the thickness-loading coupling

¹Camber is a measure of the curvature of hydrofoil. The mean camber surface is an imaginary surface which lies halfway between the upper and lower surface of the blade.

²Midchord cavities refer to cavities that detach aft of the blade leading edge.

to correctly model the effect of cavitation.

- *Boundary Element Method*

The potential-based BEM developed by [Kinnas and Fine 1990, 1993] was extended to predict mixed cavitation patterns on the back of propeller blades subjected to non-axisymmetric inflows [Fine 1992; Kinnas and Fine 1992; Fine and Kinnas 1993]. The time-dependent cavities were assumed to detach at the blade leading edge, and a wake alignment similar to that of MPUF-3A [Greeley and Kerwin 1982] was applied. The method, named PROPCAV, places constant strength panels on the actual blade and hub surfaces. Thus, PROPCAV inherently includes the effect of nonlinear thickness-loading coupling and provides a more realistic hub model than MPUF-3A³. Similar BEMs were also developed by [Kim and Lee 1996; Caponnetto and Brizzolara 1995]. Recently, [Mueller and Kinnas 1997; Mueller 1998; Mueller and Kinnas 1999] further extended PROPCAV to predict midchord cavitation on either the back or the face of propeller blades.

2.1.4 3-D Supercavitating Propeller Flows

- *Lifting Line & Lifting Surface Methods*

The development of numerical methods for the analysis and design of supercavitating propellers has been slow compared to conventional propellers. The main difficulty arises from the unknown physics in the highly turbulent region (also called the *separated region*) behind the blunt trailing edge, which is characteristic

³MPUF-3A includes the hub effect via a simplified image model which assumes the hub to be of constant radius and infinite length.

of supercavitating propeller sections. The first theoretical design method was developed by [Tachnidji and Morgan 1958], and followed by [Tulin 1962; Venning and Haberman 1962; Cox 1968; Barr 1970; Yim and Higgins 1975; Yim 1976]. However, these methods were based on 2-D studies, and required many approximations and empirical corrections. Recently, more rigorous methods were developed by [Kamiirisa and Aoki 1994; Kikuchi et al. 1994; Vorus and Mitchell 1994; Ukon et al. 1995]. Nevertheless, these methods were still based on the optimization of 2-D cavitating blade sections to yield minimal drag for a given lift and cavitation number.

A 3-D vortex-lattice method was developed by [Kudo and Ukon 1994] to predict the steady performance of supercavitating propellers. Their model assumed the pressure over the separated zone to be constant and equal to the vapor pressure. Later, Kinnas extended MPUF-3A [Lee and Kinnas 2001b] to allow for a variable length separated zone model where the pressure is determined as part of the solution [Kudo and Kinnas 1995]. They found that the length of the separated zone had no effect on the results if all the blade sections were covered by the supercavity. However, the length of the separated zone did have an effect on the pressure and cavity length near the blade trailing edge under fully wetted and partially cavitating conditions. Finally, [Kinnas et al. 1999] further extended the method to search for midchord cavitation, and coupled it with an optimization method [Mishima and Kinnas 1997] for the design of supercavitating propellers.

However, all of the above mentioned lifting surface methods cannot capture accurately the flow details at the blade leading and trailing edges due to the break-

down of linear cavity theory. In addition, the applicability of the thickness-loading coupling introduced by [Kinnas 1992] in the analysis of supercavitating propellers is still under investigation.

2.2 Objectives

For fully submerged propellers, the first objective of this work is to extend PROPCAV (an existing potential-based BEM mentioned in preceding sections) to predict mixed cavitation patterns on both sides of the blade surface subject to steady and unsteady inflows. The second objective is to extend PROPCAV to predict the performance of supercavitating propellers in fully wetted, partially cavitating, or supercavitating conditions subject to steady and unsteady inflows.

2.3 Formulation

In this work, a 3-D potential based BEM is used for the numerical modeling of supercavitating and surface-piercing propellers. At each time step, a Fredholm integral equation of the second kind is solved with respect to the perturbation potential. A Dirichlet type boundary condition is applied on the cavitating surfaces, and a Neumann type boundary condition is applied on the wetted blade and hub surfaces. For a given cavitation number, the unknown cavity surface is determined in an iterative manner until both the prescribed pressure condition and the flow tangency conditions are satisfied on the cavity. The general formulation for the prediction of unsteady sheet cavitation on conventional fully submerged propellers is presented in [Kinnas and Fine 1992; Fine 1992; Young and Kinnas 2001]. It is summarized

in this section for the sake of completeness. The numerical implementation, treatments for face and back cavitation, and treatments for supercavitating propellers, are also presented in this section.

2.3.1 Fundamental Assumptions

The propeller is assumed to be a rigid solid body which rotates at a constant angular velocity in an unbounded fluid. The inflow is assumed to be constant over the axial extent of the propeller. It represents the *effective wake* of the ship or cavitation tunnel. The effective wake models the vorticity in the inflow in **absence** of the propeller (also called the *nominal wake*) and the vorticity due to the propeller. It is determined via the coupling of a potential method (MPUF-3A) with an unsteady Euler solver (which models the rotational part of the flow) [Choi 2000; Choi and Kinnas 2000b,a, 2001].

The problem is solved with respect to a coordinate system that rotates with the blades. The resulting flow is assumed to be incompressible, inviscid, and irrotational. The viscous force is calculated by applying a uniform friction drag coefficient on the wetted portions of the blade and hub.

Only sheet cavities on the propeller blades are modeled. The sheet cavities are assumed to be constant pressure surfaces that grow and collapse with time. The cavities are allowed to grow on both sides of the blade surface and the detachment locations are searched for numerically.

2.3.2 Problem Definition

Consider a cavitating propeller subject to a general inflow wake, $\vec{q}_w(x_s, y_s, z_s)$, as shown in Fig. 2.1. The inflow wake is expressed in terms of the absolute (ship fixed) system of coordinates (x_s, y_s, z_s) . The inflow velocity, \vec{q}_{in} , with respect to the blade fixed coordinates (x, y, z) , can be expressed as the sum of the inflow wake velocity, \vec{q}_w , and the propeller's angular velocity $\vec{\omega}$, at a given location \vec{x} :

$$\vec{q}_{in}(x, y, z, t) = \vec{q}_w(x, r, \theta_B - \omega t) + \vec{\omega} \times \vec{x} \quad (2.1)$$

where $r = \sqrt{y^2 + z^2}$, $\theta_B = \arctan(z/y)$, and $\vec{x} = (x, y, z)$.

As explained in the previous section, the inflow (\vec{q}_w) is assumed to be the effective wake. The resulting flow is assumed to be incompressible, inviscid, and irrotational flow. Therefore, the time dependent perturbation potential, $\phi(x, y, z, t)$, can be expressed as follows:

$$\vec{q}(x, y, z, t) = \vec{q}_{in}(x, y, z, t) + \nabla\phi(x, y, z, t) \quad (2.2)$$

where ϕ satisfies the Laplace's equation in the fluid domain:

$$\nabla^2\phi = 0 \quad (2.3)$$

Note that in analyzing the flow around the propeller, the blade fixed coordinates system is used.

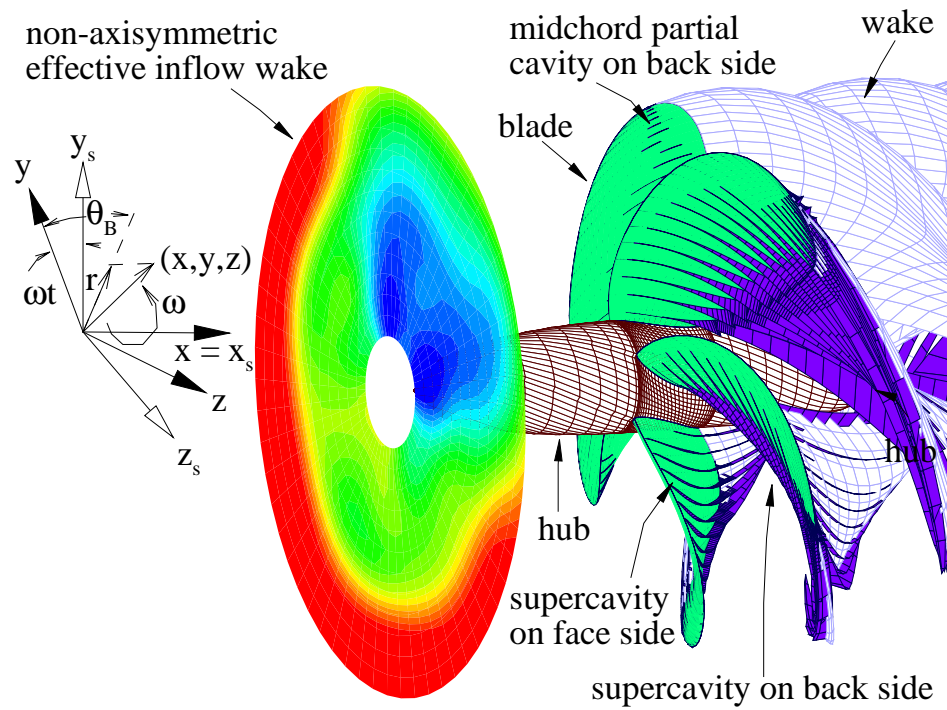


Figure 2.1: Propeller subjected to a general inflow wake. The blade fixed (x, y, z) and ship fixed (x_s, y_s, z_s) coordinate systems are shown.

2.3.3 Green's Formula

The perturbation potential, ϕ , at every point p on the combined wetted blade and cavity surface, $S_{WB}(t) \cup S_C(t)$, must satisfy Green's third identity:

$$2\pi\phi_p(t) = \int \int_{S_{WB}(t) \cup S_C(t)} \left[\phi_q(t) \frac{\partial G(p; q)}{\partial n_q(t)} - G(p; q) \frac{\partial \phi_q(t)}{\partial n_q(t)} \right] dS + \int \int_{S_W(t)} \Delta\phi(r_q, \theta_q, t) \frac{\partial G(p; q)}{\partial n_q(t)} dS; \quad p \in S_{WB}(t) \cup S_C(t) \quad (2.4)$$

where the subscript q corresponds to the variable point in the integration. $G(p; q) = 1/R(p; q)$ is the Green's function with $R(p; q)$ being the distance between points p and q . \vec{n}_q is the unit vector normal to the integration surface, with the positive direction pointing into the fluid domain. $\Delta\phi$ is the potential jump across the wake surface, $S_W(t)$. As shown in Fig. 2.2, the symbols $S_{WB}(t)$, $S_C(t)$, and $S_W(t)$ denote the wetted blade and hub, blade sheet cavity, and wake surfaces, respectively.

Equation 2.4 should be applied on the "exact" cavity surface S_C , as shown in part (a) of Fig. 2.2. However, the cavity surface is not known and has to be determined as part of the solution. In this work, an approximated cavity surface, shown in part (b) of Fig. 2.2, is used. The approximated cavity surface is comprised of the blade surface underneath the cavity on the blade, $S_{CB}(t)$, and the portion of the wake surface which is overlapped by the cavity, $S_{CW}(t)$. The justification for making this approximation, as well as a measure of its effect on the cavity solution can be found in [Kinnas and Fine 1993; Fine 1992]. Using the approximated cavity surface, Eqn. 2.4 may be decomposed into a summation of integrals over the blade surface, $S_B \equiv S_{CB}(t) + S_{WB}(t)$, and the portion of the wake surface which is overlapped by the cavity, $S_{CW}(t)$.

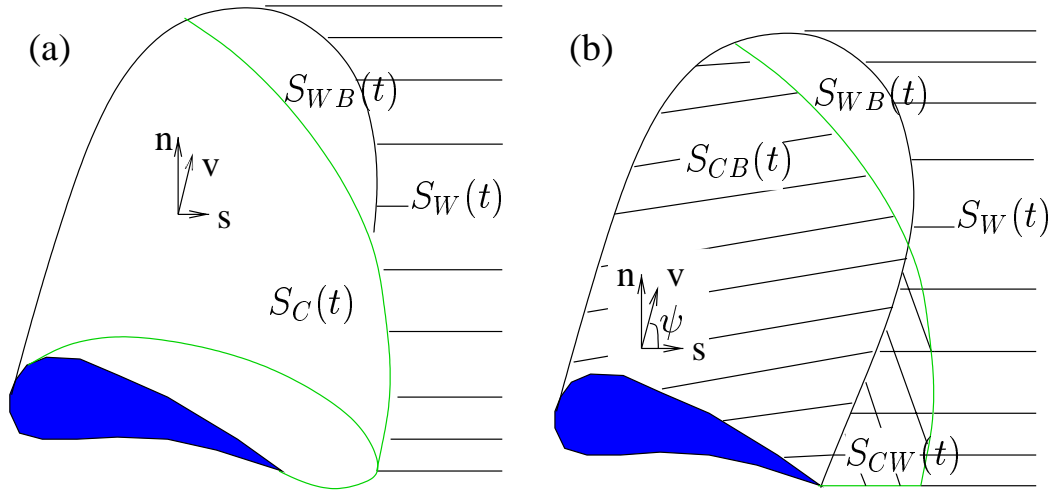


Figure 2.2: (a) Definition of the exact surface. (b) Definition of the approximated cavity surface .

• *Field Points on S_B .*

For field points on S_B , Eqn. 2.4 becomes:

$$\begin{aligned}
2\pi\phi_p(t) &= \int \int_{S_B} \left[\phi_q(t) \frac{\partial G(p; q)}{\partial n_q} - G(p; q) \frac{\partial \phi_q(t)}{\partial n_q} \right] dS \\
&- \int \int_{S_{CW}(t)} q_w(t) G(p; q) dS \\
&+ \int \int_{S_{CW}(t) \cup S_W(t)} \Delta \phi(r_q, \theta_q, t) \frac{\partial G(p; q)}{\partial n_q} dS; \quad p \in S_B \quad (2.5)
\end{aligned}$$

where q_w is the cavity source distribution in the wake, defined as:

$$q_w(t) \equiv \frac{\partial \phi^+}{\partial n}(t) - \frac{\partial \phi^-}{\partial n}(t) \quad (2.6)$$

The superscripts ”+” and ”-” denote the upper and lower wake surface, respectively.

The trailing wake geometry is determined by satisfying the *force-free* wake condition, which requires zero pressure jump across the wake sheet. In this work,

the wake is aligned with the circumferentially averaged inflow using an iterative lifting surface method developed by [Greeley and Kerwin 1982]. As stated in [Greeley and Kerwin 1982], this method “artificially” suppresses the wake roll-up. Recently, a fully unsteady wake alignment method, including wake roll-up and developed tip vortex cavity, is developed for propellers in non-axisymmetric inflows [Lee and Kinnas 2001a, 2002; Lee 2002]. The formulation and results using this unsteady wake alignment method is presented in [Lee and Kinnas 2001a, 2002; Lee 2002].

The dipole strength $\Delta\phi(r, \theta, t)$ in the wake is convected along the assumed wake model with angular speed ω :

$$\begin{aligned}\Delta\phi(r, \theta, t) &= \Delta\phi_T\left(r_T, t - \frac{\theta - \theta_T}{\omega}\right); & t \geq \frac{\theta - \theta_T}{\omega} \\ \Delta\phi(r, \theta, t) &= \Delta\phi^S(r_T); & t < \frac{\theta - \theta_T}{\omega}\end{aligned}\tag{2.7}$$

where r, θ are the cylindrical coordinates at any point in the trailing wake surface, S_W , and (r_T, θ_T) are the coordinates of the trailing edge at a point on the same streamline with (r, θ) . $\Delta\phi^S$ is the steady flow potential jump in the wake when the propeller is subject to the circumferentially averaged flow.

The value of the dipole strength, $\Delta\phi_T(r_T, t)$, at the trailing edge of the blade at radius r_T and time t , is given by Morino’s Kutta condition [Morino and Kuo 1974]:

$$\Delta\phi_T(r_T, t) = \phi_T^+(r_T, t) - \phi_T^-(r_T, t)\tag{2.8}$$

where $\phi_T^+(r_T, t)$ and $\phi_T^-(r_T, t)$ are the values of the potential at the upper (suction side) and lower (pressure side) blade trailing edge, respectively, at time t .

Recently, an iterative pressure Kutta condition [Kinnas and Hsin 1992] is applied instead for the analysis of unsteady fully wetted and cavitating propellers. The iterative pressure Kutta condition modifies $\Delta\phi_T(r_T, t)$ from that of Morino to achieve equality of pressures at both sides of the trailing edge everywhere on the blade [Young et al. 2001a].

- *Field Points on S_{CW} .*

For field points on S_{CW} , the left-hand side of Eqn. 2.4 reduces to $2\pi [\phi_p^+(t) + \phi_p^-(t)]$, which can be expressed as $4\pi\phi_p^\pm(t) \mp 2\pi\Delta\phi_p(t)$ depending on if the equation is applied on the upper “+” or the lower “-” surface of the supercavitating region. This will render the following expression for ϕ_p^\pm :

$$\begin{aligned}
4\pi\phi_p^\pm(t) &= \pm 2\pi\Delta\phi_p(t) + \int \int_{S_B} \left[\phi_q(t) \frac{\partial G(p; q)}{\partial n_q} - G(p; q) \frac{\partial \phi_q(t)}{\partial n_q} \right] dS \\
&- \int \int_{S_{CW}(t)} q_w(t) G(p; q) dS \\
&+ \int \int_{S_{CW}(t) \cup S_W(t)} \Delta\phi(r_q, \theta_q, t) \frac{\partial G(p; q)}{\partial n_q} dS; \quad p \in S_{CW}(t) \quad (2.9)
\end{aligned}$$

2.3.4 Boundary Conditions

Equations 2.5 and 2.9 implied that the perturbation potential (ϕ_p) can be expressed as: (1) continuous source (G) and dipole ($\frac{\partial G}{\partial n}$) distributions on the wetted blade (S_{WB}) and cavity ($S_{CB} \cup S_{CW}$) surfaces, and (2) continuous dipole distribution on the wake surface S_W . Thus, ϕ_p can be uniquely determined by satisfying the following boundary conditions:

- *Kinematic Boundary Condition on Wetted Blade and Hub Surfaces*

The kinematic boundary condition requires the flow to be tangent to the wetted blade and hub surface. Thus, the source strengths, $\frac{\partial \phi}{\partial n}$, are known in terms of the inflow velocity, \vec{q}_{in} :

$$\frac{\partial \phi}{\partial n} = -\vec{q}_{in} \cdot \vec{n} \quad (2.10)$$

• *Dynamic Boundary Condition on Cavitating Surfaces*

The dynamic boundary condition on the cavitating blade and wake surfaces requires the pressure everywhere on the cavity to be constant and equal to the vapor pressure, P_v . By applying Bernoulli's equation, the total cavity velocity, \vec{q}_c , can be expressed as follows:

$$|\vec{q}_c|^2 = n^2 D^2 \sigma_n + |\vec{q}_w|^2 + \omega^2 r^2 - 2gy_s - 2\frac{\partial\phi}{\partial t} \quad (2.11)$$

where $\sigma_n \equiv (P_o - P_v)/(\frac{\rho}{2}n^2 D^2)$ is the cavitation number; ρ is the fluid density and r is the distance from the axis of rotation. P_o is the pressure far upstream on the shaft axis; g is the acceleration of gravity and y_s is the ship fixed coordinate, shown in Fig. 2.1. $n = \omega/2\pi$ and D are the propeller rotational frequency and diameter, respectively.

The total cavity velocity can also be expressed in terms of the local derivatives along the s (chordwise), v (spanwise), and n (normal) grid directions:

$$\vec{q}_c = \frac{V_s [\vec{s} - (\vec{s} \cdot \vec{v})\vec{v}] + V_v [\vec{v} - (\vec{s} \cdot \vec{v})\vec{s}]}{||\vec{s} \times \vec{v}||^2} + (V_n) \vec{n} \quad (2.12)$$

where \vec{s} , \vec{v} , and \vec{n} denote the unit vectors along the non-orthogonal curvilinear coordinates s , v , and n , respectively. The total velocities on the local coordinates (V_s, V_v, V_n) are defined as follows:

$$\begin{aligned} V_s &\equiv \frac{\partial\phi}{\partial s} + \vec{q}_{in} \cdot \vec{s} \\ V_v &\equiv \frac{\partial\phi}{\partial v} + \vec{q}_{in} \cdot \vec{v} \\ V_n &\equiv \frac{\partial\phi}{\partial n} + \vec{q}_{in} \cdot \vec{n} \end{aligned} \quad (2.13)$$

Note that if s , v , and n were located on the “exact” cavity surface, then the total normal velocity, V_n , would be zero. However, this is not the case since the cavity surface is approximated with the blade surface beneath the cavity and the wake surface overlapped by the cavity. Although V_n may not be exactly zero on the approximated cavity surface, it is small enough to be neglected in the dynamic boundary condition [Fine 1992].

Equations 2.11 and 2.12 can be integrated to form a quadratic equation in terms of the unknown chordwise perturbation velocity $\frac{\partial \phi}{\partial s}$. By selecting the root which corresponds to the cavity velocity vectors that point downstream, the following expression can be derived:

$$\frac{\partial \phi}{\partial s} = -\vec{q}_{in} \cdot \vec{s} + V_v \cos \psi + \sin \psi \sqrt{|\vec{q}_c|^2 - V_v^2} \quad (2.14)$$

where ψ is the angle between s and v directions, as shown in Fig. 2.2.

Equation 2.14 can then be integrated to form a Dirichlet type boundary condition for ϕ :

$$\phi(s, v, t) = \phi(s_o, v, t) + \int_{s_o}^s \left\{ -\vec{q}_{in} \cdot \vec{s} + V_v \cos \psi + \sin \psi \sqrt{|\vec{q}_c|^2 - V_v^2} \right\} ds \quad (2.15)$$

where $s = s_o$ corresponds to the cavity leading edge. The terms $\frac{\partial \phi}{\partial t}$ and $\frac{\partial \phi}{\partial v}$ inside $|\vec{q}_c|^2$ and V_v on the right-hand-side of Eqn. 2.15 are also unknowns and are determined in an iterative manner. The value of $\phi(s_o, v, t)$ is determined via cubic extrapolation of the unknown potentials on the wetted blade surface immediately upstream of the cavity.

On the cavitating wake surface, the coordinate s is assumed to follow the streamline. It was found that the crossflow term ($\frac{\partial}{\partial v}$) in the cavitating wake region had a very small effect on the solution [Fine 1992; Fine and Kinnas 1993]. Thus, the total cross flow velocity is assumed to be small, which renders the following expression for ϕ on the cavitating wake surface:

$$\phi^{\pm}(s, v, t) = \phi^{\pm}(s_T, v, t) + \int_{s_T}^s \{-\vec{q}_{in} \cdot \vec{s} + |\vec{q}_c|\} ds \quad (2.16)$$

where s_T is the s-direction curvilinear coordinate at the blade trailing edge. ϕ^+ and ϕ^- represent the potential on the upper and lower wake surface, respectively. The value of $\phi^{\pm}(s_T, v, t)$ can be obtained by applying Eqn. 2.15 at the blade trailing edge.

• *Kinematic Boundary Condition on Cavitating Surfaces*

The kinematic boundary condition requires that the total velocity normal to the cavity surface to be zero:

$$\frac{D}{Dt}(n - h(s, v, t)) = \left[\frac{\partial}{\partial t} + \vec{q}_c(x, y, z, t) \cdot \nabla \right] (n - h(s, v, t)) = 0 \quad (2.17)$$

where n and h are the curvilinear coordinate and cavity thickness normal to the blade surface, respectively, as shown in Fig. 2.3.

Substituting Eqn. 2.12 into Eqn. 2.17 yields the following partial differential equation for h on the blade [Kinnas and Fine 1992]:

$$\frac{\partial h}{\partial s} [V_s - \cos \psi V_v] + \frac{\partial h}{\partial v} [V_v - \cos \psi V_s] = \sin^2 \psi \left(V_n - \frac{\partial h}{\partial t} \right) \quad (2.18)$$

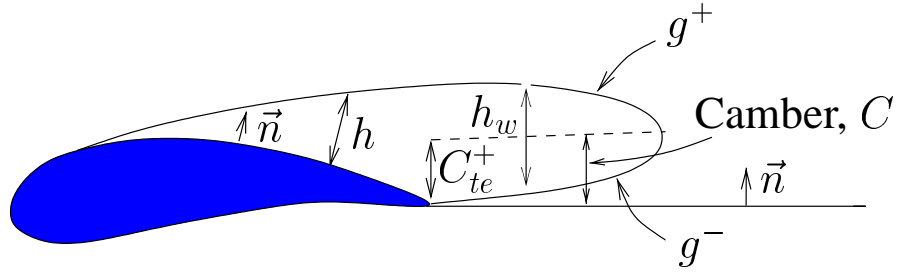


Figure 2.3: Definition of the cavity height on the blade and on the supercavitating wake.

Assuming again that the spanwise crossflow velocity on the wake surface is small, the kinematic boundary condition reduces to the following equation for the cavity thickness (h_w) in the wake:

$$q_w(t) - \frac{\partial h_w}{\partial t} = |\vec{q}_c| \frac{\partial h_w}{\partial s} \quad (2.19)$$

where q_w is the cavity source distribution, defined by Eqn. 2.6. Note that h_w in Eqn. 2.19 is defined normal to the wake surface, as shown in Fig. 2.3. In addition, the quantity h_w at the blade trailing edge is determined by interpolating the upper and/or lower cavity surface over the blade and computing its normal offset from the wake sheet.

- *Cavity Closure Condition*

The extent of the unsteady cavity is unknown and has to be determined as part of the solution. The cavity length at each radius r and time t is given by the function $l(r, t)$. For a given cavitation number, σ_n , the cavity planform, $l(r, t)$, must

satisfy the following condition:

$$\delta(l(r, t); r, \sigma_n) \equiv h(l(r, t), r, t) = 0 \quad (2.20)$$

where δ is the cavity height at the trailing edge of the cavity. Equation 2.20 requires that the cavity closes at its trailing edge. This requirement is the basis of an iterative solution method that is used to find the cavity planform [Kinnas and Fine 1993], and is demonstrated in 2-D in Fig. 2.4.

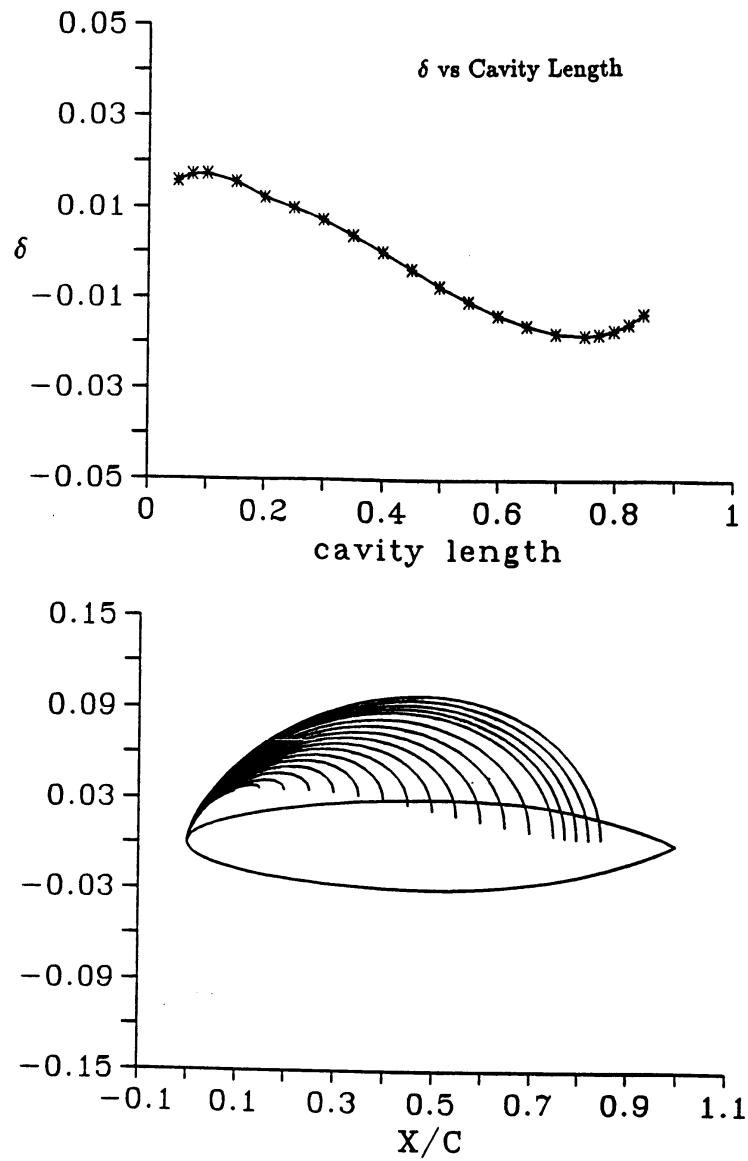


Figure 2.4: An example showing how the cavity closure condition is satisfied for a 2-D hydrofoil. Left: Plot of predicted cavity shape for different guess of cavity length l . Right: Plot showing convergence of cavity trailing edge thickness δ with l . Taken from [Kinnas and Fine 1993].

2.4 Numerical Implementation

The unsteady cavity problem is solved by inverting Eqns. 2.5 and 2.9 subject to conditions 2.7, 2.8, 2.10, 2.15, 2.16, and 2.20. The numerical implementation is described in detail in [Kinnas and Fine 1992; Fine 1992; Kinnas and Fine 1993]. It will be summarized here for the sake of completeness.

2.4.1 Solution Algorithm

For a given cavity planform, Green's formula is solved with respect to unknowns ϕ on the wetted blade and hub surfaces, and unknowns $\frac{\partial\phi}{\partial n}$ on the cavity surface. The *key* blade and the hub surfaces are discretized into a number of quadrilateral panels. The key trailing wake is discretized into panels with constant angular intervals $\Delta\theta_W = \omega\Delta t$, with Δt being the time step size. $\frac{\partial\phi}{\partial n}$ and ϕ for each panel are approximated with constant strength distributions.

The known values of $\frac{\partial\phi}{\partial n}$ on the wetted blade surface are given by the inflow velocity via Eqn. 2.10. The known values of ϕ on the cavity surface are computed by Eqns. 2.15 and 2.16 using trapezoidal quadrature. The potentials are required to be continuous from the wetted portions of the blade to the cavitation portions of the blade and wake.

The time marching scheme is similar to that described in [Fine 1992]. A constant time increment, Δt , is used. At each time step, the propeller blades rotate by a blade angle increment $\Delta\theta = \omega\Delta t$. Notice that in Eqns. 2.15 and 2.16, $\frac{\partial\phi}{\partial t}$ is assumed to be known. In the current algorithm, it is given by a second order moving least square derivative recovery method [Tabbara et al. 1994] using the solution (ϕ)

obtained from the previous revolution. It should be noted that other time derivative schemes (such as a second-order central difference method or a third-order forward difference method) had been used, but similar results were obtained. However, for propellers subject to highly unsteady inflows, the current algorithm was found to be the most stable.

At each time step, the solution is only obtained for the key blade. The influence of each of the other blades is accounted for in a progressive manner by using the solution from an earlier time step when the key blade was in the position of that blade. The cavity heights on the blade and the wake are then computed by differentiating Eqns. 2.18 and 2.19 with a second order central finite difference method.

Finally, the correct cavity planform for each time step is obtained iteratively using a Newton-Raphson technique which requires the cavity closure condition (Eqn. 2.20) to be satisfied.

2.4.2 Split-Panel Technique

A very crucial issue in the numerical implementation relates to the treatment of panels which were intersected by the cavity trailing edge. In order to avoid recomputing influence coefficients, a *split* panel technique [Kinnas and Fine 1993; Fine 1992] is used. The technique determines ϕ and $\partial\phi/\partial n$ of the split panel via the

weighted average of the values on the wetted and the cavitating part of the panel:

$$\begin{aligned} \phi_{split} &= \frac{\phi_L l_L + \phi_R l_R}{l_L + l_R} \\ \left(\frac{\partial\phi}{\partial n}\right)_{split} &= \frac{\left(\frac{\partial\phi}{\partial n}\right)_L l_L + \left(\frac{\partial\phi}{\partial n}\right)_R l_R}{l_L + l_R} \end{aligned} \quad (2.21)$$

A schematic representation of the split panel technique is shown in Fig. 2.5. This technique has been shown to provide substantial savings on computer time since the same panel discretization can be used to treat arbitrary cavity planforms [Kinnas and Fine 1993; Fine 1992].

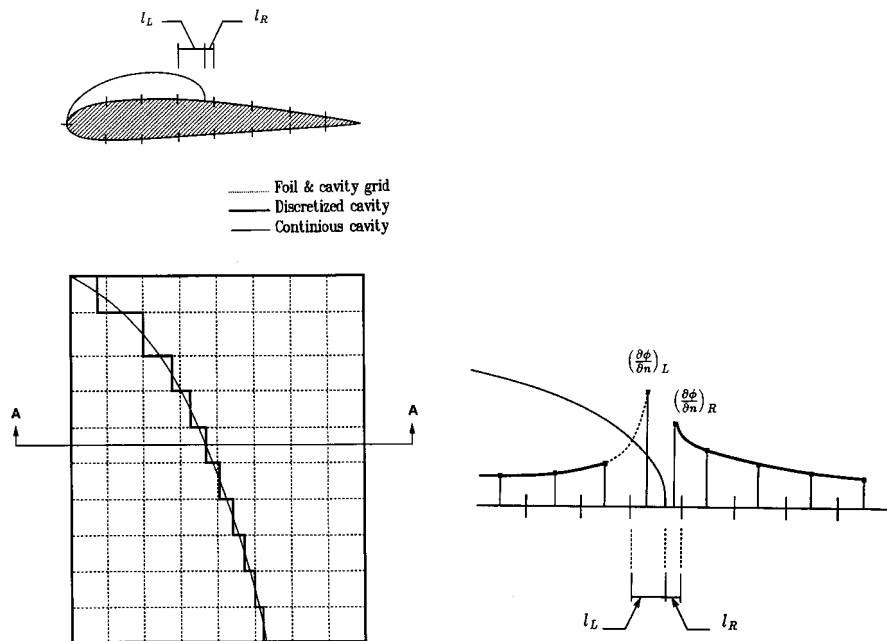


Figure 2.5: Left: The split panel technique applied to the cavity trailing edge in 3-D. Right: The extrapolated values for $\partial\phi/\partial n$ into two parts of the split panel. Taken from [Kinnas and Fine 1993].

2.4.3 Cavity Detachment Search Criterion

The cavity detachment location is determined via an iterative algorithm. First, the initial detachment lines at each time step (or blade angle) are obtained based on the fully wetted pressure distributions. The search algorithm at each spanwise strip begins at the section leading edge and travels downstream to the section trailing edge. The initial detachment location for each strip is given as the first point along the chordwise direction where the wetted pressure is less than or equal to the vapor pressure (i.e., $-C_p \geq \sigma_n$). However, this is not sufficient because the development of cavity alters the flow around the blade. Thus, at each time step, the cavity detachment location at each radial strip needs to be adjusted iteratively at every revolution until the following *smooth detachment condition* is satisfied:

1. The cavity has non-negative thickness at its leading edge, and
2. The pressure on the wetted portion of the blade upstream of the cavity should be greater than the vapor pressure.

It can be shown that the above criterion is equivalent to the Villat-Brillouin condition [Brillouin 1911; Villat 1914]. The implementation of the detachment search algorithm is given below, and is depicted in Fig. 2.6.

1. If the cavity at the strip has negative thickness, then the detachment location moves toward the trailing edge of the blade section.
2. If the pressure at a point upstream of the cavity is below the vapor pressure,

then the detachment location moves toward the leading edge of the blade section.

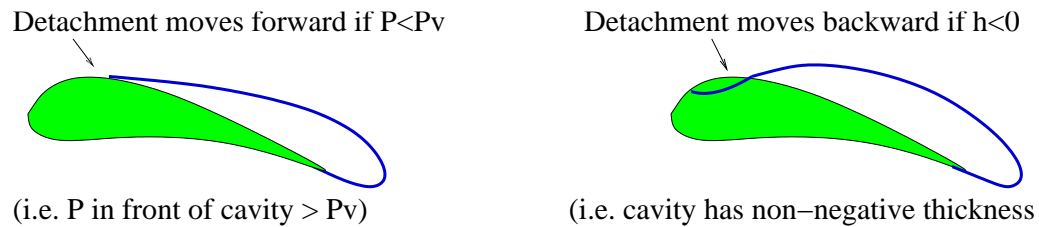


Figure 2.6: A graphical depiction of the cavity detachment search algorithm.

It should be noted that the current work assumes the flow to be inviscid. However, it is widely known that viscosity affects the cavity detachment, as well as the extent and thickness of the cavity. It is generally accepted that the cavity detachment is well downstream of the smooth detachment point, and the pressure upstream of the cavity detachment point may be smaller than the cavity pressure [Kinnas et al. 1994]. Investigations by [Arakeri 1975; Franc and Michel 1985] suggested that cavity detachment occurs immediately downstream of the laminar separation point. Using this condition and by coupling a fully nonlinear 2-D BEM with a viscous flow model, [Kinnas et al. 1994] concluded that inviscid cavity theory:

1. Over-predicted, by a small amount, the cavity extent and volume for a fixed cavitation number and angle of attack.
2. Under-predicted, by a small amount, the cavity extent and volume for a fixed cavitation number and lift coefficient.

However, [Kinnas et al. 1994] also concluded that the effect of viscosity on the predicted cavity extent and volume is negligible for the case of supercavitation. Nevertheless, future efforts should include the modeling of visous effects via a Navier Stokes solver or by coupling the current 3-D BEM with a boundary layer solver, similar to that applied in [Kinnas et al. 1994].

2.5 Face and Back Cavitation

For most conventional propellers, the dominant type of cavitation is leading edge back cavitation (i.e. cavity that forms on the suction side of the blade and detaches from the leading edge). However, midchord cavitation (i.e. cavity that detaches aft of the leading edge) is becoming more and more common in recent designs. This is often due to the designer's attempt to increase efficiency by decreasing cavity thickness [Vorus and Mitchell 1994] or designing sections with nearly constant pressure distribution on the suction [Jessup et al. 1994]. Midchord cavitation is also possible on conventional propellers when operating at off design conditions.

PROPCAV has been extended to search for cavity detachments on the back or the face of the blade by [Mueller and Kinnas 1997; Mueller 1998; Mueller and Kinnas 1999]. The search for cavitation on the face (pressure side) of the blade is also necessary because it is common for propellers subjected to off design conditions or non-uniform inflows. Propellers are often designed to produce a certain mean thrust. However, part or all of the blade may experience smaller loadings at certain angular positions due to the non-axisymmetric inflow. As a result, very small or negative angle of attack may occur, which in turn leads to face cavitation.

However, the search for face or back cavitation alone may not be sufficient because these two phenomena can alternate or occur simultaneously in a propeller revolution. Alternating or simultaneous face and back cavitation is also very common for controllable pitch propellers. In addition, some of the latest hydrofoil and propeller design intentionally produce simultaneous face and back cavitation to

achieve maximum efficiency. Thus, one of the objectives in the modeling of fully submerged propellers is to extend PROPCAV to predict face and/or back cavitation with search cavity detachment on both sides of the blade section.

2.5.1 Numerical Algorithm

The present method searches for the cavity detachments and determines the cavity lengths on both sides of the blade simultaneously. For each radial strip, the initial cavity detachments are obtained based on the fully wetted pressure distributions. Initial guesses of the cavity lengths are then assigned to both sides of each strip.

•*Dynamic Boundary Condition on Cavitating Surfaces*

The dynamic boundary condition, Eqns. 2.15 and 2.16, gives the known strengths of the potential (ϕ) on all cavitating surfaces:

$$\begin{aligned} \phi(s^\pm, v, t) &= \phi(s_o^\pm, v, t) + \int_{s_o^\pm}^{s^\pm} \{-\vec{q}_{in} \cdot \vec{s} + V_v \cos \psi \\ &+ \sin \psi \sqrt{|\vec{q}_c|^2 - V_v^2}\} ds; \quad s_o^\pm \leq s^\pm \leq s_c^\pm \end{aligned} \quad (2.22)$$

$$\begin{aligned} \phi^\pm(s_w^\pm, v, t) &= \phi^\pm(s_T^\pm, v, t) \\ &+ \int_{s_T^\pm}^{s_w^\pm} \{-\vec{q}_{in} \cdot \vec{s} + |\vec{q}_c|\} ds; \quad s_T^\pm \leq s_w^\pm \leq s_{TE}^\pm \end{aligned} \quad (2.23)$$

where the superscripts "+" and "-" denote the suction side and pressure side cavitating surfaces, respectively. As shown in Fig. 2.7, s is the arclength defined from the cavity leading edge, and s_w is the arclength defined from the blade trailing edge. The quantity $\phi(s_o^\pm, v, t)$ is the perturbation potential at the cavity leading edge. It is

determined via cubic extrapolation of the unknown potentials on the wetted blade panels adjacent to the cavity leading edge:

$$\begin{aligned} \phi(s_o^\pm, v, t) = & C_1^\pm(m, t)\phi_1^\pm(m, t) + C_2^\pm(m, t)\phi_2^\pm(m, t) \\ & + C_3^\pm(m, t)\phi_3^\pm(m, t) + C_4^\pm(m, t)\frac{\partial\phi}{\partial s}(s_o^\pm, v, t) \end{aligned} \quad (2.24)$$

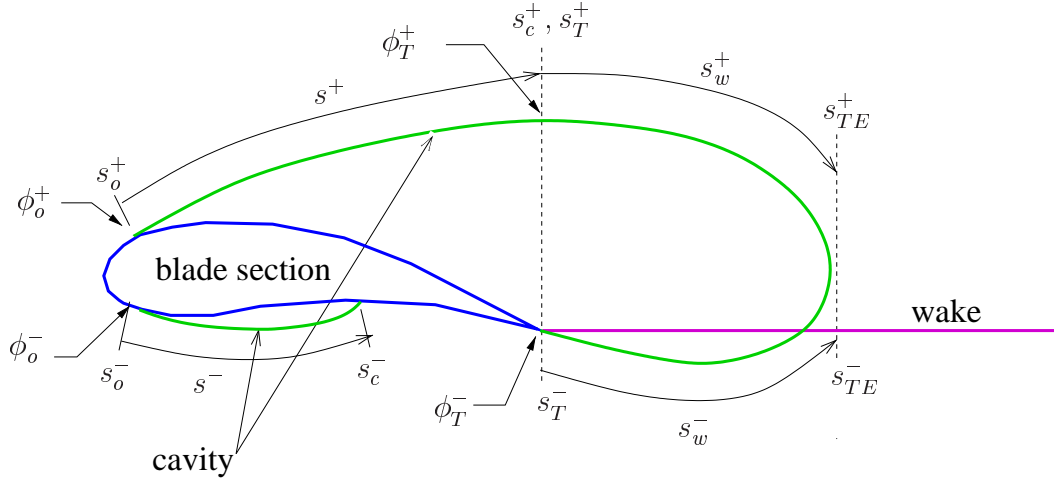


Figure 2.7: Application of the dynamic boundary condition on the face and the back of a cavitating blade section.

where $C_1^\pm(m, t), \dots, C_4^\pm(m, t)$ are the extrapolation coefficients for cavitating blade panels on radial strip m at time t . As shown in Fig. 2.8, $\phi_1^\pm(m, t), \dots, \phi_3^\pm(m, t)$ represent the unknown potentials on the wetted blade panels upstream of the cavity leading edge. The quantity $\frac{\partial\phi}{\partial s}(s_o^\pm, v, t)$ is the tangential component of the perturbation velocity at the cavity leading edge.

The quantity $\phi(s_T^\pm, v, t)$ in Eqn. 2.23 is the perturbation potential at the blade

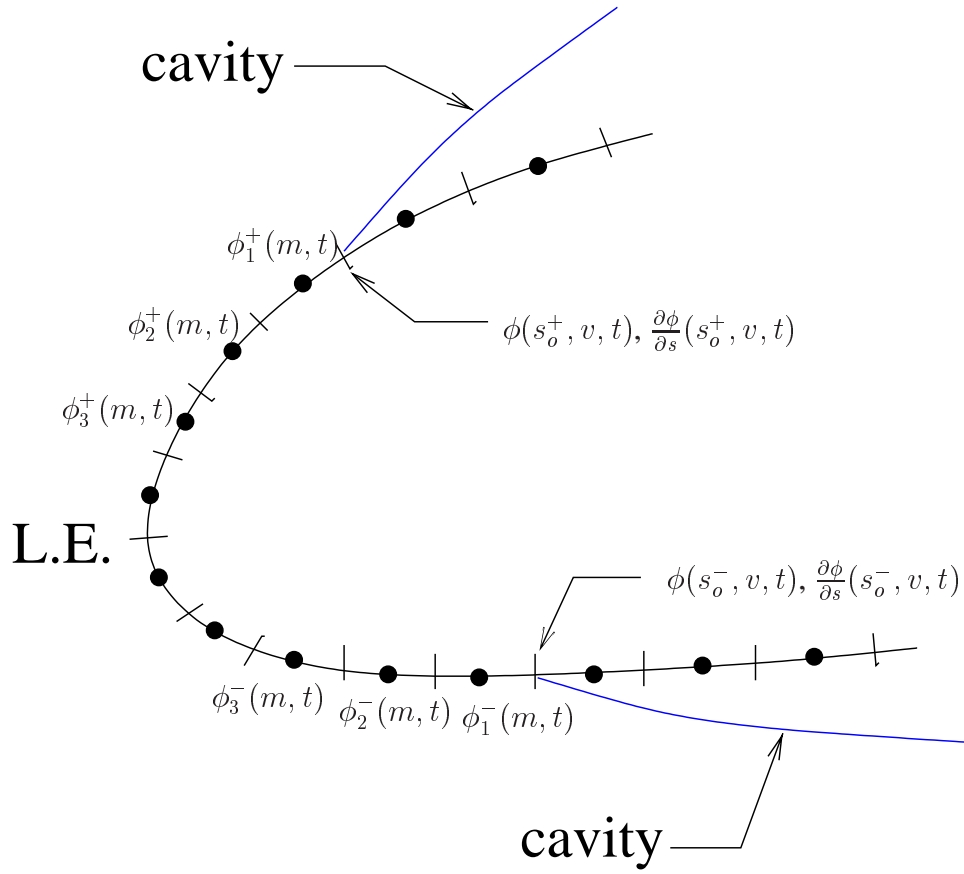


Figure 2.8: Extrapolation of the potential at the cavity leading edge on the face and the back of a cavitating blade section.

trailing edge. It is determined by evaluating Eqn. 2.22 at $s^\pm = s_c^\pm$:

$$\begin{aligned} \phi(s_T^\pm, v, t) &= \phi(s_c^\pm, v, t) = \phi(s_o^\pm, v, t) \\ &+ \int_{s_o^\pm}^{s_c^\pm} \left\{ -\vec{q}_{in} \cdot \vec{s} + V_v \cos \psi + \sin \psi \sqrt{|\vec{q}_c|^2 - V_v^2} \right\} ds \end{aligned} \quad (2.25)$$

The kinematic boundary condition, Eqn. 2.10, gives the known source strength ($\frac{\partial \phi}{\partial n}$) on the wetted body surfaces. Green's third identity, Eqns. 2.5 and 2.9, is then solved to obtain (1) the unknowns ϕ on the wetted body surfaces, and (2) the un-

knows $\frac{\partial\phi}{\partial n}$ on the cavitating surfaces. Details of the numerical implementation for Eqns. 2.5 and 2.9 are presented in [Fine 1992].

•*Kinematic Boundary Condition on Cavitating Surfaces*

Once the problem is solved for the assumed cavity detachment locations and extents, the cavity thickness can be determined via the kinematic boundary condition, Eqns. 2.18 and 2.19. The cavity heights on the suction and the pressure side of the blade is denoted by h^+ and h^- , respectively. The partial differential equation for h^\pm in Eqn. 2.18 is evaluated at time step k using a two-point backward difference formula:

$$\begin{aligned}\frac{\partial h^\pm}{\partial s} &= \frac{h_{n+1,m,k}^\pm - h_{n,m,k}^\pm}{\Delta s_{n,m,k}^\pm} \\ \frac{\partial h^\pm}{\partial v} &= \frac{H_{n,m,k}^\pm - H_{n,m-1,k}^\pm}{\Delta v_{n,m,k}^\pm} \\ \frac{\partial h^\pm}{\partial t} &= \frac{H_{n,m,k}^\pm - H_{n,m,k-1}^\pm}{\Delta t}\end{aligned}\tag{2.26}$$

where

$$H_{n,m,k}^\pm = \frac{1}{2}(h_{n,m,k}^\pm + h_{n+1,m,k}^\pm)\tag{2.27}$$

and subject to the following initial boundary condition:

$$h^\pm(1, m, k) = 0\tag{2.28}$$

The cavity thickness on the wake, h_w , is also evaluated via the same method. The schematic of the cavity height calculation is shown in Fig. 2.9. Note that the cavity

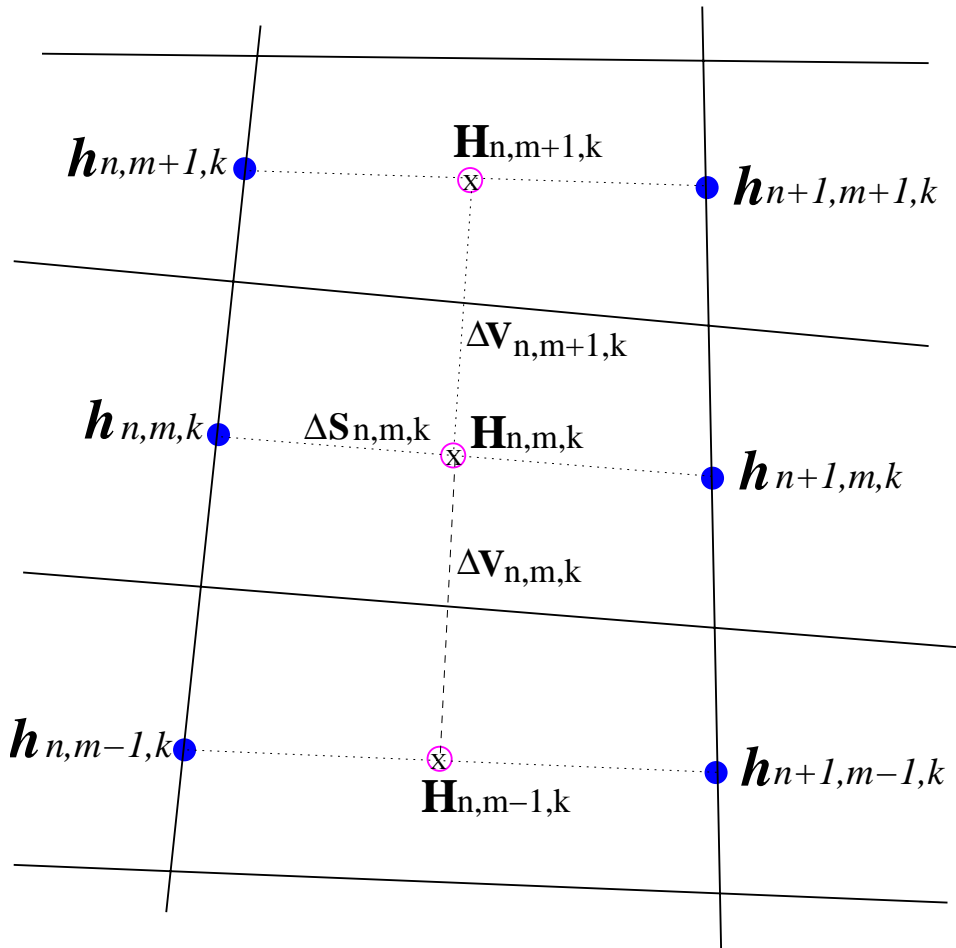


Figure 2.9: Schematic of cavity height calculation.

heights are calculated at the panel edges while the derivatives are calculated at the control points.

•*Cavity Closure Condition*

For assumed cavity detachment locations, the correct cavity extents are determined via the cavity closure condition:

$$\delta^\pm (l^\pm(r, t); r, \sigma_n) \equiv h^\pm (l^\pm(r, t), r, t) = 0 \quad (2.29)$$

where $l^\pm(r, t)$ and $\delta^\pm (l^\pm(r, t); r, \sigma_n)$ represent the cavity length and cavity trailing edge thickness, respectively, on the suction side (“+”) and the pressure side (“-”) at radius r of time t for a given σ_n . Equation 2.29 is solve via a Newton-Raphson algorithm explained in [Fine 1992].

If the cavity extends to the supercavitating wake, then the suction side and pressure side cavitating surfaces must meet at a point down stream on the wake. In other words, the thickness of the cavity trailing edge must be zero at all locations.

•*Cavity Detachment Search Algorithm*

Finally, the cavity detachment locations on both sides of the blade surface are adjusted in the next revolution according to the Villat-Brillouin smooth detachment condition described in Section 2.4.3.

An example of the initial cavity shape on a 3-D hydrofoil section with detachment locations obtained based on the wetted pressure distribution is shown on the top of Fig. 2.10. Notice that the resulting cavity on the suction side has negative thickness at its leading edge due to the incorrect guess of cavity detachment

locations. The converged cavity shapes and corresponding pressure distribution for the same foil section are shown on the bottom of Fig. 2.10. Notice that the Villat-Brillouin detachment condition is satisfied on both sides of the hydrofoil section. Also notice the considerable under prediction of the extent and volume (especially on the face side) of the cavities. Figure 2.10 demonstrates the importance to search for cavities on both sides of the blade surface. The hydrodynamic force, which is calculated by integrating the pressures acting normal to the blade surface, would be very different between the results shown on the top and the bottom of Figure 2.10.

2.5.2 Numerical Validation

Cavity patterns on conventional propellers which can be predicted by the present method are shown in Fig. 2.11. At the present time, there are no experimental data available to validate face and back cavitation patterns predictions by the method. Thus, only numerical validations for face and back cavitation are shown in this section. This is achieved by comparing the predictions for two identical 3-D rectangular hydrofoils⁴: one with a positive camber and positive angle of attack, and the other with a negative camber and negative angle of attack. These two hydrofoils should yield equal and opposite results. Figures 2.12 and 2.13 show validations test results for different combinations of cavitation patterns using sets of two identical hydrofoils. Note that the smooth detachment criterion is satisfied on both sides of the foil surface in all cases, and that the results are as expected.

⁴The option to run PROPCAV in “hydrofoil mode” is a modification that can be found in [Mueller 1998].

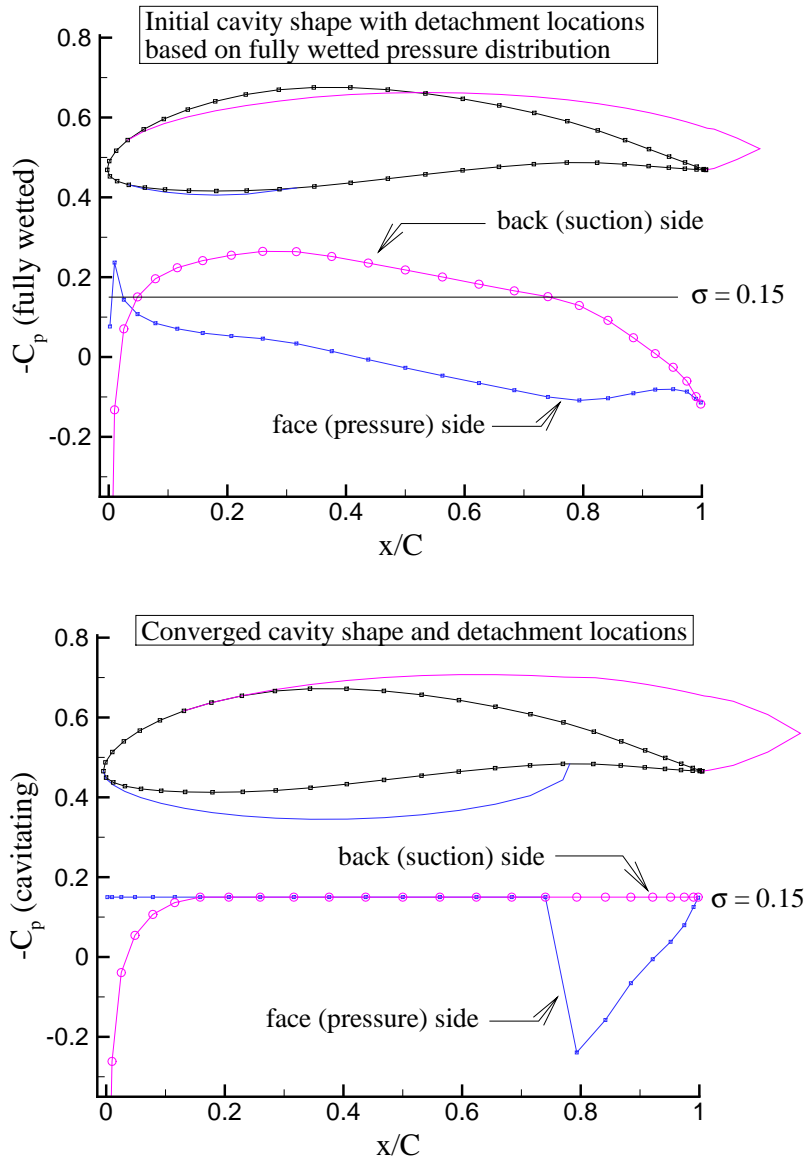


Figure 2.10: Top: Initial cavity shape for a 3-D hydrofoil section with detachment locations based on the shown wetted pressure distributions. Bottom: The converged cavity shape and cavity pressure distributions.

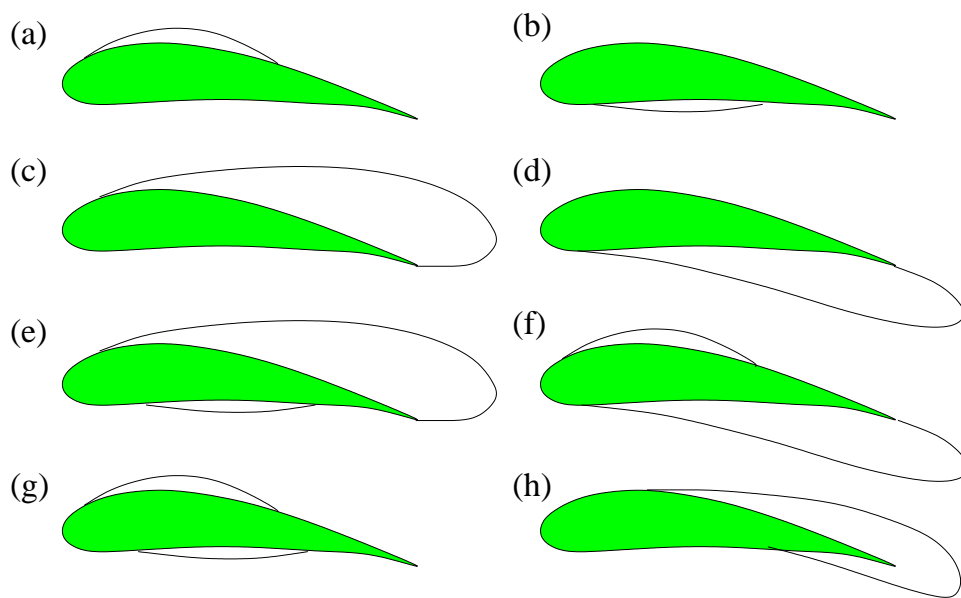


Figure 2.11: Cavitation patterns on conventional propellers which can be predicted by the present method.

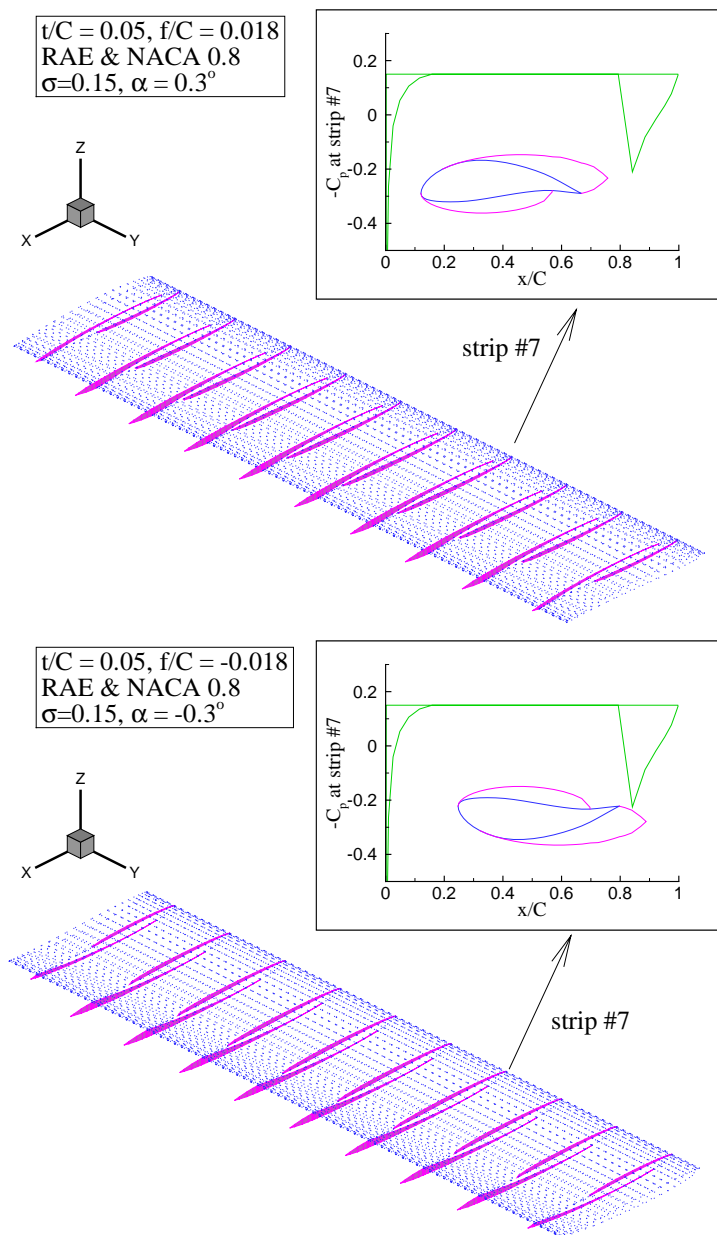


Figure 2.12: Validation of simultaneous face and back cavitation on an asymmetric rectangular hydrofoil. 50X10 panels. $\alpha = \pm 0.3^\circ$. $f_o/C = \pm 0.018$ (NACA a=0.8). $\tau_o/C = 0.05$ (RAE). $\sigma_v = 0.15$.

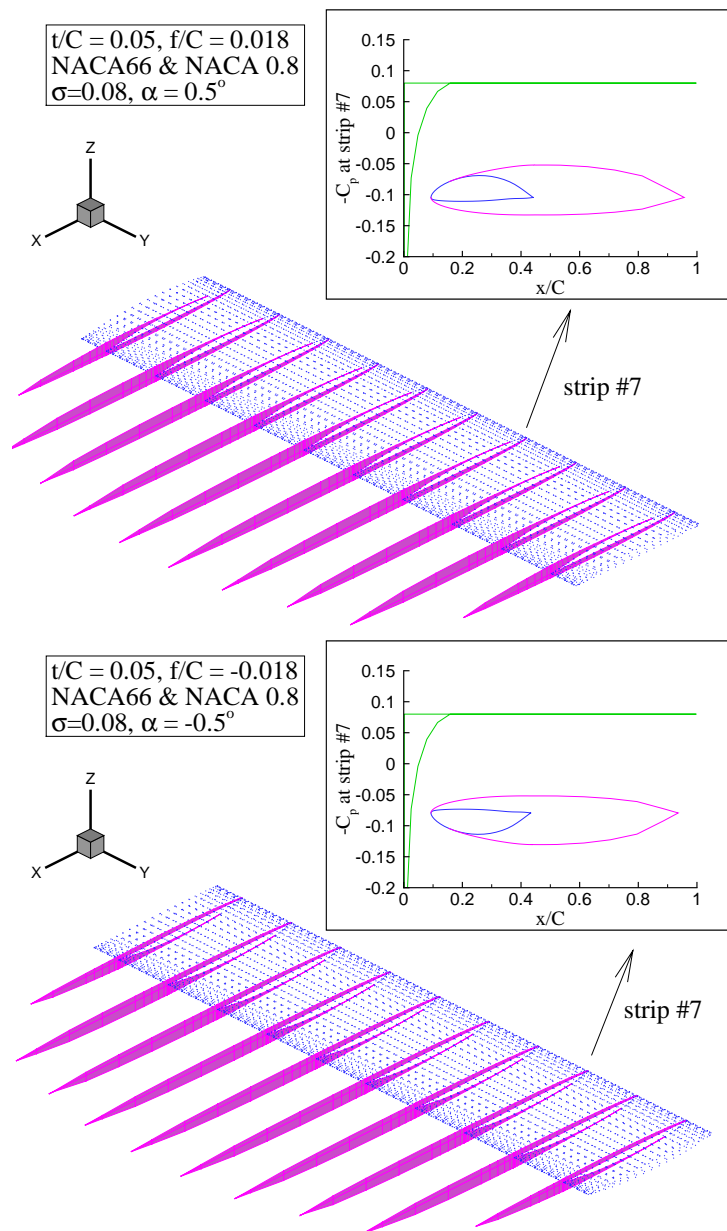


Figure 2.13: Validation of simultaneous face and back cavitation on an asymmetric rectangular hydrofoil. 50X10 panels. $\alpha = \pm 0.5^\circ$. $f_{max}/C = \pm 0.018$ (NACA a=0.8). $T_{max}/C = 0.05$ (NACA66). $\sigma_v = 0.08$.

2.6 Supercavitating Propellers

Experimental evidence shows that the separated zone behind the thick blade trailing edge forms a closed cavity that separates from the practically ideal irrotational flow around a supercavitating blade section [Russel 1958]. Furthermore, the pressure within the separated zone (also called the base pressure) can be assumed to be uniform [Riabouchinsky 1926; Tulin 1953]. However, in high Reynolds number flows, the mean base pressure depends on the mechanics of the wake turbulence [Roshko 1955]. This implies that a turbulent dissipation model, such as the one used in [Vorus and Chen 1987], is necessary to determine the mean base pressure and the extent of the separated zone. However, the use of such models in the prediction of unsteady 3-D cavitating propeller flows is not practical for engineering purposes.

To simplify the physics, [Kudo and Ukon 1994] assumed the supercavitating blade section to be base ventilated (i.e. the mean base pressure equal to the vapor pressure), and solved the steady cavitating propeller problem using a 3-D vortex-lattice lifting surface method. Later, [Kudo and Kinnas 1995] modified the method to allow for a variable length separated zone model which determines the mean base pressure. However, the length of the separated zone is arbitrarily specified by the user, and has found to affect the pressure and cavity length near the blade trailing edge under fully wetted and partially cavitating conditions. Furthermore, the method of [Kudo and Kinnas 1995] cannot be applied in unsteady cavitating analysis since the length of the separated zone changes with blade angle. In the present method, the assumption of [Kudo and Ukon 1994] is used for the analysis

of supercavitating propellers subjected to steady and unsteady inflow. The base pressure is assumed to be constant and equal to the vapor pressure, and the extent of the separated zone at each time step is determined iteratively like a cavity problem. The logic behind this assumption are:

1. The base pressure should equal to the vapor pressure in the case of supercavitation.
2. The separated zone has to communicate with the supercavity in the span-wise direction in the case of mixed cavitation (i.e. one part of the blade is wetted or partially cavitating while another part is supercavitating).
3. Most supercavitating propellers operate in supercavitating conditions.

Hence, the present method solves for the separated zone like an additional cavitation bubble. However, the “openness” at the blade trailing edge poses a problem for the panel method. Thus, a small closing zone, shown in Fig. 2.14, is introduced. The precise geometry of the closing zone is not important, as long as it is inside the separated region and its trailing edge lies on the aligned wake sheet. The method is modified so that it treats the original blade and the closing zone as one solid body. Thus, S_B in Eqns. 2.5 and 2.9 now includes the blade and hub surfaces, as well as the closing zone. Moreover, Eqns. 2.22 and 2.26 should also be applied over the closing zone. As depicted in Fig. 2.14, this scheme is applicable to fully wetted, partially cavitating, and supercavitating conditions in steady and unsteady flows. In addition, the numerical algorithm for the treatment of supercavitating pro-

pellers is the same as that for conventional cavitating propellers with the following modifications to the numerical algorithm.

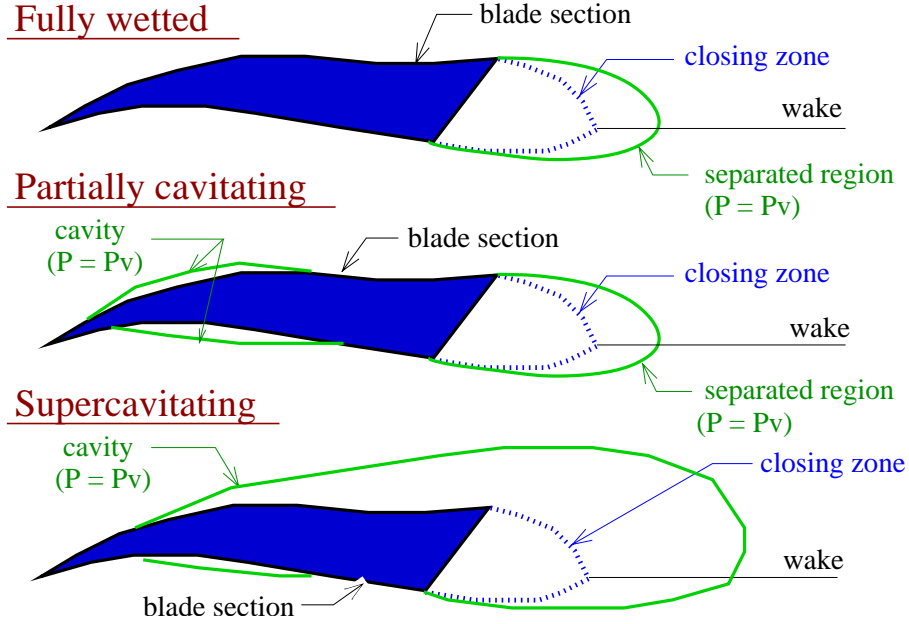


Figure 2.14: Treatment of supercavitating blade sections.

- *Dynamic Boundary Condition on Separated Region*

As depicted in Fig. 2.14, the separated region covers the entire closing zone, and extends to the wake panels. For the closing zone panels, the perturbation potential is determined as follows:

$$\begin{aligned} \phi(s_w^\pm, v, t) = & \phi(s_B^\pm, v, t) + \int_{s_B^\pm}^{s_w^\pm} \left\{ -\vec{q}_{in} \cdot \vec{s} + V_v \cos \psi \right. \\ & \left. + \sin \psi \sqrt{|\vec{q}_c|^2 - V_v^2} \right\} ds; \quad s_B^\pm \leq s_w^\pm \leq s_T^\pm \end{aligned} \quad (2.30)$$

where s_B^\pm and s_T^\pm denote the trailing edge of the blade and of the closing zone, respectively. The quantity $\phi(s_B^\pm, v, t)$ is the perturbation potential at the blade trailing

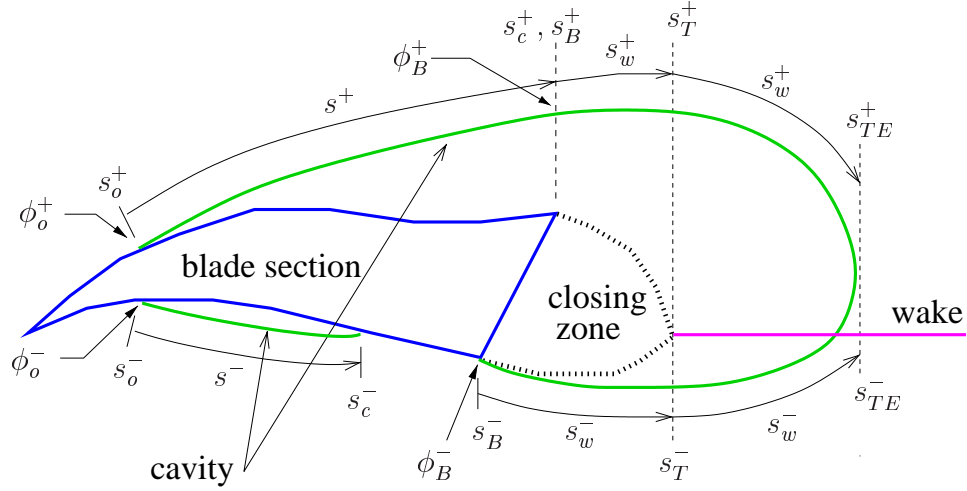


Figure 2.15: Application of the dynamic boundary condition for a supercavitating blade section.

edge. A schematic representation of the above variables is shown in Fig. 2.15.

If the blade section is partially cavitating or fully wetted, $\phi(s_B^\pm, v, t)$ is given via cubic extrapolation of the unknown potentials on the wetted blade panels adjacent to the blade trailing edge:

$$\begin{aligned} \phi(s_B^\pm, v, t) &= D_1^\pm(m, t)\phi_a^\pm(m, t) + D_2^\pm(m, t)\phi_b^\pm(m, t) \\ &+ D_3^\pm(m, t)\phi_c^\pm(m, t) + D_4^\pm(m, t)\frac{\partial\phi}{\partial s}(s_B^\pm, v, t) \end{aligned} \quad (2.31)$$

where $D_1^\pm(m, t), \dots, D_4^\pm(m, t)$ are the extrapolation coefficients for closing zone panels on radial strip m at time t . As shown in Fig. 2.16, $\phi_a^\pm(m, t), \dots, \phi_c^\pm(m, t)$ represent the unknown potentials on the wetted blade panels upstream of the blade trailing edge. The quantity $\frac{\partial\phi}{\partial s}(s_B^\pm, v, t)$ is the tangential component of the perturbation velocity at the blade trailing edge.

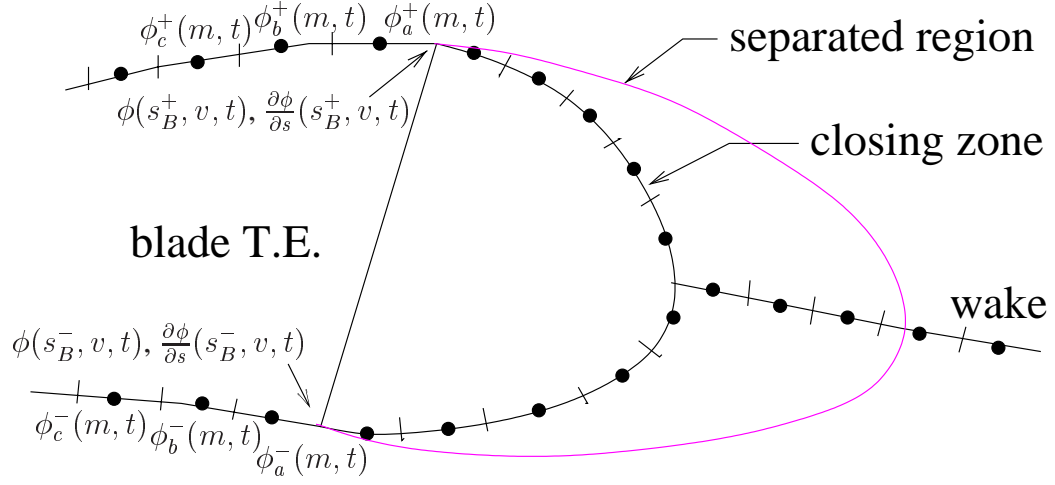


Figure 2.16: Extrapolation of the potential at the blade trailing edge for a fully wetted or partially cavitating supercavitating blade section.

On the other hand, if the blade section is supercavitating, then the separated region is part of the cavity. Thus, the perturbation potential at the blade trailing edge, $\phi(s_B^\pm, v, t)$, can be written as:

$$\begin{aligned} \phi(s_B^\pm, v, t) &= \phi(s_c^\pm, v, t) = \phi(s_o^\pm, v, t) \\ &+ \int_{s_o^\pm}^{s_c^\pm} \{-\vec{q}_{in} \cdot \vec{s} + V_v \cos \psi + \sin \psi \sqrt{|\vec{q}_c|^2 - V_v^2}\} ds \end{aligned} \quad (2.32)$$

For wake panels that are overlapped by the separated region or the supercavity, the perturbation potential is determined as follows:

$$\begin{aligned} \phi^\pm(s_w^\pm, v, t) &= \phi^\pm(s_B^\pm, v, t) \\ &+ \int_{s_B^\pm}^{s_w^\pm} \{-\vec{q}_{in} \cdot \vec{s} + |\vec{q}_c|\} ds; \quad s_B^\pm \leq s_w^\pm \leq s_{TE}^\pm \end{aligned} \quad (2.33)$$

where s_T and s_{TE} represent the arclength from the trailing edge of the blade section to the trailing edge of the closing zone and of the separated region, respectively.

- *Separated Region Closure Condition*

If the blade section is supercavitating, then the separated region is part of the cavitation bubble, which is governed by Eqn. 2.29. If the blade section is fully wetted or partially cavitating, then the separated region must detach from the blade trailing edge (i.e. $h_{sr}^{\pm}(1, m, k) = 0$) and extend into the wake panels. In addition, the following closure condition must be satisfied to ensure the separated region closes at its trailing edge:

$$\delta_{sr}(l_{sr}(r, t); r, \sigma_n) \equiv h_{sr}(l_{sr}(r, t), r, t) = 0 \quad (2.34)$$

where $l_{sr}^{\pm}(r, t)$ and $\delta_{sr}^{\pm}(l_{sr}^{\pm}(r, t); r, \sigma_n)$ represent the separated region length and separated region trailing edge thickness, respectively, at radius r of time t . h_{sr} is the thickness of the separated region.

- *Cavity Detachment Search Criterion*

In addition to the criterion described in Section 2.4.3, the cavities are also required to detach prior to the actual blade trailing edge.

- *Pressure Integration*

For supercavitating propellers, the pressure acting on the thick blade trailing edge (shown in Fig. 2.17) must also be included in the force calculation. This is accomplished by multiplying the separated region pressure acting normal to the blade trailing edge with the trailing edge area.

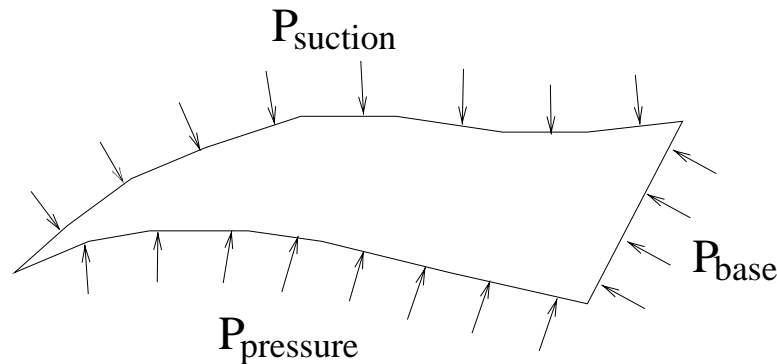


Figure 2.17: Pressure integration over a blade section with non-zero trailing edge thickness.

2.6.1 Numerical Validation

Cavitation patterns on supercavitating propellers that can be predicted by the present method are shown in Fig. 2.18. To verify the treatment for supercavitating propellers, numerical validations using 3-D hydrofoils are shown in this section.

Validation tests for a symmetric 3-D hydrofoil with non-zero trailing edge thickness under fully wetted, partially cavitating, and supercavitating conditions are shown in Figs 2.19 to 2.21. The cross section of the hydrofoil is modified from that of a NACA66 thickness distribution with NACA $a=0.8$ mean camber line. The foil has zero camber ($f_{\text{max}}/C = 0$), and the maximum thickness to chord ratio (T_{max}/C) is 0.05. The thickness to chord ratio at the foil trailing edge (T_{TE}/C) is 0.02. As expected for a symmetric hydrofoil at zero angle of attack ($\alpha = 0$), the pressure and cavity shape are identical on both sides of the foil surface. In addition, the smooth detachment condition is satisfied in all cases.

An additional validation test using a pair of asymmetric hydrofoils at equal

and opposite angle of attack ($\alpha = \pm 1^\circ$) and camber distribution ($f_{max}/C = \pm 0.02$) is shown in Fig. 2.22. As expected, the predicted pressures and cavity planforms are mirror images of each other for the hydrofoil pair.

To further validate the method, the influence of the closing zone length on the pressure and cavity shape is shown in Fig. 2.23. Since the entire closing zone is inside the separated region, the length of the closing zone should not affect the solution, which is confirmed by Fig. 2.23. Note that the small difference in the cavity shape in the wake region is due to the linearization of the supercavitating wake.

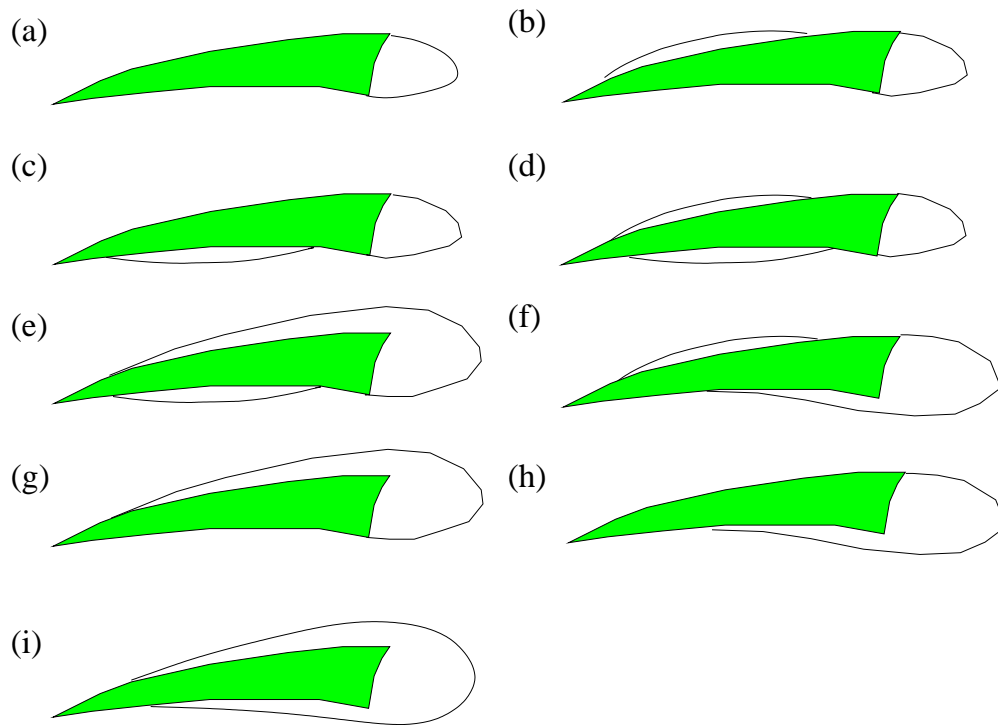


Figure 2.18: Cavitation patterns on supercavitating propellers that can be predicted by the present method.

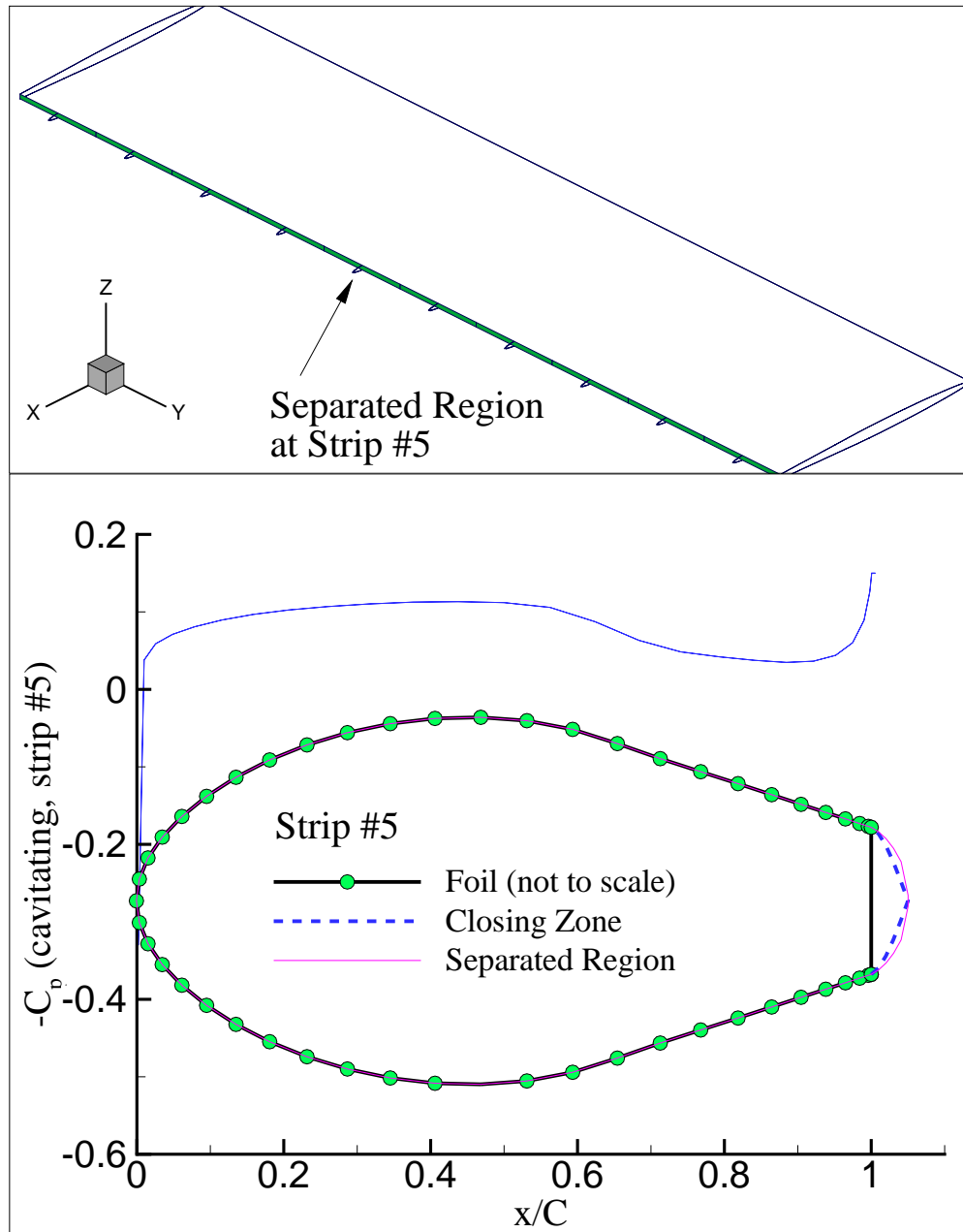


Figure 2.19: Validation for treatment of blade sections with non-zero thickness subjected to fully wetted conditions. $\sigma_v=0.15$, $T_{max}/C=0.05$, $T_{TE}/C = 0.02$, $f_{max}/C=0$, $\alpha=0^\circ$. Uniform inflow.

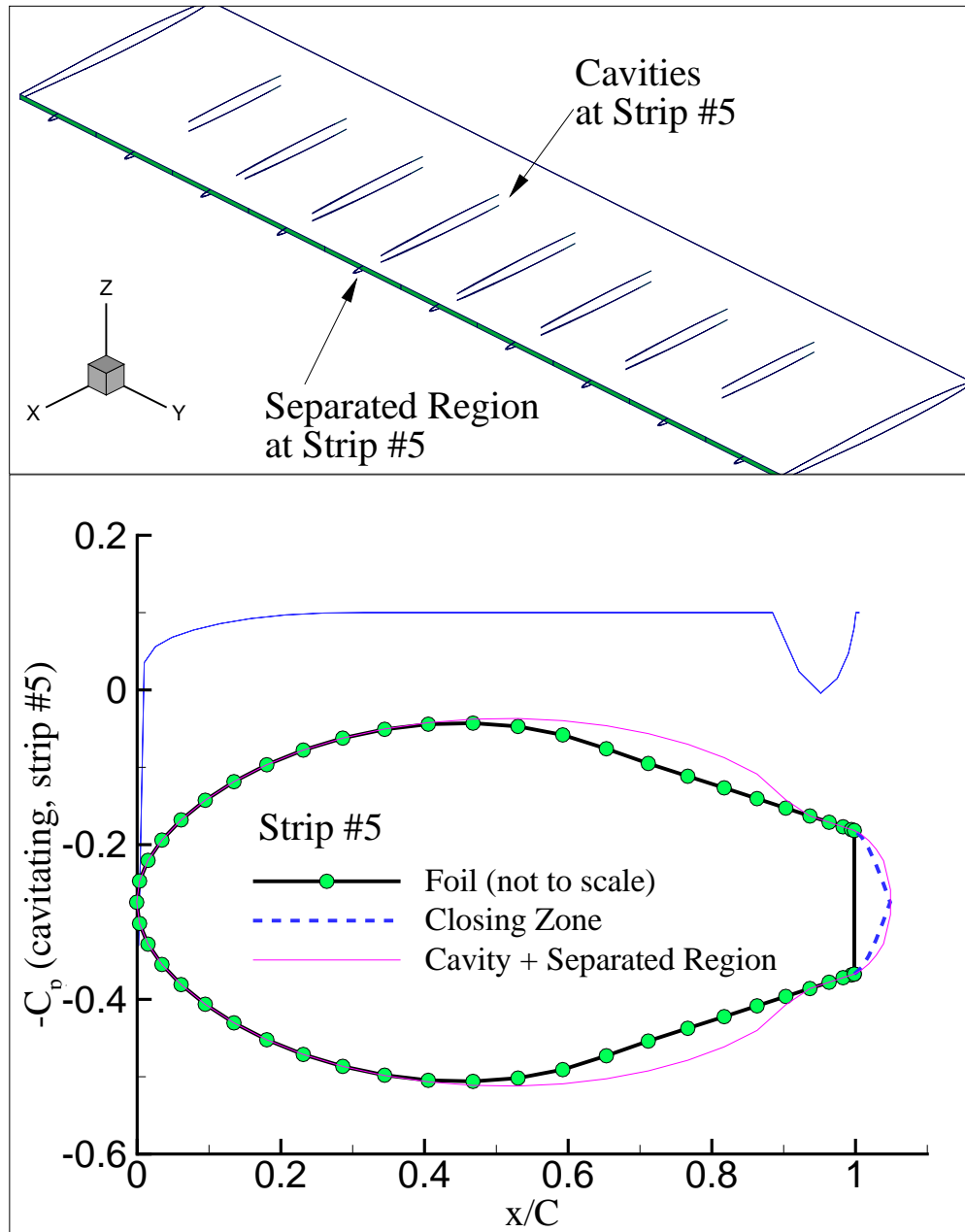


Figure 2.20: Validation for treatment of blade sections with non-zero thickness subjected to partially cavitating conditions. $\sigma_v=0.10$, $T_{max}/C = 0.05$, $T_{TE}/C=0.02$, $f_{max}/C=0$, $\alpha=0^\circ$. Uniform inflow.

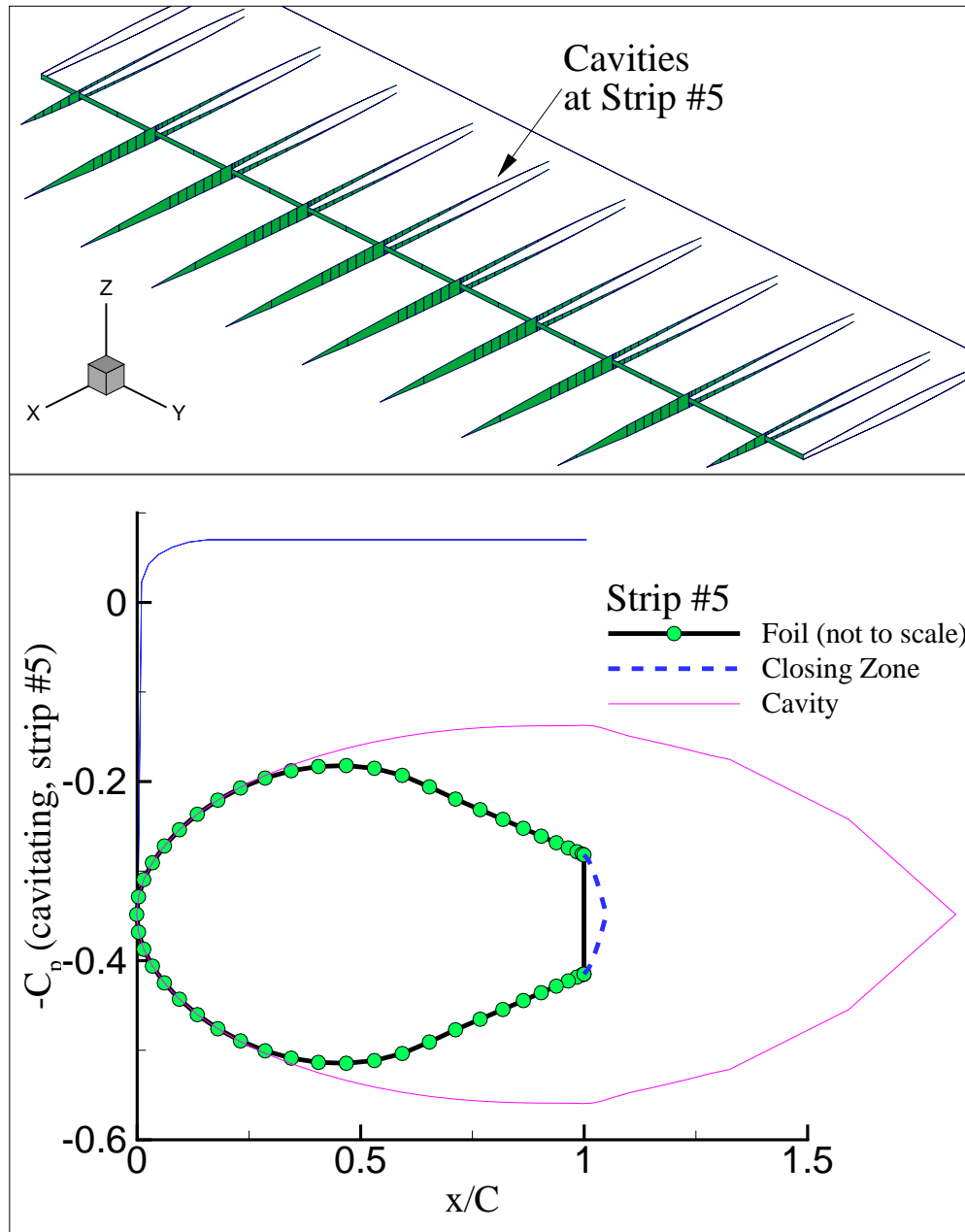
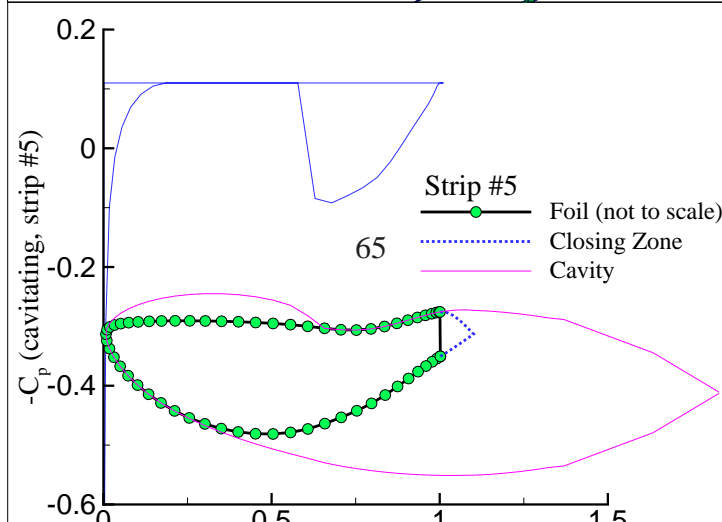
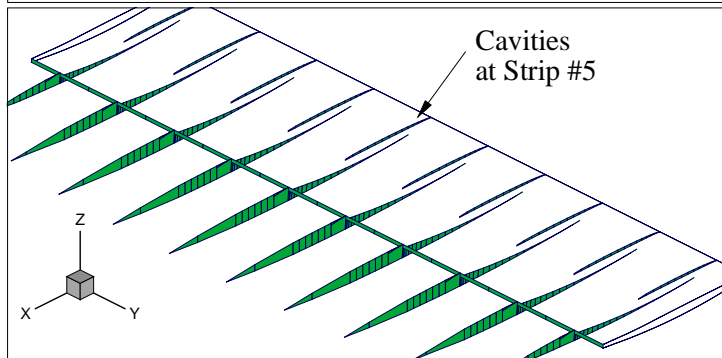
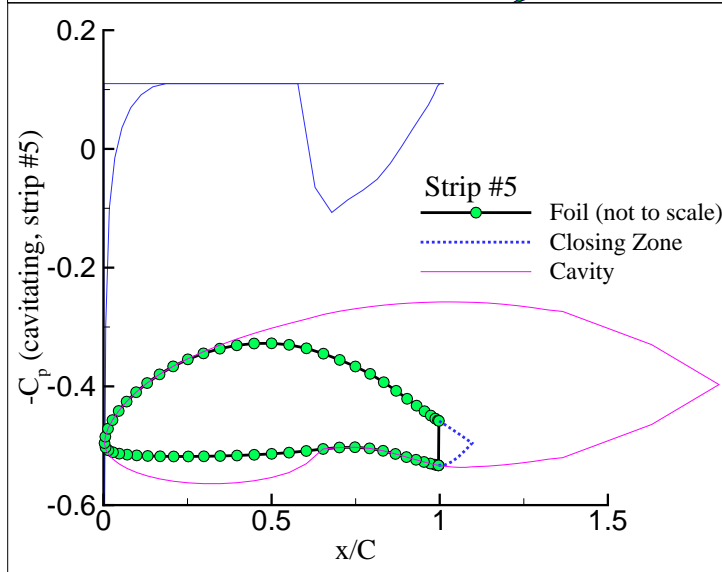
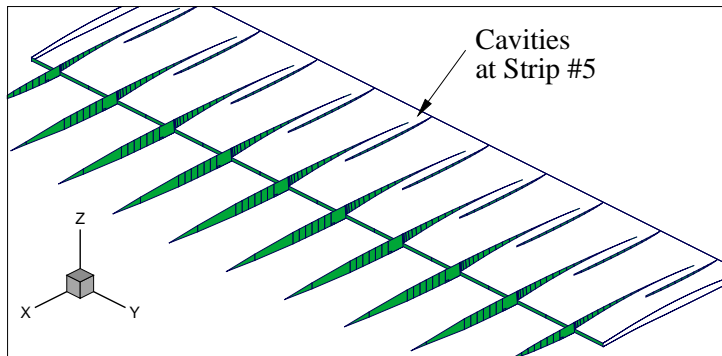


Figure 2.21: Validation for treatment of blade sections with non-zero thickness subjected to supercavitating conditions. $\sigma_v=0.07$, $T_{max}/C = 0.05$, $T_{TE}/C=0.02$, $f_{max}/C=0$, $\alpha=0^\circ$. Uniform inflow.



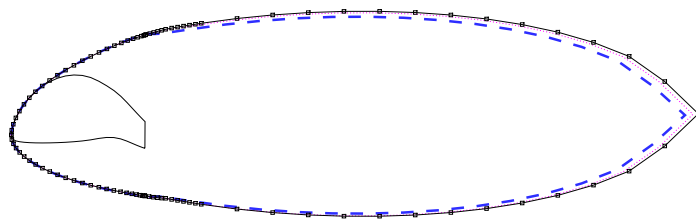
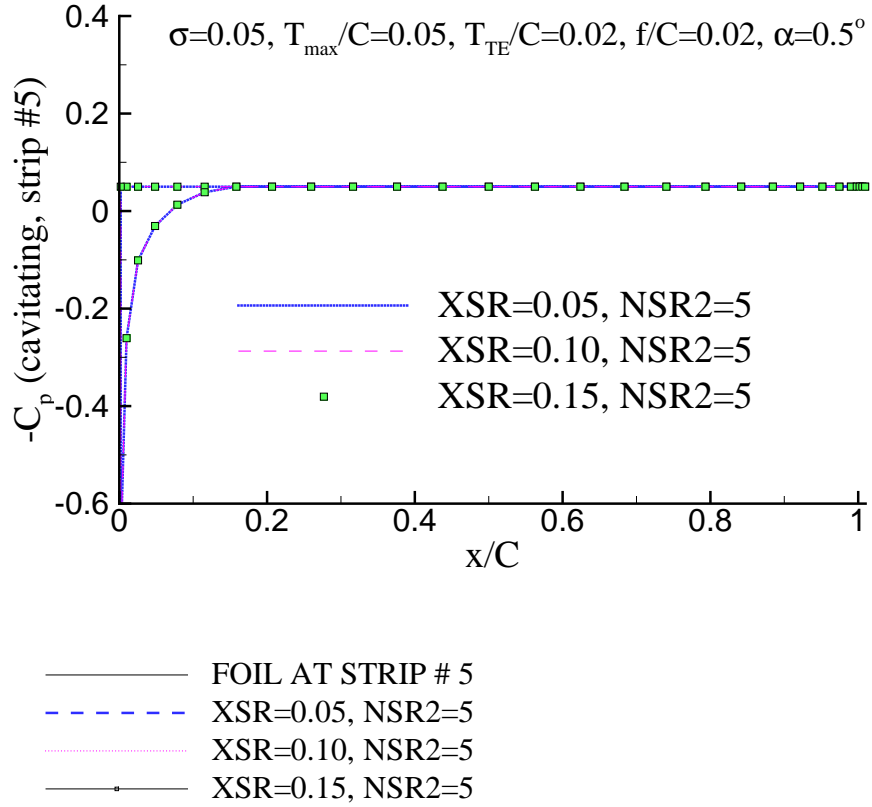


Figure 2.23: The influence of the closing zone length on the pressure and cavity shape for a supercavitating blade section. XSR is the ratio of the lengths of the closing zone and the chord. $NSR2$ is the number of panels on each side of the closing zone per each radial strip. $\sigma_v=0.15, T_{\max}/C = 0.05, T_{TE}/C = 0.02, f_{\max}/C=0, \alpha=0^\circ$. Uniform inflow.

2.7 Convergence Studies

In order to validate the method, convergence studies are performed. In this section, the sensitivity of the solution to varying number of propeller revolutions, panel discretization, and time step size are presented for two different fully submerged propellers.

2.7.1 Propeller DTMB N4148 - Traditional Propeller with Back Cavitation

The convergence of the method is first studied for propeller DTMB N4148, the geometry of which is given in [Kinnas and Pyo 1999], and is shown in Fig. 2.24. It is a conventional fully submerged propeller with 3-blades. The inflow wake, which corresponds to the wake in [Mishima et al. 1995] with the effects of the tunnel walls and vortical inflow/propeller interactions (non-axisymmetric “effective” wake) accounted for by using the method of [Kinnas et al. 2000; Choi 2000], is also presented in Fig. 2.24. For the given flow conditions ($\sigma_n = 2.576$, $J_s = 0.954$, and $F_r = 9.159$), the dominant cavitation pattern for this propeller is leading edge back cavitation.

Convergence with Number of Revolutions

As explained in Section 2.4.1, the method accounts for the effect of other blades on the key blade in a progressive manner. Thus, the solution obtained by the method depends on the number of revolutions. Figure 2.25 shows the convergence of individual blade forces with number of revolutions. As shown on the figure, the solution converged at the fourth revolution for this particular case. It should

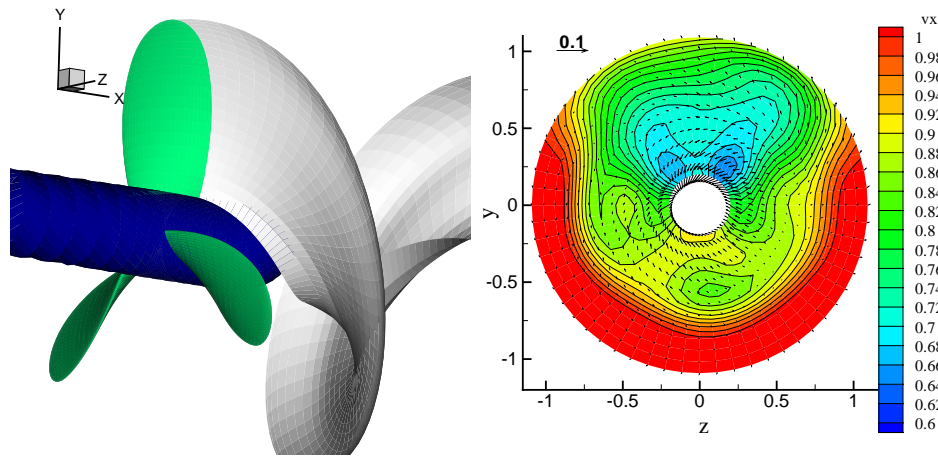


Figure 2.24: Geometry and inflow wake of propeller DTMB4148.

be noted that the sudden change from the second to the third revolution is due to the activation of the unsteady term, $\frac{\partial \phi}{\partial t}$, after two revolutions are completed. The unsteady term is not activated in the first two revolutions because the solution need time to stabilize from the wrong initial guess of cavity planform and wake dipole distributions.

Convergence with Time Step Size

Since the problem is unsteady, the numerical solution depends on the time step size, which is expressed in terms of blade angle increment, $\Delta\theta$, in PROPCAV. Three blade angle increments are used: 4° , 6° , and 8° . The effect of different blade angle increments on the predicted individual blade forces and cavity planforms are shown in Figs. 2.26 and 2.27, respectively. As shown in the figures, the results are not very sensitive to blade angle increments for this particular case.

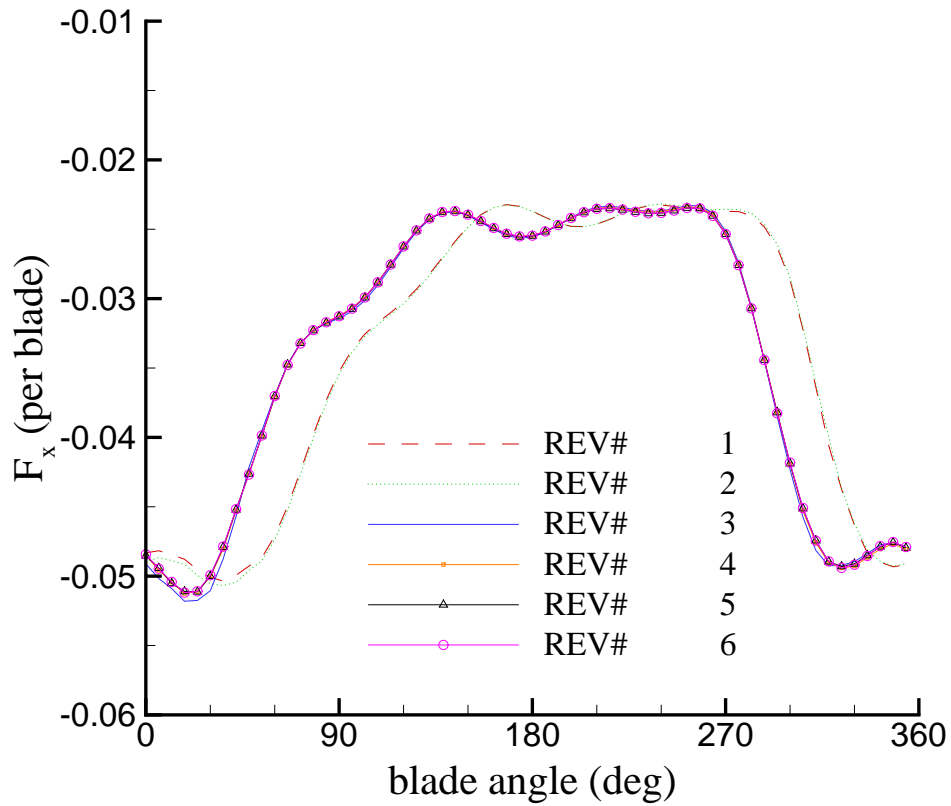


Figure 2.25: Convergence of individual blade forces with number of propeller revolutions for propeller DTMB4148. 60x20 panels. $\Delta\theta = 6^\circ$. $\sigma_n = 2.576$. $J_s = 0.954$. $F_r = 9.159$.

Convergence with Mesh Size

In addition to the number of propeller revolutions and blade angle increments, panel discretization also affects the convergence of the solution. Figures 2.28 and 2.29 show the dependence of individual blade forces and cavity planforms, respectively, on the panel discretization. As shown in the figures, the results are slightly more sensitive to mesh size than blade angle increment.

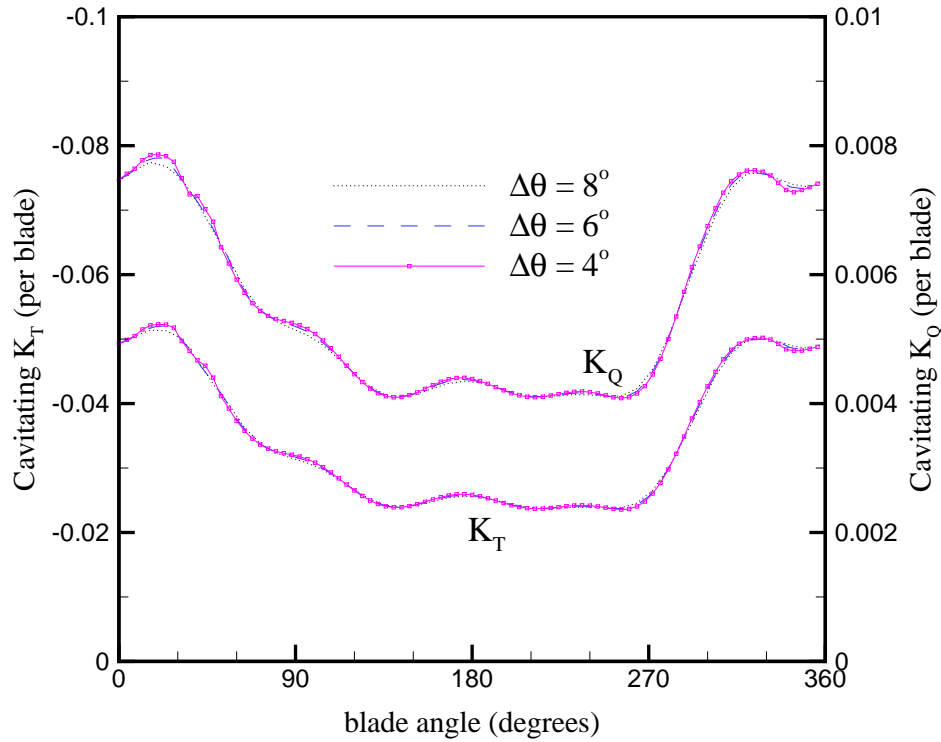


Figure 2.26: Convergence of cavitating blade force coefficients (per blade) with blade angle increments for propeller DTMB N4148. 60x20 panels. $\sigma_n = 2.576$. $J_s = 0.954$. $F_r = 9.159$.

2.7.2 Propeller SRI - Supercavitating Propeller

In order to validate the treatment for supercavitating propellers, convergence tests for propeller M.P.No.345 (SRI) are presented. The discretized propeller geometry and a drawing of the blade sections with the corresponding closing zones are shown in Fig. 2.30. The propeller is subjected to a non-axisymmetric inflow with constant velocity and a 3° inclination angle. The flow conditions are as follows:

$\sigma_n=0.784$, $J_s=1.4$, $F_r=5$. The dominant cavitation pattern for this propeller is mid-chord supercavitation on the suction side and leading edge partial cavitation on the pressure side.

Convergence with Number of Revolutions

The convergence of the individual blade forces with number of propeller revolutions for propeller SRI is shown in Fig. 2.31. It should be noted that the unsteady term ($\frac{\partial\phi}{\partial t}$) is not activated until the fourth revolution for the case of supercavitating propellers to avoid stability problems.

Convergence with Time Step Size

The convergence of the individual blade forces with time step size are shown in Fig. 2.32. Only two blade angle increments are presented: 4° and 6° . Higher blade angle increments were attempted, but the solution was unstable due to the combination of large time step size and small panel size.

Convergence with Mesh Size

The convergence of the individual blade forces with three different panel discretization is shown in Fig. 2.33. For the given flow conditions, the solution is not very sensitive to the shown space discretizations.

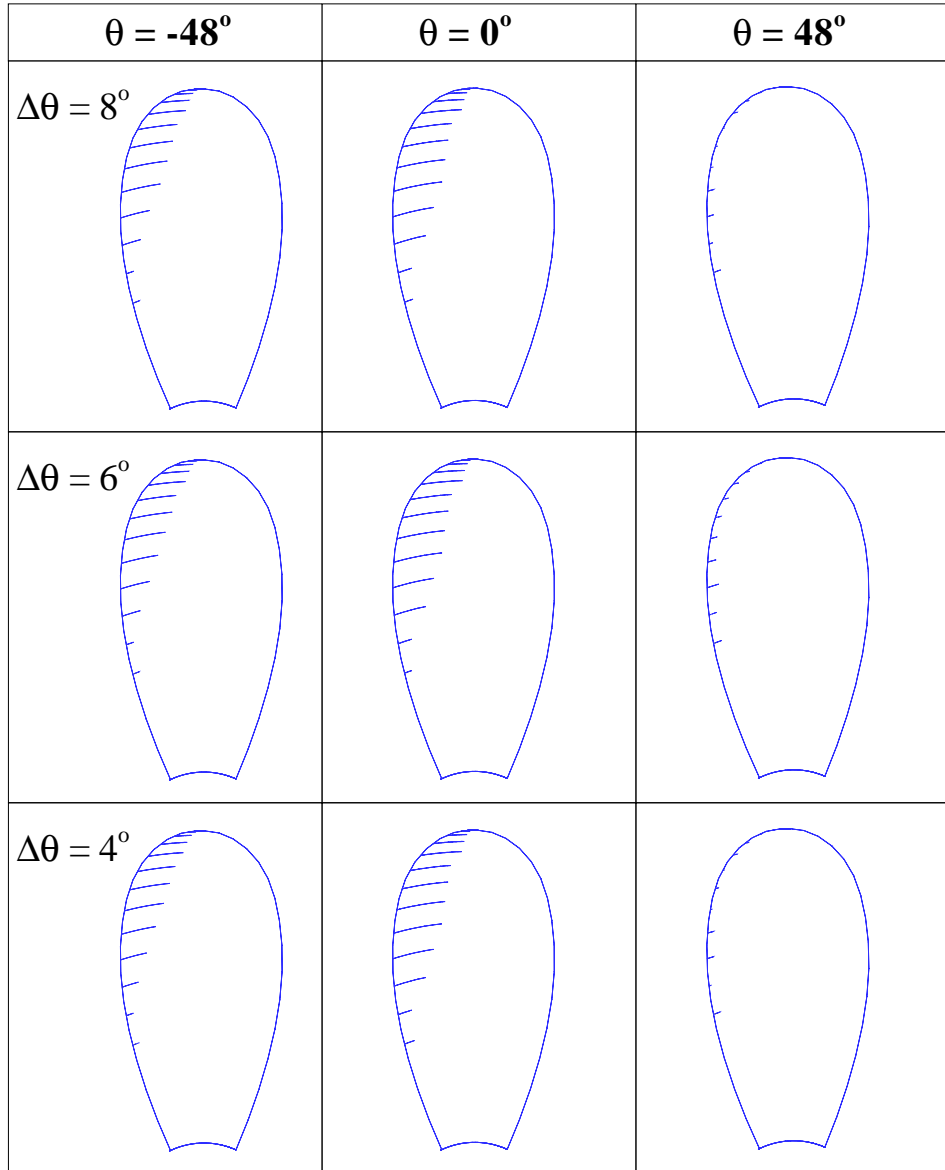


Figure 2.27: Convergence of cavity planforms with blade angle increments for propeller DTMB N4148. 60x20 panels. $\sigma_n = 2.576$. $J_s = 0.954$. $F_r = 9.159$.

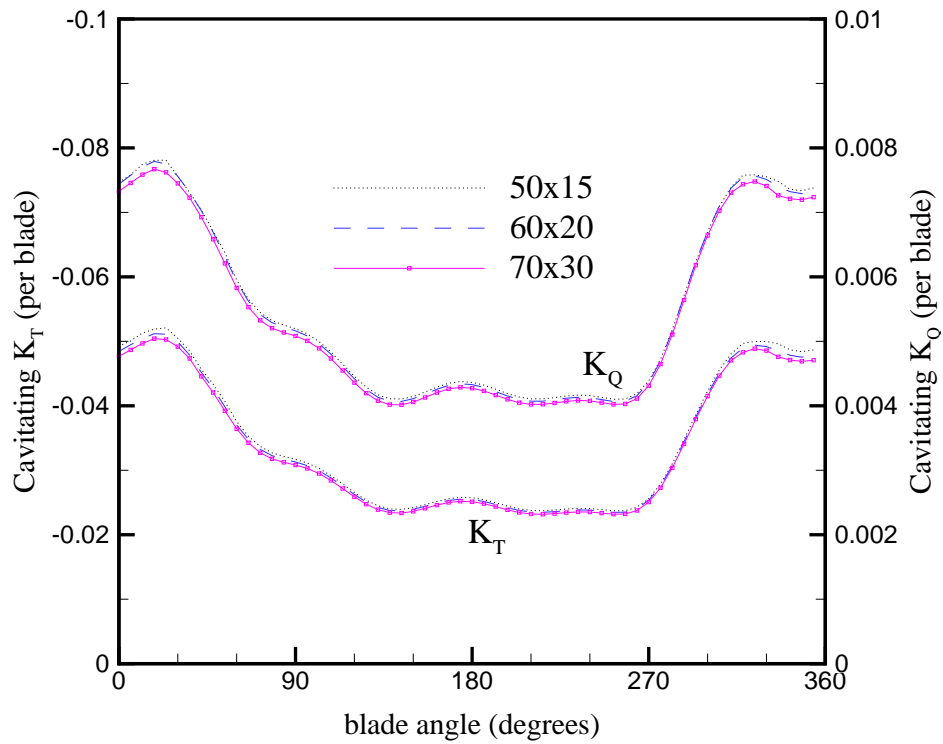


Figure 2.28: Convergence of cavitating blade force coefficients (per blade) with mesh size for propeller DTMB N4148. $\Delta\theta = 6^\circ$. $\sigma_n = 2.576$. $J_s = 0.954$. $F_r = 9.159$.

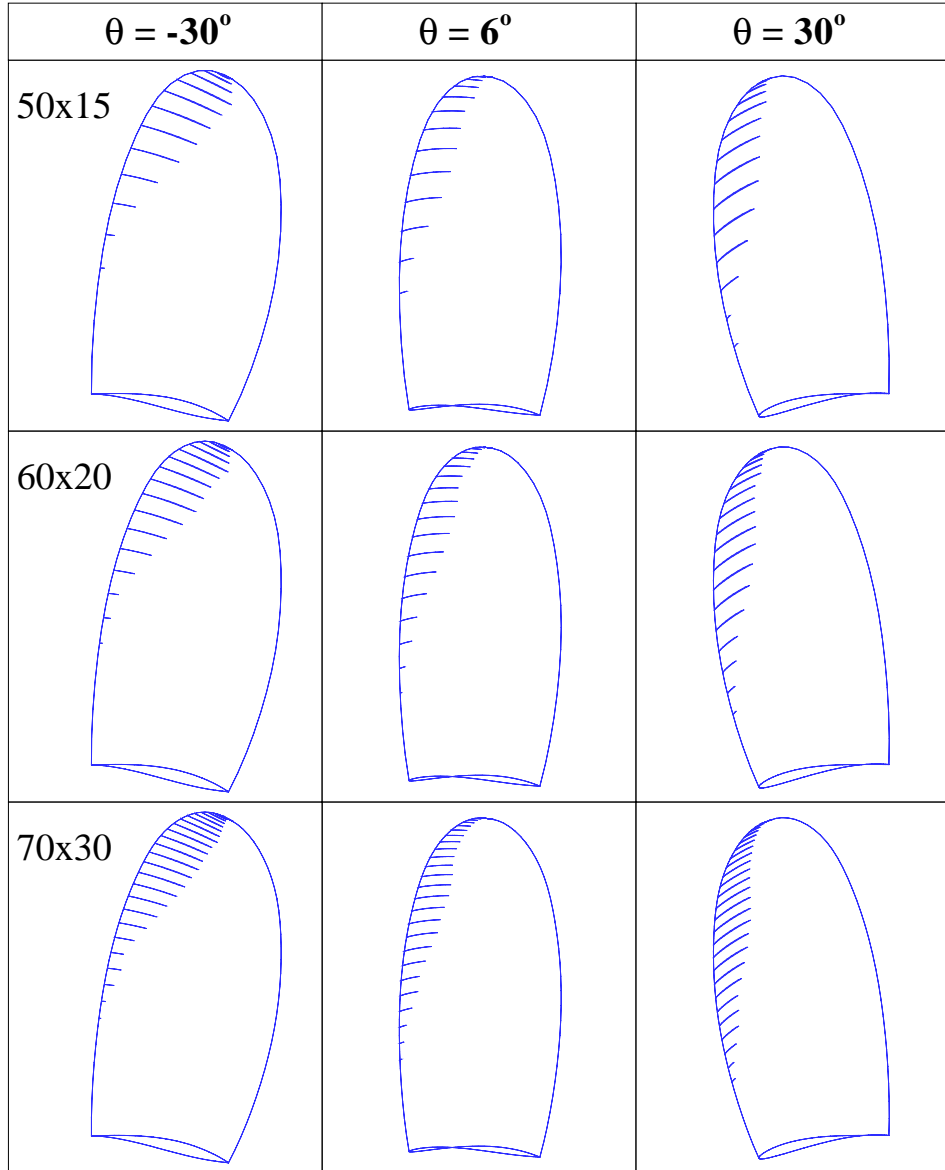


Figure 2.29: Convergence of cavity planforms with mesh size for propeller DTMB N4148. $\Delta\theta = 6^\circ$. $\sigma_n = 2.576$. $J_s = 0.954$. $F_r = 9.159$.

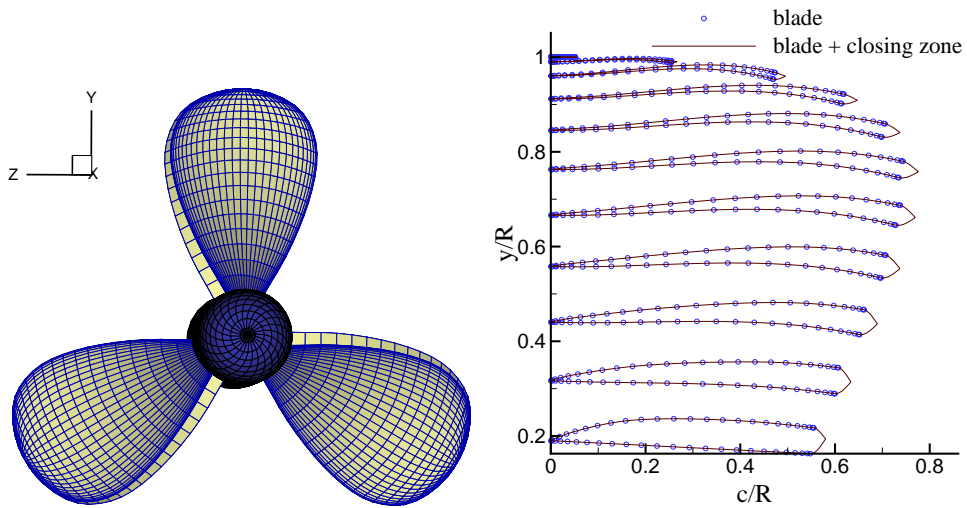


Figure 2.30: Left: Discretized propeller geometry. Right: Blade section and closing zone geometry. Propeller SRI. uniform inflow.

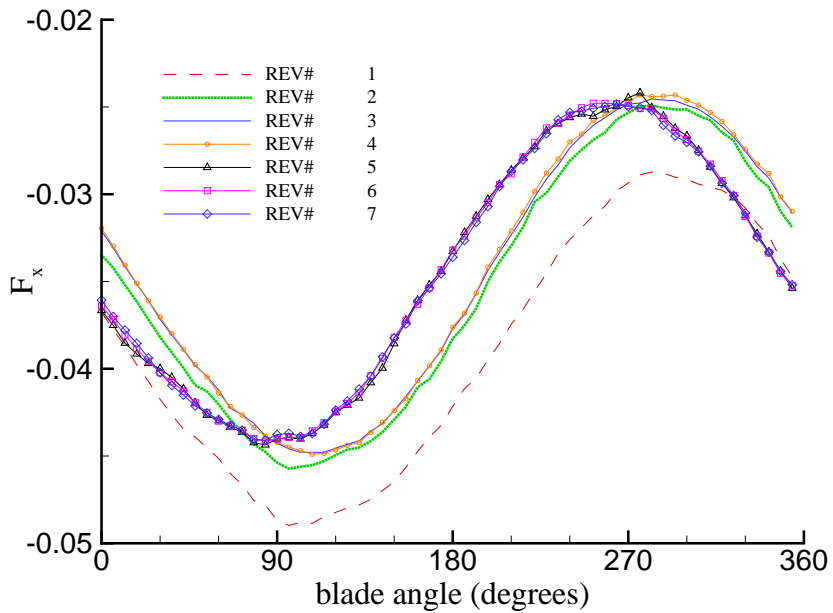


Figure 2.31: Convergence of thrust coefficient (per blade) with number of revolutions. Propeller SRI. $\sigma_n=0.784$. $J_s=1.4$. $F_r=5.0$. 3° inclination. 60×20 panels. $\Delta\theta = 6^\circ$.

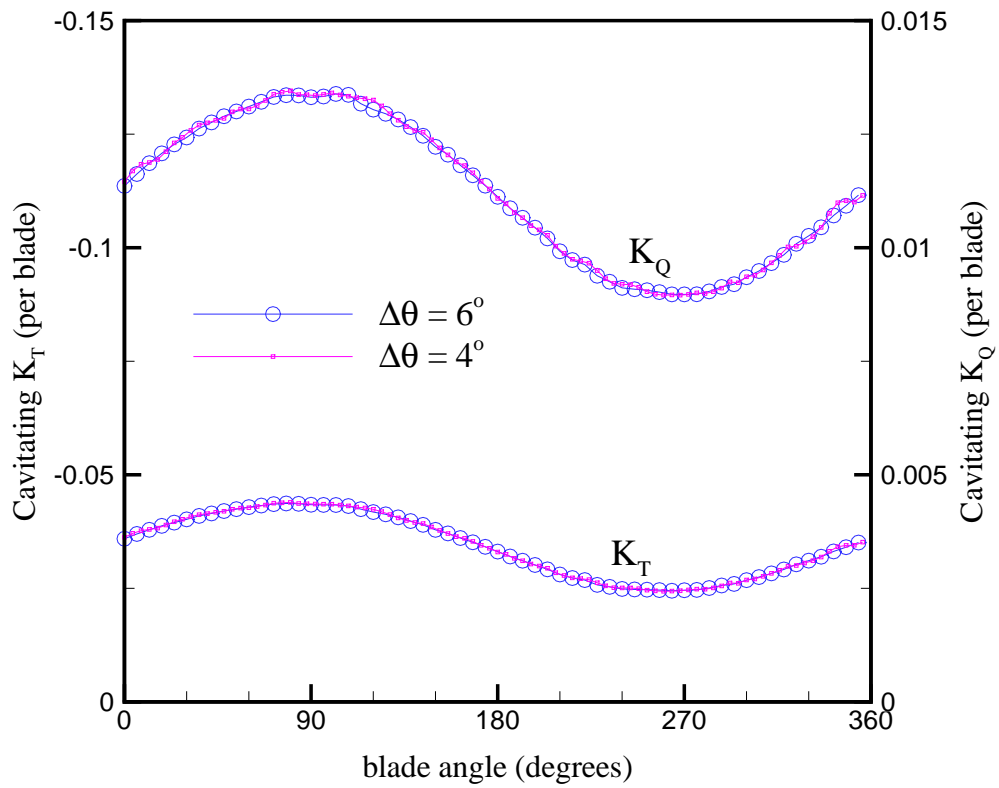


Figure 2.32: Convergence of thrust and torque coefficient (per blade) with blade angle increment. Propeller SRI. $\sigma_n=0.784$. $J_s=1.4$. $F_r=5.0$. 3° inclination. 70x30 panels.

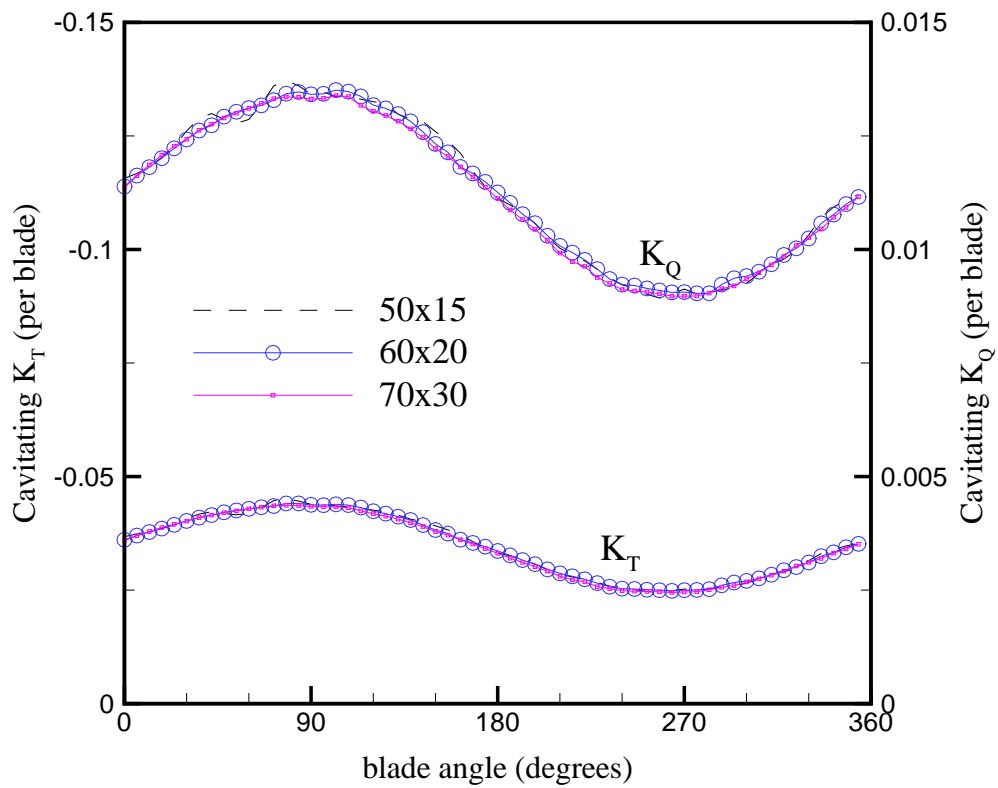


Figure 2.33: Convergence of thrust and torque coefficient (per blade) with grid discretization. Propeller SRI. $\sigma_n=0.784$. $J_s=1.4$. $F_r=5.0$. 3° inclination. $\Delta\theta = 8^\circ$.

2.8 Validation with Experiments and other Numerical Methods

In order to validate the method, numerical predictions are compared with experimental measurements and observations for five different propellers. The consistency of the method is also tested by comparing the numerical predictions by PROPCAV with those predicted by MPUF-3A, a vortex-lattice method. The author would like to thank Mr. HanSeong Lee for performing all the MPUF-3A predictions shown in this section.

2.8.1 Propeller DTMB 5168 - Five Bladed, Highly-Skewed Propeller

Comparisons of thrust and torque coefficients measured in experiments [Jesup 1996], and predictions by PROPCAV and MPUF-3A, for propeller DTMB 5168 in fully wetted, uniform inflow are shown in Fig. 2.34. The geometry of the propeller with the finite hub model⁵ is also shown in Fig. 2.34. Notice that PROPCAV with the finite hub model yields more accurate force predictions. In addition, PROPCAV with the infinite hub model predicts similar results to those obtained by MPUF-3A. This is expected because MPUF-3A uses a simplified hub image model that assumes the hub to be of constant radius and infinite length, which is equivalent to the infinite hub model in PROPCAV.

⁵In PROPCAV, the hub can be open or closed upstream and downstream. The radius of the hub can also be varied in the streamwise direction. For the open end, a dipole disk is used to represent the part that extends to infinity.

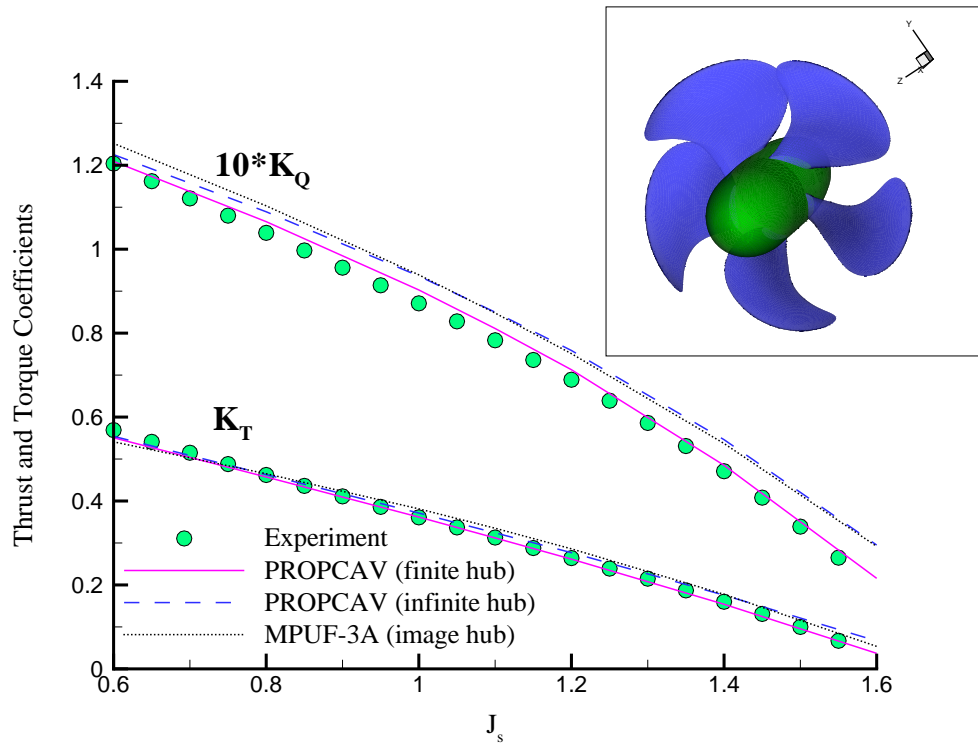


Figure 2.34: Geometry of propeller DTMB5168. Also shown are the predicted and measured K_T and K_Q for different advance coefficients. PROPCAV: 80x60 Panels. MPUF-3A: 20x18 panels.

2.8.2 Propeller DTMB 4119 - Three Bladed, Zero-Skew and Zero-Rake Propeller

Figure 2.35 shows the comparison of unsteady thrust and torque coefficients obtained from experiment [Jessup 1990], PROPCAV, and MPUF-3A for propeller DTMB 4119. The propeller was subjected to a non-axisymmetric 3-cycle wake [Jessup 1990] (also shown in Fig. 2.35) in fully wetted flow. As shown in Fig. 2.35, both numerical codes did well in predicting the unsteady blade force harmonics.

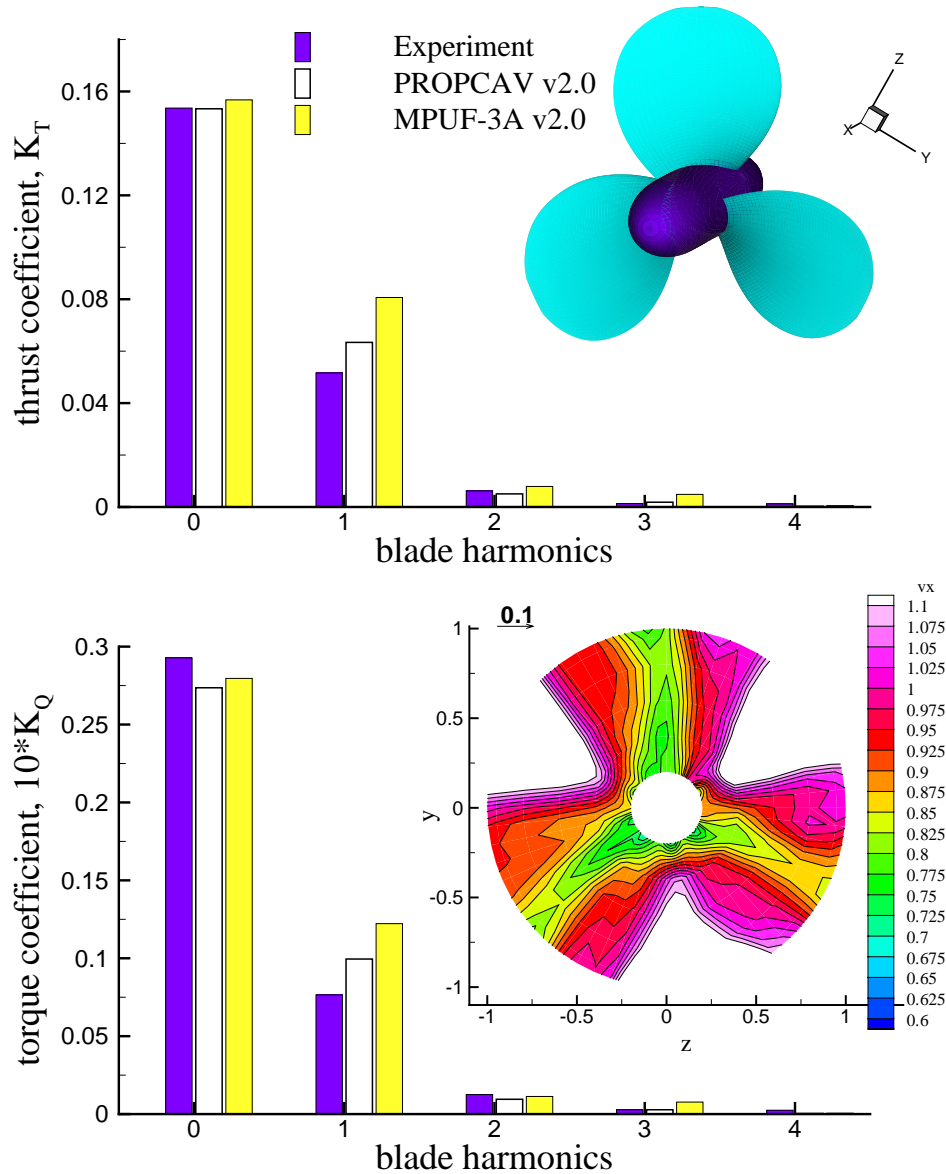


Figure 2.35: Geometry and inflow wake of propeller DTMB4119. Also shown are the predicted and measured K_T and K_Q for different blade harmonics. PROPCAV: 80x50 Panels. MPUF-3A: 40x27 panels

2.8.3 Propeller DTMB 4148 - Three Bladed, Zero-Skew and Zero-Rake Propeller

In the third set of experiment, PROPCAV is used to predict the cavity shape for propeller DTMB N4148 in a screen generated non-axisymmetric inflow inside a cavitation tunnel [Mishima et al. 1995]. The predicted cavity shapes from PROPCAV are shown in Fig. 2.36 together with photographs taken during the experiment. The flow conditions were as follows: $J_s = 0.9087$, $F_r = 9.159$, and $\sigma_n = 2.576$. The equivalent J_s , 0.957, for unbounded flow is obtained by matching the fully wetted thrust coefficient, K_T , with the measured K_T , 0.0993, from experiment. The inflow wake used in PROPCAV, which is shown in Fig. 2.24, corresponds to the wake in [Mishima et al. 1995] with the effects of the tunnel walls and vortical inflow/propeller interactions (non-axisymmetric “effective” wake) accounted by using the method of [Kinnas et al. 2000; Choi 2000].

As shown in Fig. 2.36, the numerical results agree relatively well with experimental observations except for the area near the blade tip. It should be noted that PROPCAV’s prediction in the blade tip region is unreliable because the current method does not include a tip-vortex cavity model. Furthermore, the current version of PROPCAV does not require cavity lengths at $r/R > 0.95$ to converge due to numerical difficulties very near the tip.

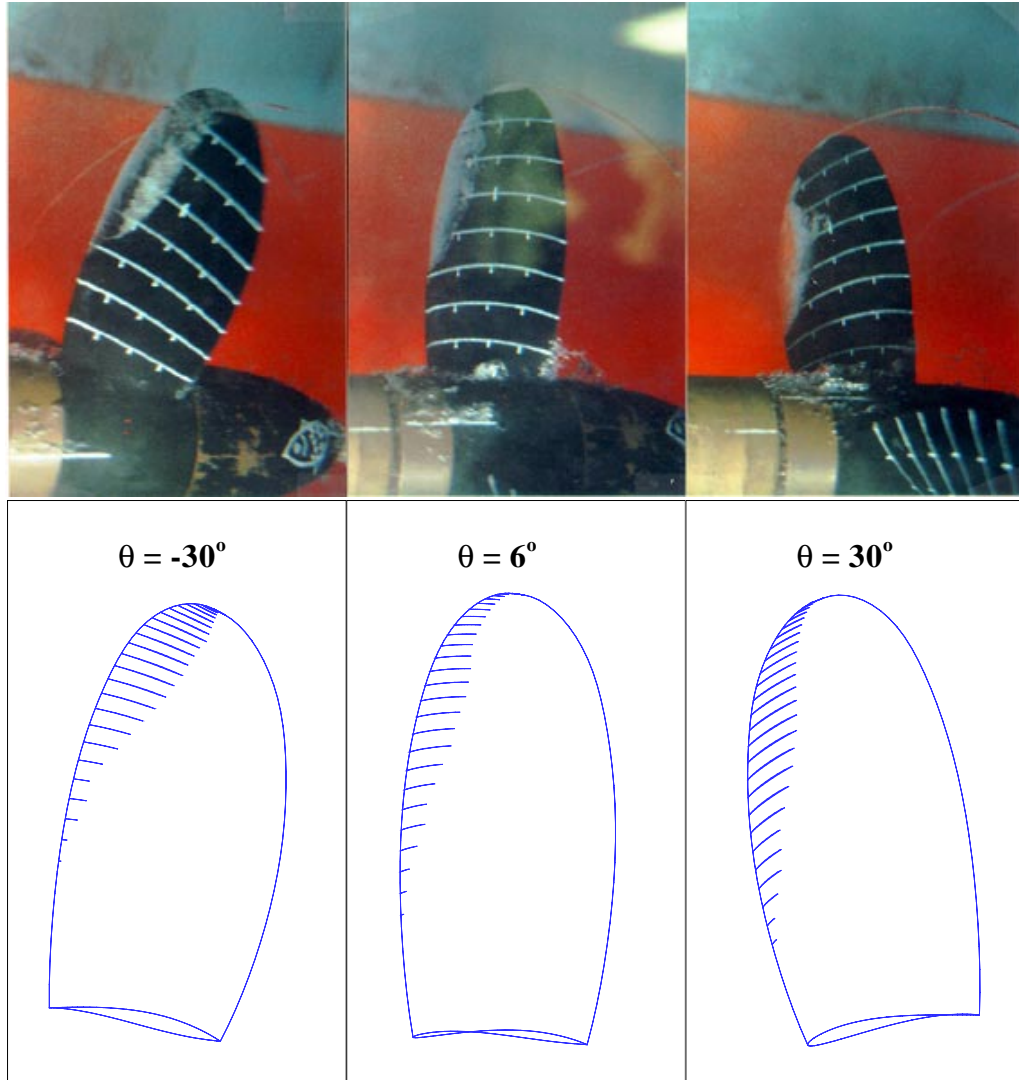


Figure 2.36: Comparison of PROPCAV's prediction (bottom) to experimental observations (top) for propeller DTMB4148. $J_s = 0.954$, $\sigma_n = 2.576$, $F_r = 9.159$, 70×30 panels, $\Delta\theta = 6^\circ$.

2.8.4 Propeller 4382 - Five Bladed, Non-Zero Skew and Non-Zero Rake Propeller

The fourth set of comparisons between experimental measurements and numerical predictions is for propeller 4382. The propeller geometry is given in [Boswell 1971; Cumming et al. 1972], and is shown in Fig. 2.37. Open water performance was measured at the NSRDC deep water basin, and are compared with numerical predictions by PROPCAV and MPUF-3A in Fig. 2.38. As shown in the figure, both methods compared well with experimental measurements.

Cavitation tests for propeller 4382 were conducted in a 24-in. cavitation tunnel at NSRDC [Boswell 1971]. One of the objectives of the experiment was to determine thrust breakdown due to cavitation. The thrust and torque breakdown curves for propeller 4382 at the design advance ratio ($J_A = V_A/nD = 0.889$)⁶ are shown in Fig. 2.39 along with numerical predictions by PROPCAV and MPUF-3A. Note that the numerical methods are in good agreement with each other, but both methods under-predicted in the cavitating region (i.e. $\sigma_v \leq 1.5$). This behavior is somewhat expected because the initial inception curves shown in [Cumming et al. 1972] indicated that the the breakdown at design J_A for propeller 4382 caused by bubble cavitation. Thus, numerical predictions are not expected to match that of experimental measurements in the cavitating region since both methods assumed sheet cavitation only.

Comparisons of predicted and measured thrust and torque coefficients as a function of advance ratio (J_A) and cavitation number ($\sigma_v = (P_o - P_v)/(0.5\rho V_A^2)$) are

⁶ V_A is the speed of advance of propeller in open water

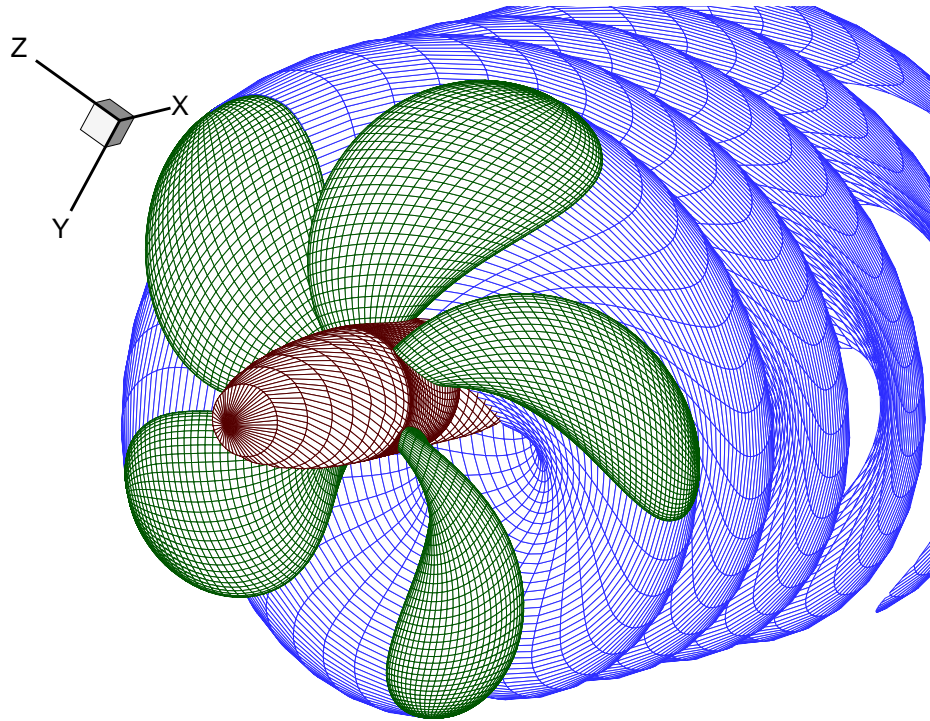


Figure 2.37: Propeller DTMB 4382 with paneled blades, hub, and trailing wake.

shown in Fig. 2.40. The corresponding cavity planform at $J_A = 0.7$ and $\sigma_v = 3.5$ predicted by PROPCAV and MPUF-3A is shown in Fig. 2.41. A sketch of the observed cavity pattern at the same flow condition is given in [Boswell 1971], and it agrees well with numerical predictions.

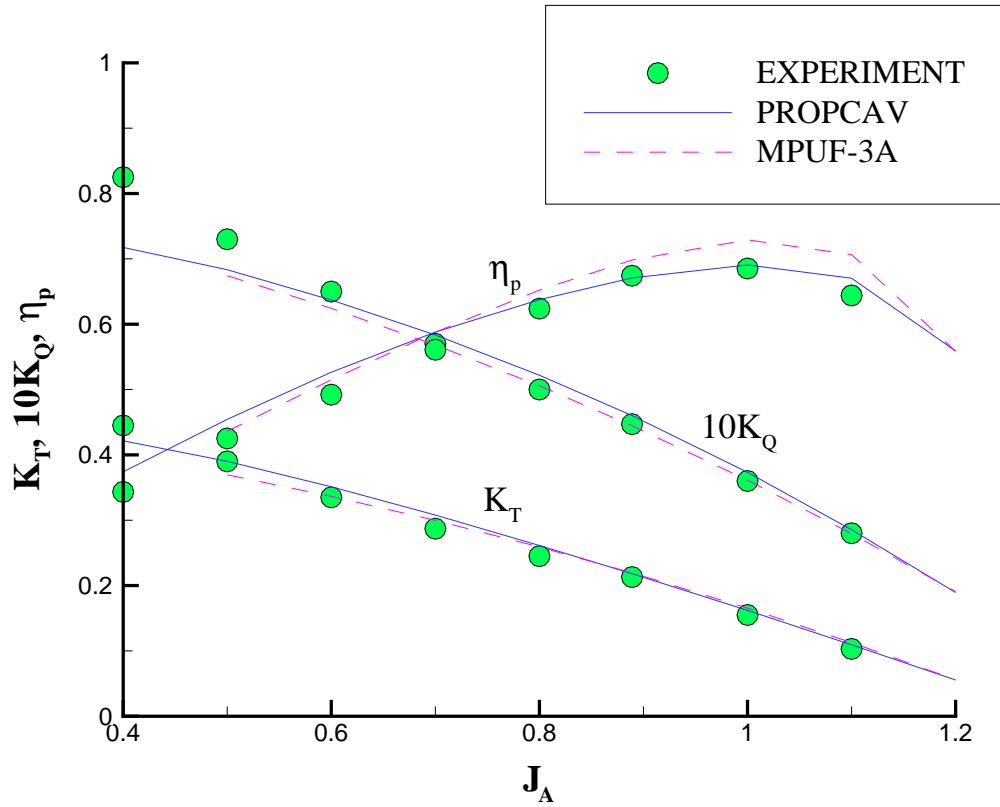


Figure 2.38: Open water performance predicted by PROPCAV, MPUF3A, and measured in experiments by [Boswell 1971]

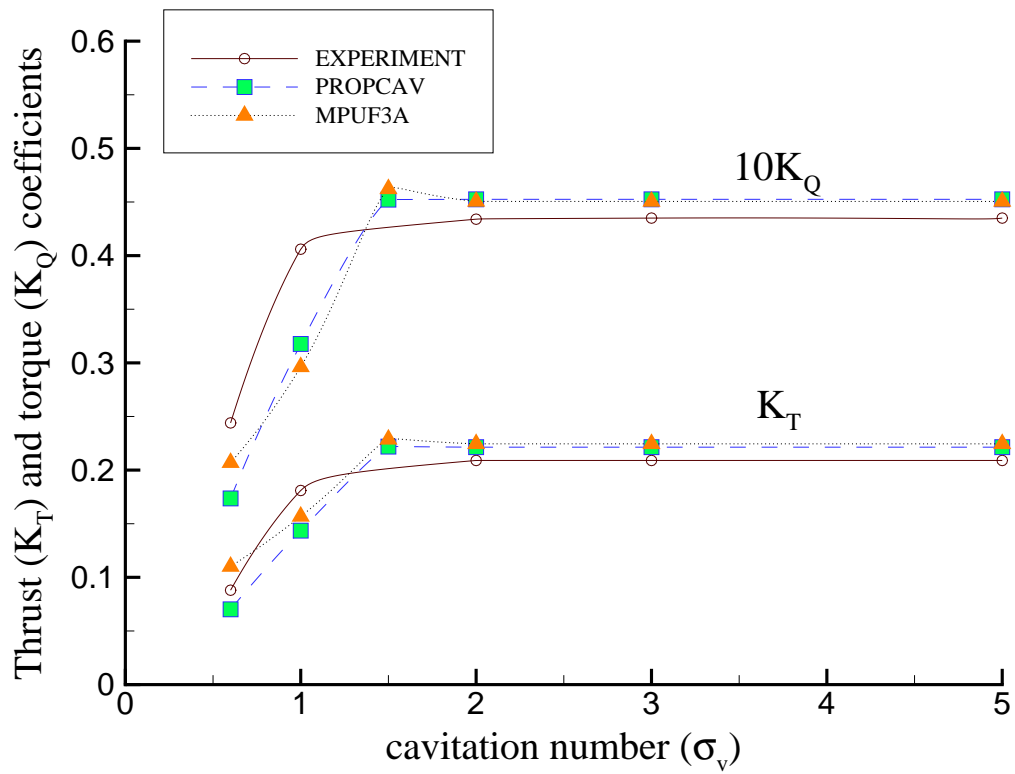


Figure 2.39: Predicted and measured thrust (K_T) and torque (K_Q) coefficients as a function of cavitation number (σ_v) at the design advance ratio ($J_A = 0.889$).

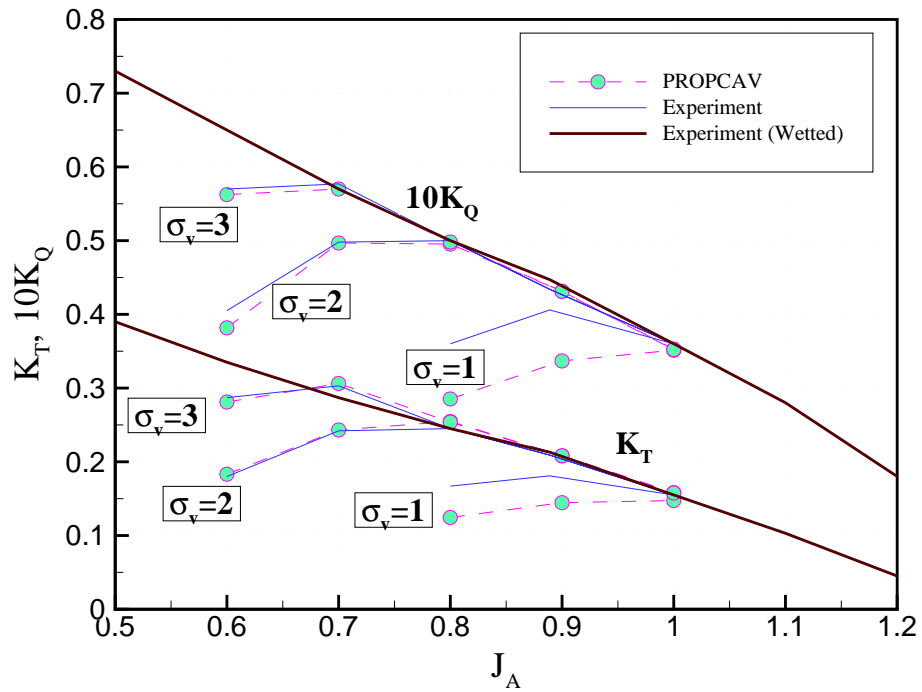


Figure 2.40: Predicted and measured thrust (K_T) and torque (K_Q) coefficients as a function of cavitation number (σ_v) and advance ratio (J_A).

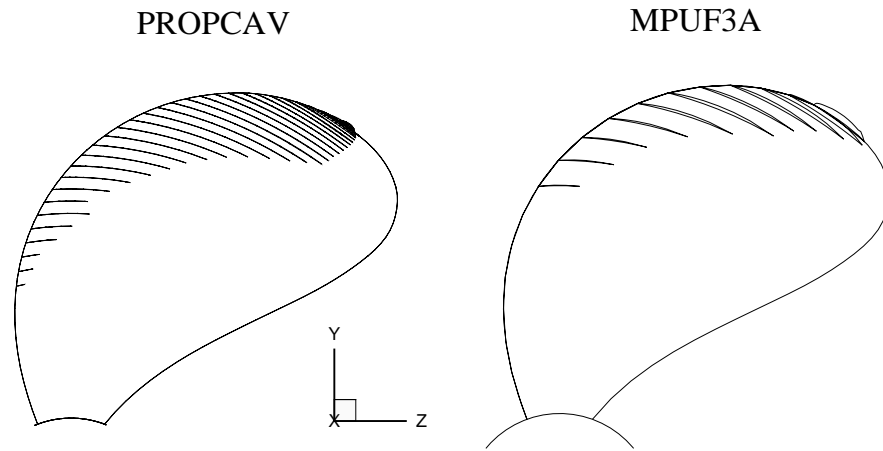


Figure 2.41: Predicted cavity planform at $J_A = 0.7$ and $\sigma_v = 3.5$ by PROPCAV and MPUF3A.

2.8.5 Propeller SRI - Three Bladed, Non-Zero Skew and Non-Zero Rake Supercavitating Propeller

To validate the treatment of supercavitating propellers, the predicted force coefficients are compared with experimental measurements [Matsuda et al. 1994] for a supercavitating propeller. The test geometry is M.P.No.345 (SRI), which is designed using SSPA charts under the following conditions: $J_A = 1.10$, $\sigma_v = 0.40$, and $K_T = 0.160$. The discretized propeller geometry, and a drawing of the blade sections with the corresponding closing zones are shown in Fig. 2.30. Comparisons of the predicted and measured thrust (K_T), torque (K_Q), and efficiency (η_p) are shown in Fig. 2.42. It is worth noting that at $J_A = 1.3$, there is substantial midchord detachment. Fig. 2.43 indicates that the detachment search condition is satisfied since the cavities have non-negative thickness and the pressures everywhere on the wetted blade surfaces are above the vapor pressure.

As shown in Fig. 2.42, the numerical predictions compared well with experimental measurements. To further validate the method, the convergence of the predicted cavity planforms, as well as the thrust and torque coefficients, with number of panels are shown in Fig. 2.44 for $J_A = 1.3$. As depicted in Fig. 2.44, the predicted results converged quickly with number of panels.

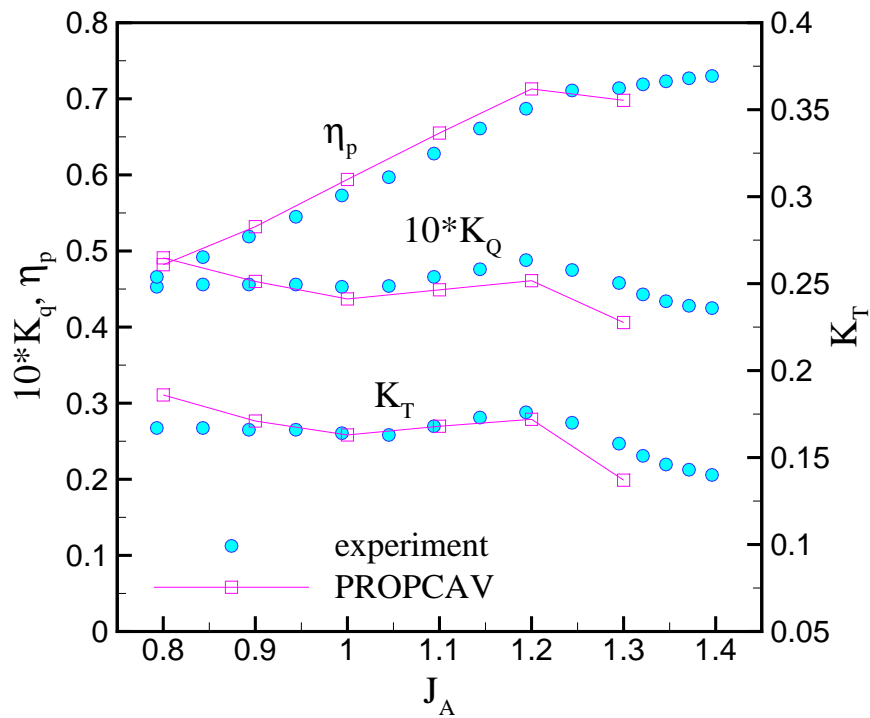


Figure 2.42: Comparison of the predicted and versus measured K_T , K_Q , and η_p for different advance coefficients.

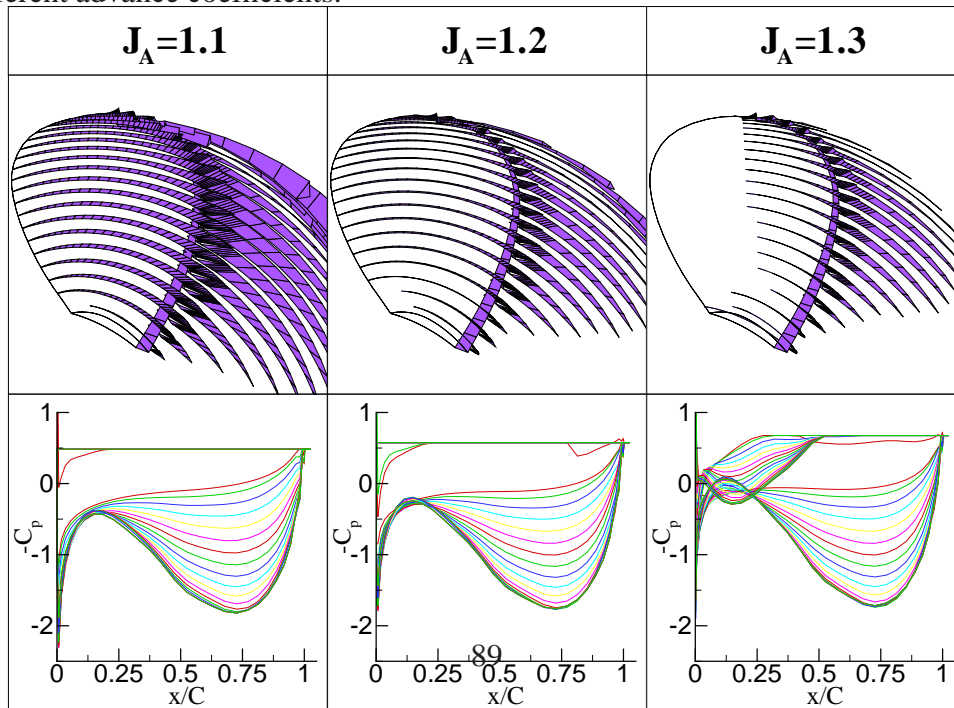


Figure 2.43: Predicted cavity shape and cavitating pressures for propeller SRI at $J_A = 1.3$. 50x20 panels. Uniform inflow.

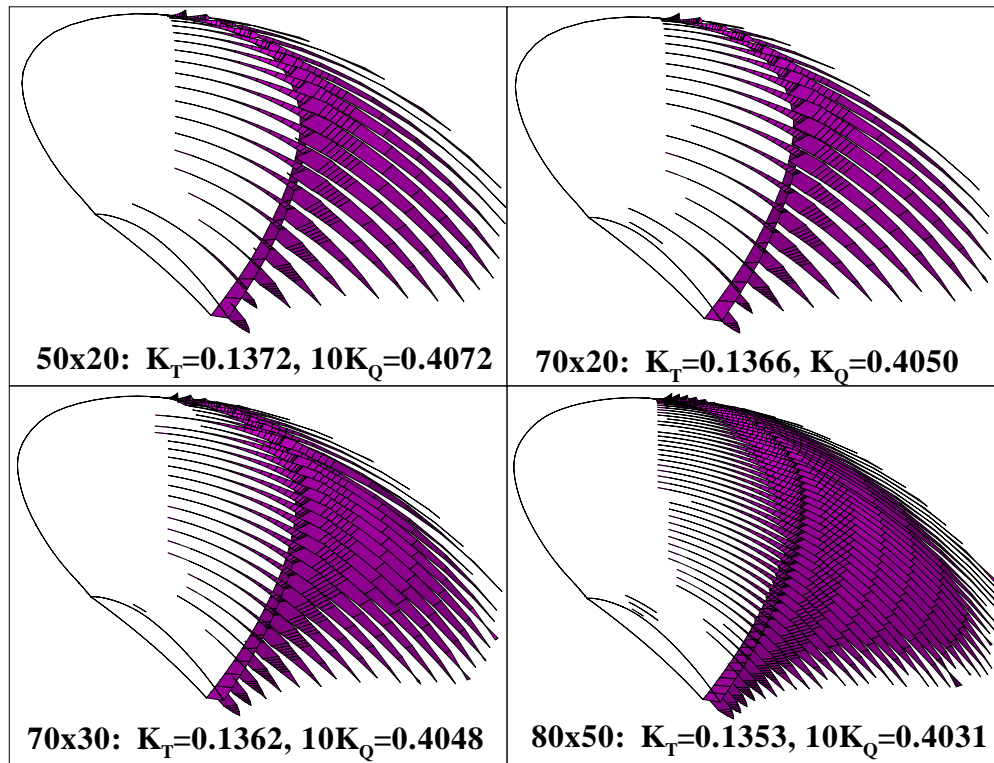


Figure 2.44: Convergence of cavity shape and force coefficients with number of panels for $J_A = 1.3$. Uniform inflow.

2.9 Results

To the authors' knowledge, there are no documented experimental measurements for submerged supercavitating propellers subjected to non-axisymmetric inflows. Thus, only numerical predictions for a sample run with propeller SRI subjected to inclined inflow are shown in this section. The propeller geometry is depicted in Fig. 2.30. The flow conditions are as follows: $\sigma_n=0.784$, $J_s=1.4$, $F_r=5.0$, and 3° inclination. The predicted cavity planforms, pressure distributions, and pressure contours are shown in Figs. 2.45 to 2.47. Convergence studies with respect to number of propeller revolutions, time step size, and grid size are shown in Figs. 2.31, 2.32, and 2.33, respectively. Notice that for the given blade geometry and flow conditions, there is simultaneous face and back cavitation. On the suction side, there is midchord supercavitation that remains relatively constant in shape for all blade angles. On the pressure side, there is leading edge partial cavitation that varies considerably with blade angle. It is also worth noting that the smooth detachment condition is satisfied at all blade angles, and that the predicted cavities seemed reasonable. Moreover, this is the first time a numerical method is able to predict simultaneous face and back cavitation on a (conventional or supercavitating) propeller subject to non-axisymmetric inflow.

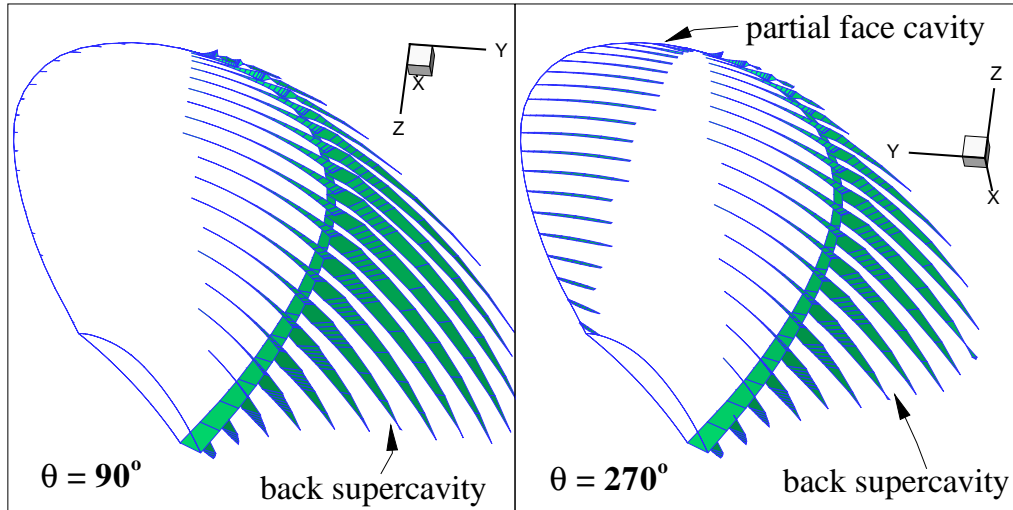


Figure 2.45: Predicted cavity planforms at two different blade angles. Propeller SRI. $\sigma_n=0.784$. $J_s=1.4$. $F_r=5$. 3° inclination. 60×20 panels. $\Delta\theta = 6^\circ$.

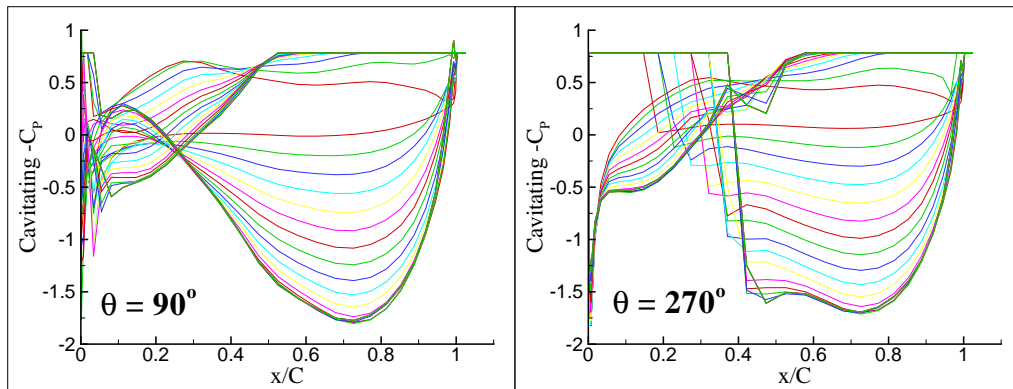


Figure 2.46: Predicted cavity pressure distributions for various radii at two different blade angles. Propeller SRI. $\sigma_n=0.784$. $F_r=5$. $J_s=1.4$. 3° inclination. 60×20 panels. $\Delta\theta = 6^\circ$.

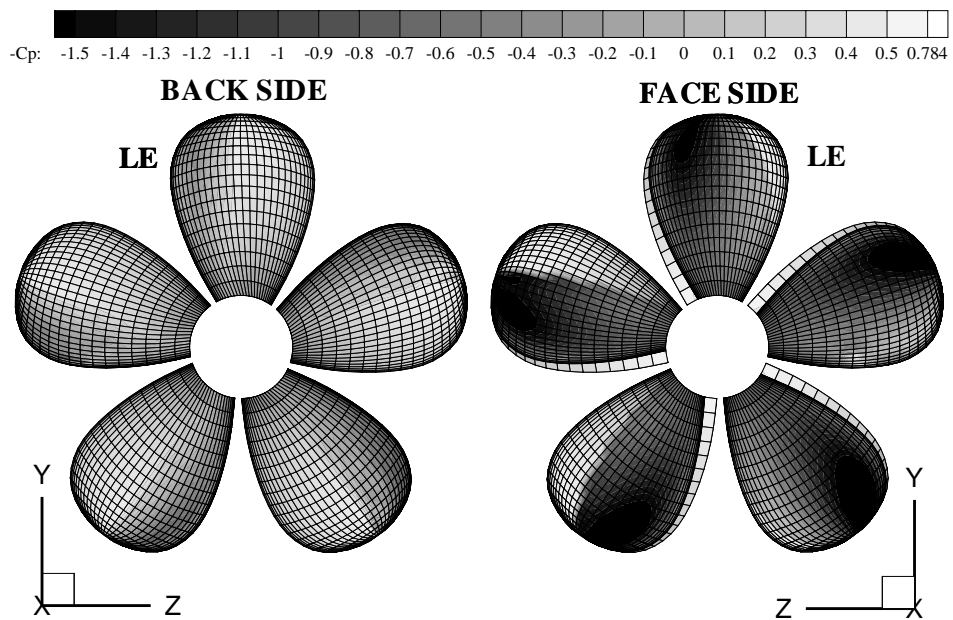


Figure 2.47: Predicted cavity pressure contours. Propeller SRI. $\sigma_n=0.784$. $J_s=1.4$. $F_r=5$. 3° inclination. 60×20 panels. $\Delta\theta = 6^\circ$.

2.10 Summary

A 3-D boundary element method has been extended to predict complex types of cavity patterns on both sides of the blade surface for conventional and supercavitating propellers in steady and unsteady flow. An overview of the formulation, numerical implementation, and treatments for face & back cavitation are presented. For supercavitating propellers with non-zero trailing edge thickness, the current algorithm assumes the pressure to be constant and equal to the vapor pressure on the separated region. Based on this assumption, the method is able to predict the extent and thickness of the separated regions like additional cavitation bubbles.

Numerical validation studies for face and back cavitation, and for sections with non-zero trailing edge thickness, seemed very reasonable. Parametric studies also showed that the method converged quickly with different time and space discretizations.

The current method is able to predict face and/or back cavitation on general propeller geometries in steady or unsteady flow conditions. The required CPU time for a steady (cavitating) run is in the order of minutes, and for an unsteady (cavitating) run is in the order of hours. Examples of required CPU times for two different propellers with various grid discretization are shown in Tables 2.1 and 2.2.

The results from validation tests with experiments showed that in general, the predicted propeller loadings and cavity shapes agree well with experimental observations and measurements. PROPCAV's predictions were also in reasonable agreement with those of MPUF-3A. However, additional studies are needed to de-

termine the effect of prescribed separated region pressure on the predicted blade forces in the case of fully wetted and partially cavitating flow. Under the current algorithm, it is possible to prescribe a different pressure, such as that measured in experiment or computed using a 2-D viscous flow analysis, on the separated region. This feature should be used in the future to determine the relationship between the prescribed separated region pressure and the predicted propeller loadings. A more careful study is also needed to study pressure gradient along the blade trailing edge when one part the blade is wetted or partially cavitating, and another is supercavitating. In addition, in the case of non-axisymmetric inflow, a time-dependent wake alignment model (such as that presented in [Lee 2002]) should be applied to the current method in order to capture the effect of vortex sheet deformation.

Grid	Wetted Analysis	Cavitating Analysis
50x20	0.24 min.	6.20 min.
70x20	0.37 min.	10.57 min.
70x30	0.55 min.	21.13 min.
80x50	1.34 min.	73.18 min.

Table 2.1: Approximate CPU time required on a COMPAQ DS20E with 2-833 MHz Processor (approximately 3-times as fast as an 1-GHz Pentium PC) for propeller SRI subjected to steady inflow. 3 blades. $J_A=1.3$. $\sigma_n=0.676$. $\Delta\theta = 6^\circ$. 8 cavitating revolutions. The comparisons of the cavity shape and cavitating forces for the different grid discretization are shown in Fig. 2.44. Taken from [Young et al. 2001b].

Grid	Wetted Analysis	Cavitating Analysis
50x15, $\Delta\theta = 8^\circ$	1.5 min.	0.5 hr.
50x15, $\Delta\theta = 6^\circ$	2.8 min.	0.8 hr.
50x15, $\Delta\theta = 4^\circ$	4.3 min.	1.5 hr.
60x20, $\Delta\theta = 6^\circ$	4.4 min.	1.5 hr.
70x30, $\Delta\theta = 6^\circ$	11.5 min.	3.1 hr.

Table 2.2: Approximate CPU time required on a COMPAQ DS20E with 2-833 MHz Processor (approximately 3-times as fast as an 1-GHz Pentium PC) for propeller 4148 subjected to unsteady inflow. 3 blades. $J_s=0.954$. $\sigma_n=2.576$. $F_r=9.159$. 5 wetted revolutions and 6 cavitating revolutions. The comparisons of the cavity shape and cavitating forces for the different grid and time discretization are shown in Figs. 2.26 to 2.29. Taken from [Young et al. 2001b].

Chapter 3

Partially Submerged Propellers

3.1 Previous Work

This section presents a brief review of the development of experimental and numerical methods used to determine the performance characteristics of partially submerged propellers.

3.1.1 Experimental Methods

In the past, the design of partially submerged propellers was often based on experience, due to the lack of systematic series data and the lack of reliable theoretical design methods. One of the first known experimental study of partially submerged propellers was presented in [Reynolds 1874], where the effect of immersion on skewed propellers was studied. Since then, many more experimental investigations have been published. Some of the more notable investigation include those by [Shiba 1953; Hadler and Hecker 1968; Hecker 1973; Rains 1981; Rose and Kruppa 1991; Kruppa 1992; Rose et al. 1993; Wang 1995]. The focus of all these studies was to determine the *time averaged* thrust, torque, bending moment, and transverse forces. In particular, the influence of blade tip immersion, number of blades, blade pitch, rake, skew, section geometry, as well as shaft yaw and inclination angles. More recently, [Olofsson 1996; Miller and Szantyr 1998; Dyson

2000; Dyson et al. 2000] also conducted experiments to determine the dynamic performance of partially submerged propellers. The common objective was to study the time dependent hydrodynamic load, and the stresses induced on the propeller blades, shaft, and the hull structure.

However, model tests are extremely expensive, difficult, and time consuming to perform. The test must be carried out in a variable pressure free-surface tunnel that permits high-speed operations. The free surface must be clearly defined [Kruppa 1992]. A multi-component dynamometer is needed to measure primary and secondary forces ¹. Special equipments are also needed to simultaneously provide realistic conditions for cavitation inception while maintaining constant water density [Olofsson 1996]. Furthermore, special considerations are needed to address scale issues so that the performance of the model scale, including blade vibration characteristics, resembles that of the prototype [Olofsson 1996; Dyson 2000]. Thus, the development of reliable, versatile, and robust computational tools to predict propeller performance is crucial to the design and application of partially submerged propellers.

¹Experimental studies indicated that the transverse hydrodynamic forces are high in both directions, which can significantly influence vessel performance and shaft stresses [Rose et al. 1993].

3.1.2 Numerical Methods

•*Lifting Line Methods*

The first effort to model partially submerged propeller was carried out by [Oberembt 1968]. He used a lifting line approach to calculate the characteristics of partially submerged propellers. [Oberembt 1968] assumed that the propeller is lightly loaded such that no natural ventilation of the propeller and its vortex wake occur. However, this is often not the case for partially submerged propellers.

A lifting-line approach which includes the effect of propeller ventilation was developed by Furuya in [Furuya 1984, 1985]. He used linearized boundary conditions and applied the image method to account for free surface effects. He also assumed the face portion of the blades to be fully wetted and the back portion of the blades to be fully ventilated starting from the blade leading edge. The blades were reduced to a series of lifting lines, and method was combined with a 2-D water entry-and-exit theory developed by [Wang 1977, 1979] to determine thrust and torque coefficients. Furuya compared the predicted mean thrust and torque coefficients with experimental measurements obtained by [Hadler and Hecker 1968]. In general, the predicted thrust coefficients were within acceptable range compared to measured values. However, there were significant discrepancies with torque coefficients. Furuya attributed the discrepancies to the effects of nonlinearity, absence of the blade and cavity thickness representation in the induced velocity calculation, and uncertainties in interpreting the experimental data. He also stated that the application of lifting-line theory is limited due to the relative large induced velocities at low advance coefficients.

•*Lifting Surface Methods*

An unsteady lifting surface method was employed by [Wang et al. 1990b] for the analysis of 3-D fully ventilated thin foils entering into initially calm water. The method was later extended by [Wang et al. 1990a] and [Wang et al. 1992] to predict the performance of fully ventilated partially submerged propellers with its shaft above the water surface. Similar to [Furuya 1984, 1985], the method assumed the flow to separate from both the leading edge and trailing edge of the blade, forming on the suction side a cavity that vents to the atmosphere. Discrete line vortices and sources were placed on the face portion of the blade to simulate the effect of blade loading and cavity thickness, respectively. Line sources were also placed on the cavity surface behind the trailing edge of the blade to represent the cavity thickness in the wake. A helical surface with constant radius and pitch were used to construct the trailing vortex sheets. The negative image method was used to account for the effect of the free surface. The effect of the blade thickness was neglected in the computation. Comparisons were presented with both experimental measurements by [Hadler and Hecker 1968] and numerical predictions by [Furuya 1984, 1985]. The predictions were within reasonable agreement with experimental values for propeller MAU4-60 for a limited data range. However, substantial discrepancies were observed for propeller 4002 with both experimental values and numerical predictions by [Furuya 1984, 1985].

The 3-D lifting surface VLM developed by [Kudo and Ukon 1994] and [Kudo and Kinnas 1995] for the analysis of supercavitating propellers (described in Section 2.1.4) has also been extended for the analysis of surface-piercing pro-

pellers. However, the VLM performs all the calculations assuming the propeller is fully submerged, then multiplies the resulting forces with the propeller submergence ratio. As a result, only the mean forces can be predicted while the complicated phenomena of blade's entry to, and exit from, the water surface are completely ignored.

•*Boundary Element Methods*

A 2-D time-marching BEM was developed by [Savineau and Kinnas 1995] for the analysis of the flow field around a fully ventilated partially submerged hydrofoil. However, this method only accounts for the hydrofoil's entry to, but not exit from, the water surface. In addition, the negative image method was used so the effects of water jets and change in free surface elevation were ignored.

3.2 Objectives

For partially submerged propellers, the primary objective is to extend PROPCAV to predict the performance of partially submerged propellers subject to time dependent inflow. The second objective is to quantify the added hydrodynamic forces due to the formation of high speed jets at the moment of blade entry.

3.3 Formulation

In this chapter, the 3-D potential based BEM (PROPCAV) for the analysis fully submerged propellers is extended to predict the performance of partially submerged propellers. The formulation and numerical implementation that are dif-

ferent from that of fully submerged propellers are presented in this section.

3.3.1 Fundamental Assumptions

For the 3-D hydrodynamic modeling of partially submerged propellers, the following assumptions are made in addition to those explained in Section 2.3.1:

- The influence of free surface jets are assumed negligible (i.e. the free surface can be treated as a flat surface)².
- The Froude number is assumed to grow without bounds³.
- The wake is assumed to be a helical surface with constant pitch and radius.
- The cavities are assumed to be fully ventilated, i.e. the pressure on the cavity is constant and equal to the atmospheric pressure. The ventilated cavity detachment locations are searched for on the suction (back) side of the blade.
- The influence of the shed and trailing vorticity in the wake once the blade has left the free surface is assumed negligible.

Despite all these drastic simplifications, the problem remains difficult to solve due to the unknown and time-dependent geometry of ventilated cavities. The

²Based on experimental observations, very high jets develop at the blade entry and exit phase, which tend to increase the hydrodynamics forces. Thus, a detailed 2-D study (see Chapter 4) using the exact free surface boundary conditions, is initiated to study the effect of jet sprays.

³Although the effect of gravity plays an important role in surface wave generation, experimental studies by [Shiba 1953; Brandt 1973; Olofsson 1996] shown that the effect of Froude number is negligible for $F_{nd} = \frac{V}{\sqrt{gD}} > 4$ or $F_r = \frac{n^2 D}{g} > 2$ in the fully ventilated regime.

problem is further complicated by the interruption of the ventilated wake by the free surface. The characteristic thick blade trailing edge also increases the level of difficulty in analyzing the flow. The objective of this work is to provide a numerical tool that can predict, to some extent, the unsteady hydrodynamic response of partially submerged propellers.

3.3.2 Green's Formula

Since the propeller is partially submerged, the computational boundary must also include the free surface. Hence, the perturbation potential, ϕ_p , at every point p on the combined wetted blade surface $S_{WB}(t)$, ventilated cavity surface $S_{C1}(t) \cup S_{C2}(t) \cup S_{C3}(t)$, and free surface $S_F(t)$, must satisfy Green's third identity:

$$2\pi\phi_p(t) = \int \int_{S(t)} \left[\phi_q(t) \frac{\partial G(p; q)}{\partial n_q(t)} - G(p; q) \frac{\partial \phi_q(t)}{\partial n_q(t)} \right] dS \quad (3.1)$$

where $S(t) \equiv S_{WB}(t) \cup S_{C1}(t) \cup S_{C2}(t) \cup S_{C3}(t) \cup S_F(t)$ is the combined surfaced as defined in the blade section example shown on Fig. 3.1. \vec{n}_q is the unit vector normal to the integration surface, with the positive direction pointing into the fluid domain.

As in the case of fully submerged propellers, the "exact" ventilated cavity surfaces, $S_{C1}(t) \cup S_{C2}(t) \cup S_{C3}(t)$, are unknown and have to be determined as part of the solution. Thus, the ventilated cavity surfaces are approximated with the blade surface underneath the cavity, $S_{C2}(t) \rightarrow S_{CB}(t)$, and the portion of the wake surface which is overlapped by the cavity, $S_{C1}(t) \cup S_{C3}(t) \rightarrow S_{CW}(t)$. The definition of $S_{CB}(t)$ and $S_{CW}(t)$ are shown in Fig. 3.1.

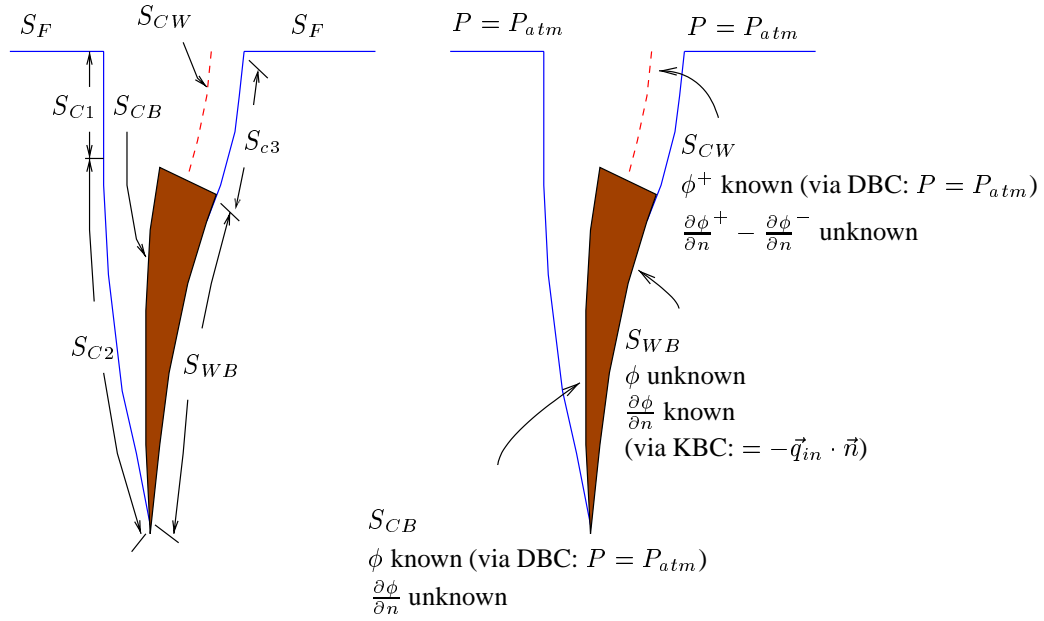


Figure 3.1: Definition of “exact” and approximated flow boundaries around a surface-piercing blade section .

3.3.3 Boundary Conditions

The boundary conditions are similar to those presented in Section 2.3.4 with the following modifications and additions:

- *Dynamic Boundary Condition on the Free Surface and Ventilated Cavity Surfaces*

The dynamic boundary condition requires that the pressure everywhere on the free surface and on the ventilated cavity surface to be constant and equal to the atmospheric pressure, P_{atm} . Redefining $\sigma_n \equiv (P_o - P_{atm})/(\frac{\rho}{2}n^2D^2)$ as the ventilated cavitation number, the dynamic boundary condition reduces to Eqns 2.15 and 2.16 on the on $S_{CB}(t)$ and $S_{CW}(t)$, respectively.

- *Kinematic Boundary Condition on the Ventilated Cavity Surfaces*

The kinematic boundary condition on the ventilated cavity surfaces renders the same expression as Eqns. 2.18 and 2.19 on $S_{CB}(t)$ and $S_{CW}(t)$, respectively. However, for partially submerged propellers, the cross-flow velocities are also assumed to be small on the blade surface (i.e. $V_v \approx V_s \cos \psi$ on $S_{CB}(t)$). This reduces the $\frac{\partial h}{\partial v}$ term in Eqn. 2.18 to zero, as depicted in Fig. 3.2. The justification of this assumption can be found in [Fine 1992], where it is shown that the cross-flow term (evaluated iteratively) on the blade has a very small effect on the predicted supercavity on either a 3-D hydrofoil or a propeller blade. In addition, the $\frac{\partial h}{\partial v}$ term is difficult to evaluate due to the interruption of the ventilated cavity by the free surface.

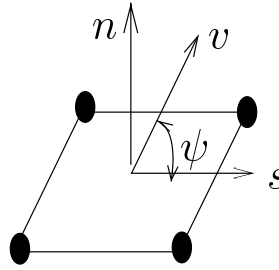
KBC on cavitating surface

$$\begin{aligned} \frac{\partial h}{\partial s} [V_s - \cos \psi V_v] + \frac{\partial h}{\partial v} [V_v - \cos \psi V_s] \\ = \sin^2 \psi \left(V_n - \frac{\partial h}{\partial t} \right) \end{aligned}$$

$$V_n \equiv \frac{\partial \phi}{\partial n} + \vec{q}_{in} \cdot \vec{n}$$

$$V_v \equiv \frac{\partial \phi}{\partial v} + \vec{q}_{in} \cdot \vec{v}$$

$$V_s \equiv \frac{\partial \phi}{\partial s} + \vec{q}_{in} \cdot \vec{s}$$



Assume crossflow velocity is small

$$\Rightarrow V_v = \cos \psi V_s$$

$$\Rightarrow \frac{\partial h}{\partial v} [V_v - \cos \psi V_s] = 0$$

Figure 3.2: Reduction of the cross-flow term in the kinematic boundary condition on the ventilated blade cavity surface, $S_{CB}(t)$.

• *Linearized Free Surface Boundary Condition on the Free Surface*

As a first step to model partially submerged propellers in 3-D, the linearized free surface boundary condition is applied:

$$\frac{\partial^2 \phi}{\partial t^2}(x, y, z, t) + g \frac{\partial \phi}{\partial y_s}(x, y, z, t) = 0 \quad \text{at } y_s = -R + h \quad (\text{i.e. free surface}) \quad (3.2)$$

where h and R are the blade tip immersion and blade radius, respectively, as defined in Fig. 3.3. y_s is the vertical ship-fixed coordinate, defined in Fig. 2.1.

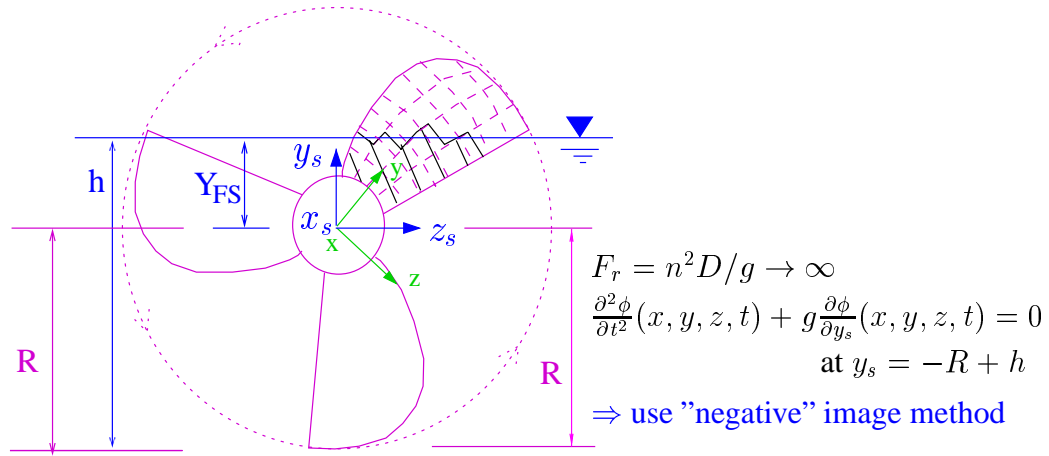


Figure 3.3: Linearized free surface boundary condition and the infinite Froude number assumption.

Assuming that the infinite Froude number condition (i.e. $F_r = n^2 D / g \rightarrow \infty$) applies, Eqn. 3.2 reduces to:

$$\phi(x, y, z, t) = 0 \quad \text{at } y_s = -R + h \quad (3.3)$$

Equation 3.3 implies that the negative image method⁴ can be used to account for

⁴Details of the negative image method are presented in Section 3.4.1.

the effect of the free surface. The assumption that the Froude number grows without bounds is valid because partially submerged propellers usually operate at very high speeds. Studies by [Shiba 1953; Brandt 1973; Olofsson 1996] have also shown that the effect of Froude number is negligible for $F_{nd} = \frac{V}{\sqrt{gD}} > 4$ or $F_r = \frac{n^2 D}{g} > 2$ in the fully ventilated regime.

3.4 Numerical Implementation

In this section, the numerical implementation for partially submerged propellers that differs from fully submerged propellers is presented.

3.4.1 Negative Image Method

For the 3-D analysis of partially submerged propellers, the negative imaged method is used to account for free surface effects. The method is based on the linearized free surface boundary condition and the infinite Froude number assumption. Consequently, only vertical motions are allowed on the free surface. This is accomplished by distributing sources and dipoles of equal strengths but with negative signs on the location of the mirror image with respect to the free surface. A schematic example of the negative image method on a blade section is shown in Fig. 3.4.

In the current method, the image influence coefficients are lumped with the real influence coefficients for each submerged panel. Thus, the discretized form of

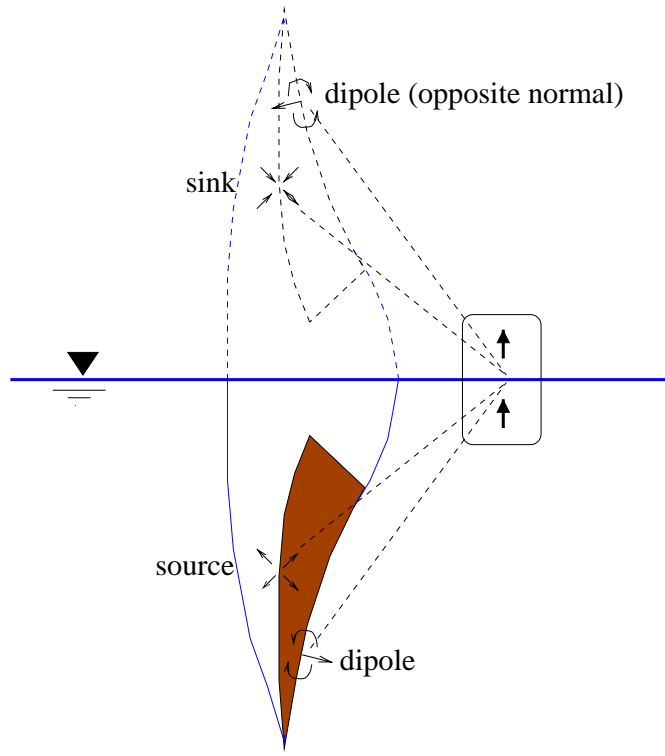


Figure 3.4: Schematic example of the negative image method on a partially submerged blade section.

Eqn. 3.1 can be written as:

$$\begin{aligned}
 2\pi\phi_i &= \sum_{k=1}^{NK} \sum_{m=1}^M \left\{ \sum_{n=1}^{NB_s(m,k,t)} \left[A_{i,m,n,k}(t)\phi_{m,n,k}(t) - B_{i,m,n,k}(t)\frac{\partial\phi}{\partial n_{m,n,k}}(t) \right] \right. \\
 &\quad \left. - \sum_{n=1}^{NCW_s(m,k,t)} C_{i,m,n,k}(t)Q_{m,n,k}(t) + \sum_{n=1}^{NW_s(m,k,t)} W_{i,m,n,k}(t)\Delta\phi_{m,n,k}(t) \right\} \\
 &\text{for } i = 1, \dots, M \times \{NB_s(m, k, t) + NCW_s(m, k, t)\} \quad (3.4)
 \end{aligned}$$

where

$$\begin{aligned}
A_{i,m,n,k}(t) &= A_{i,m,n,k}^s - A_{i,m,n,k}^i(t) \\
B_{i,m,n,k}(t) &= B_{i,m,n,k}^s - B_{i,m,n,k}^i(t) \\
C_{i,m,n,k}(t) &= C_{i,m,n,k}^s - C_{i,m,n,k}^i(t) \\
W_{i,m,n,k}(t) &= W_{i,m,n,k}^s - W_{i,m,n,k}^i(t)
\end{aligned} \tag{3.5}$$

The superscript “*s*” and “*i*” in Eqn. 3.5 denote the submerged panel and its image, respectively. $A_{i,m,n,k}$ represent the potential induced at the i^{th} submerged control point on the key blade by unit strength dipoles at the real and imaged n^{th} panel on the m^{th} strip of the k^{th} blade. Note that $k = 1$ refers to the key blade. Similarly, $B_{i,m,n,k}$, $C_{i,m,n,k}$, and $W_{i,m,n,k}$ represent the sum of the real and image influence coefficients due to unit strength source on the blade, unit strength source on the cavitating wake, and unit strength dipole on the wake, respectively. $Q_{m,n,k}$ represents the cavity source strength defined by Eqn. 2.6 on the n^{th} panel of the m^{th} strip of the k^{th} blade.

Note that the sign in front of the image coefficients in Eqn. 3.5 are negative due to the equal and opposite strengths of the image singularities compared to the real singularities. In addition, since the problem is solved with respect to the propeller fixed coordinates which rotates with the key blade, the location of the n^{th} image on the m^{th} strip of the k^{th} blade changes with time t . The quantities NB_s , NCW_s , and NW_s represent the number of submerged panels on the blade, cavitating wake, and wake, respectively, on the m^{th} strip of the k^{th} blade. The quantity

NK in Eqn. 3.4 represents the total number blades, while M represents the total number of radial strips per blade.

3.4.2 Solution Algorithm

As shown in Eqn. 3.4, Green's formula is only solved for the total number of submerged panels on the key blade and the cavitating portion of the key wake. The influence of the other blades is accounted for in a progressive manner by using the solution from an earlier time step when the key blade was in the position of that blade. The values of the ϕ and $\frac{\partial\phi}{\partial n}$ are set equal to zero on the blade and wake panels that are above the free surface. Note that the current algorithm does not re-panel the blades and wakes at every time step, in order to maintain computation efficiency. As a result, there are some panels that are partially cut by the free surface. In the present algorithm, the strengths of the singularities are also set equal to zero for the partially submerged panels. Nevertheless, a method similar to the split-panel technique, described in Section 2.4.2, can be applied to account for the effects of these panels.

The solution algorithm for partially submerged propellers is similar to that explained in Sections 2.4.1 and 2.6 for fully submerged supercavitating propellers. However, iterations to determine the correct cavity lengths are no longer necessary since the ventilated cavities are assumed to vent to the atmosphere, as observed in experiments.

3.4.3 Ventilated Cavity Detachment Search Criterion

Depending on the flow conditions and the blade section geometry, the ventilated cavities may detach aft of the blade leading edge. The cavity detachment locations on the suction side of the blade are searched for in an iterative manner at each time step until the smooth detachment condition (presented in Section 2.4.3) is satisfied. In addition, due to the interruption of the free surface, the following detachment conditions must also be satisfied for partially submerged propellers:

- The ventilated cavities must detach at or prior to the blade trailing edge; and
- During the exit phase (i.e. when part of the blade is departing the free surface), the ventilated cavities must detach at or aft of the intersection between the blade section and the free surface.

A schematic diagram showing different cavity detachment locations for a surface-piercing blade section is depicted in Fig. 3.5. It should be noted that the ventilated cavities on the pressure side of the blade are always assumed to detach from the blade trailing edge. It is possible to also search for cavity detachment locations on the pressure side. However, such occurrence is unlikely due to the high-speed operation of partially submerged propellers.

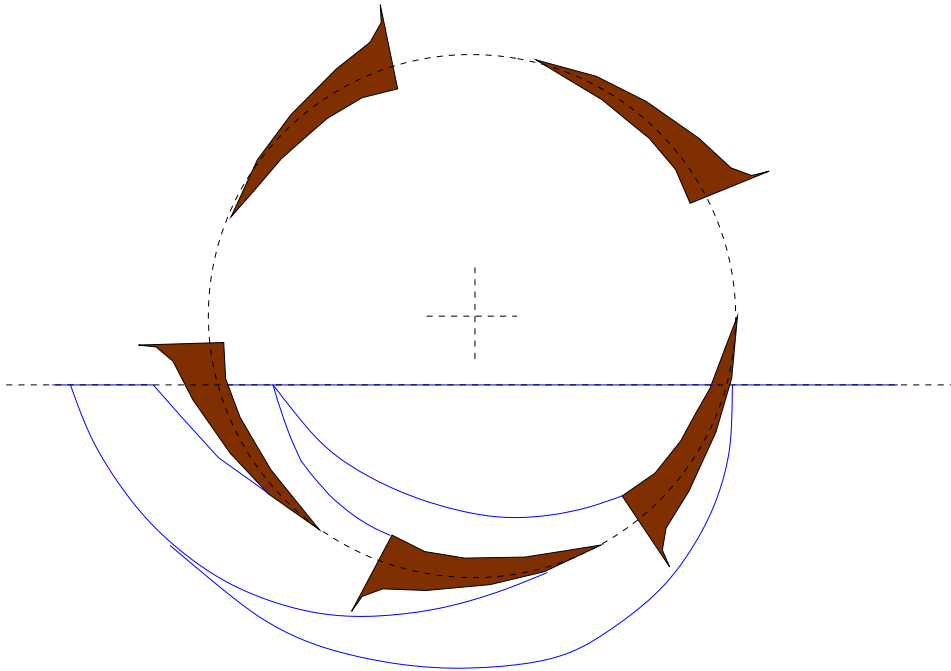


Figure 3.5: Graphic illustration of ventilated cavity patterns that satisfy the cavity detachment condition on a partially submerged blade section. In addition, the cavities are assumed to vent to the atmosphere.

3.5 Convergence Studies

In order to validate the performance prediction of the method, convergence studies with varying number of propeller revolutions, panel discretization, and time step size are presented in this section. All the convergence studies shown in this section are for propeller model 841-B with $J_s = 1.2$. The propeller geometry, test conditions, and comparisons of predictions with experimental measurements are presented in Section 3.6.

3.5.1 Convergence with Number of Revolutions

As explained in Section 3.4, the influence of the other blades on the key blade are accounted for in a progressive manner. In addition, iterations are needed to determine the correct ventilated cavity detachment locations. Thus, the solution depends on the number of propeller revolutions. The convergence of individual blade forces with number of revolution for propeller model 841-B is shown in Fig. 3.6. It should be noted that the unsteady term ($\frac{\partial \phi}{\partial t}$) is not activated until two revolutions are completed for the case of partially submerged propellers to avoid stability problems. As shown in Fig. 3.6, the results converged very quickly with number of revolutions.

3.5.2 Convergence with Time Step Size

Partially submerged propellers flows are inherently unsteady due to the loading and unloading of the blades associated with the blades' entry to, and exit from, the free surface. Thus, the solution also depends on the time step size, which

is expressed in terms of blade angle increment. In Fig. 3.7, the convergence of the individual blade forces $\Delta\theta = 3^\circ, 6^\circ, \&9^\circ$ are presented. Notice that the result also converged quickly with time step size.

3.5.3 Convergence with Grid Size

In addition to the number of propeller revolutions and blade angle increments, the solution also depends on the panel discretization. Figure 3.8 depicts the influence of panel discretization on the individual blade forces, which also converged quickly with number of panels.

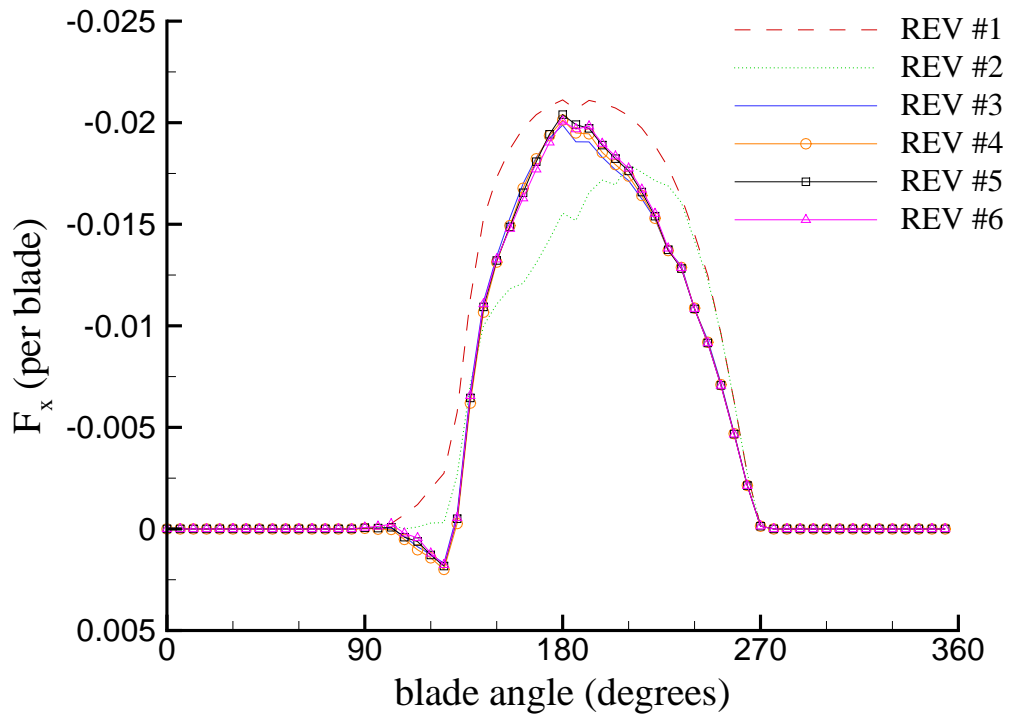


Figure 3.6: Convergence of thrust (K_T) and torque (K_Q) coefficients (per blade) with number of revolutions. Propeller model 841-B. $J_A = 1.2$. 70x30 panels. $\Delta\theta = 6^\circ$.

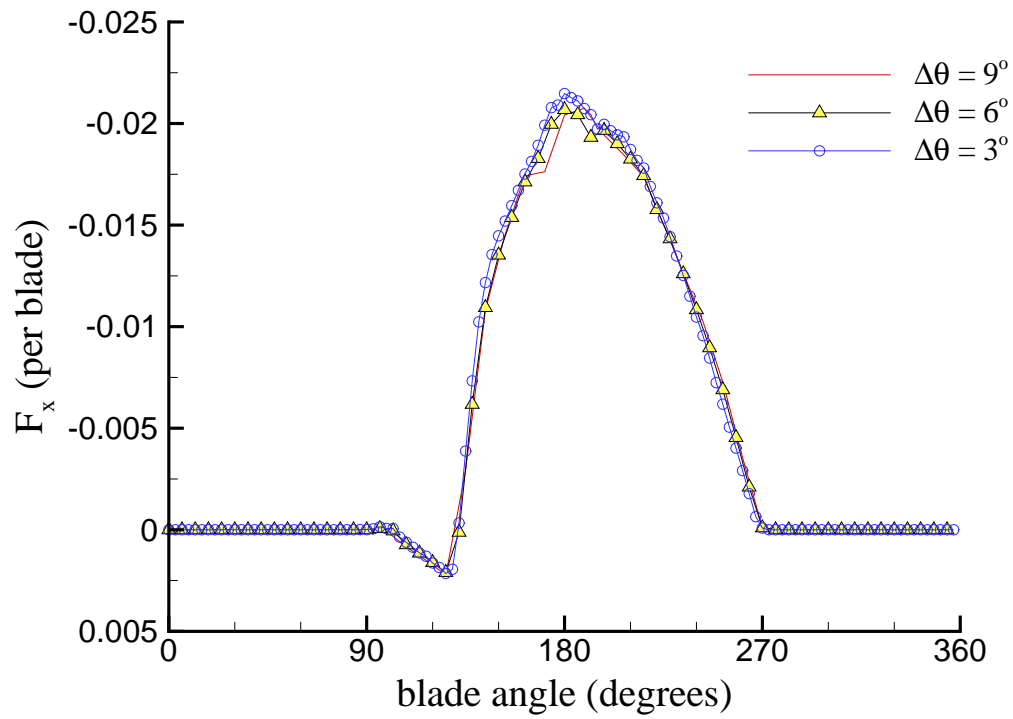


Figure 3.7: Convergence of thrust (K_T) and torque (K_Q) coefficients (per blade) with time step size. Propeller model 841-B. $J_A = 1.2$. 70x30 panels. 6 propeller revolutions.

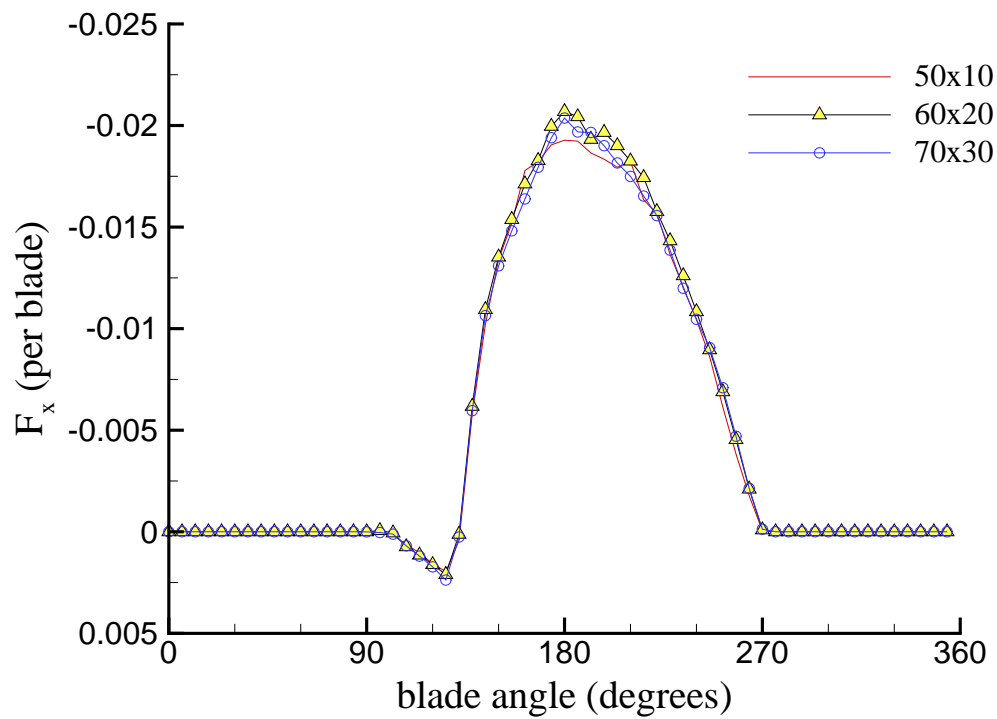


Figure 3.8: Convergence of thrust (K_T) and torque (K_Q) coefficients (per blade) with panel discretization. Propeller model 841-B. $J_A = 1.2$. $\Delta\theta = 6^\circ$. 6 propeller revolutions.

3.6 Validation with Experiments

In order to validate the partially submerged propeller formulation of the method, numerical predictions for propeller model 841-B are compared with experimental measurements collected by [Olofsson 1996]. A photograph of the partially submerged propeller and the corresponding BEM model are shown in Fig. 3.9. The experiments were conducted at the free-surface cavitation tunnel at KaMeWa of Sweden. Details of the experiments are given in [Olofsson 1996], and are summarized in the next subsection for the sake of completeness.

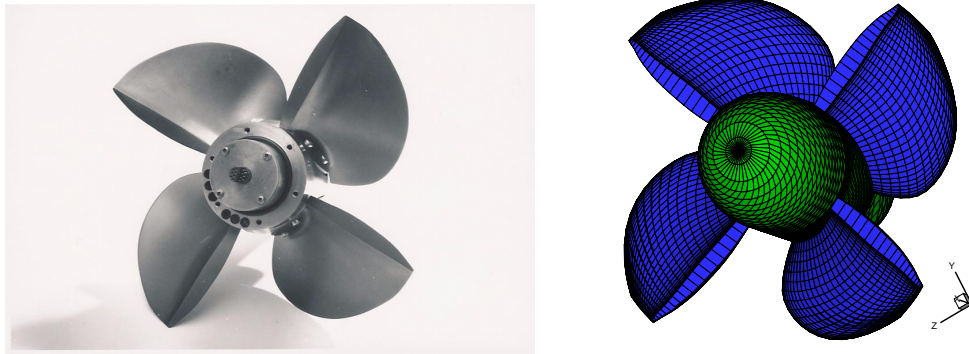


Figure 3.9: Photograph of propeller model 841-B shown in [Olofsson 1996], with corresponding BEM model on the right.

3.6.1 Summary of Experiment by Olofsson

In [Olofsson 1996], Olofsson conducted a very thorough series of experiments to determine the time-averaged and dynamic performance of propeller model 841-B. The four-bladed high-speed partially submerged propeller was designed based on sea trials on a board a 13 m twin screw planing test craft. The diame-

ter of the full-scale propeller is 250 mm. The experiments were conducted at the KaMeWa free surface cavitation tunnel in Sweden. The tunnel was selected for its high speed and flow observation capabilities. The test section length, width, and height are 4 m, 0.8 m, and 1.5 m, respectively. The water is filled to a height of 0.8 m to ensure small wall effects under fully cavitating or ventilated conditions. The data and outline of the tunnel is shown in Fig. 3.10. The tunnel was equipped with a large de-aerating chamber downstream of the test section. The de-aerating chamber was used to eliminate the occurrence of air-liquid mixture in the test section when testing to maintain constant water density. The tunnel has also been equipped with a special device for micro air bubble seeding to provide constant cavitation inception as well as realistic propeller thrust and torque without hysteresis in partially cavitating conditions. The blade dynamometer was an existing 4-bladed, single flexure, 5-component dynamometer developed KaMeWa. The flexure-unit, shown in Fig. 3.11, was specially designed to capture the true effect of *blade* vibration.

In the experiment, Olofsson selected combinations of Froude number and cavitation number that simultaneously satisfied cavitation number and Froude number scaling. In other words, the model scale is required to have the same same cavitation number and Froude number as the full scale. The cavitation and Froude number were defined as follows in [Olofsson 1996]:

$$\sigma_v = \frac{P_o - P_v}{0.5\rho V_A^2} \quad \text{and} \quad F_{nD} = \frac{V_A}{\sqrt{gD}} \quad (3.6)$$

where the static pressure (P_o) on the water surface in the test section was given in

[Olofsson 1996] as follows:

$$P_o = P_v + (P_{atm} - P_v) \cdot \frac{1}{\lambda} \quad (3.7)$$

Thus, the cavitation number can be re-written as:

$$\sigma_v = \frac{P_{atm} - P_v}{0.5\rho g D} \cdot \frac{1}{\lambda} \cdot \frac{1}{F_{nD}^2} \quad (3.8)$$

The symbol λ in Eqn. 3.8 is the scale ratio, i.e. the ratio of full-scale diameter and model scale diameter D . In the experiment, three scale models were examined: $\lambda = 1, 3,$ and 9 . The Froude numbers (F_{nD}), scale ratios (λ), and corresponding cavitation numbers ($\sigma = \sigma_v$) that was tested are shown in Fig. 3.12. Also shown in Fig. 3.12 are the critical Reynolds number (R_n), Weber number (W_n), and Froude number for model 841-B.

In [Olofsson 1996], only one blade immersion ratio ($h/D = 0.33$) was considered, and the influence of Froude and cavitation number at different advance speeds was systematically examined. Tests with different shaft yaw and inclination angles were also performed.

3.6.2 Test Conditions Selected for Comparisons

The following combination of test conditions were selected so that the influence of Froude number, cavitation number, Webber number, and blade vibration are minimized:

$$\begin{aligned}
\text{shaft yaw angle} & : \beta = 0^\circ \\
\text{shaft inclination angle} & : \gamma = 0^\circ \\
\text{blade tip immersion} & : h/D = 0.33 \\
\text{advance coefficient} & : J_A = V_A/nD = 0.8 - 1.2 \\
\text{Froude number} & : F_{nD} = V_A/\sqrt{gD} = 6.0 \\
\text{cavitation number} & : \sigma_v = (P_o - P_v)/(0.5\rho V_A^2) = 0.25
\end{aligned}$$

At these flow conditions, the cavities are fully ventilated and the effect of Froude number is negligible [Olofsson 1996]. The velocity distribution at the propeller plane is shown in Fig. 3.13. The axial velocity is zero at the free surface because a flat plate was placed in front of the propeller to provide a well defined free surface.

3.6.3 Comparison of Numerical Predictions with Experimental Measurements

To validate the performance prediction of the method, the predicted force coefficients are compared with experimental measurements collected by Olofsson [Olofsson 1996] for $J_A = 0.8, 1.0, \& 1.2$. Also presented are the comparison of predicted and observed ventilation patterns.

In the numerical evaluation, the separated region model explained in Section 2.6 is used to treat the non-zero trailing edge thickness. The blade section geometry of propeller model 841-B is shown in Fig. 3.14.

- *Comparisons for $J_A = 0.8$*

The first set of comparisons is for $J_A = 0.8$. The predicted pressure contours on the face side of the blade are shown in Fig. 3.15. The predicted ventilated cavity patterns at different time steps are drawn in Fig. 3.16. It should be noted that this propeller was designed such that the blade enters the water at approximately 90° exits at 270° .

The predicted individual force and moment coefficients are shown in Fig. 3.17 along with experimental data from [Olofsson 1996]. The solid lines and the symbols in Fig. 3.17 represent the load coefficients predicted by the present method and measured in experiments, respectively. (K_{FX} , K_{FY} , K_{FZ} , K_{MX} , K_{MY} , K_{MZ}) are the six components of the individual blade force and moment coefficients defined in the coordinate system shown in Fig. 2.1. It should be noted that the vertical force coefficients (K_{FY}) were not measured in the experiment because a five-component dynamometer was used. Thus, K_{FY} is not shown in Fig. 3.17.

As shown in Fig. 3.17, the maximum force coefficients predicted by the current method seem to be in reasonable agreement with experimental measurements. However, there are significant discrepancies at the blade entry and exit phase. Note that the experimental data in Fig. 3.17 indicated that the blade carries load from approximately 70° to 290° , which is different from the 90° to 270° range in the design. This implies that the overall free surface elevation has increased, and very high jets were developed at the moment of blade entry, both of which were observed by [Olofsson 1996]. Also of importance are the “humps” (amplified fluctuations superimposed on the basic load) observed in the experimental measurements shown in Fig. 3.17. Olofsson [Olofsson 1996] stated that these “humps” are due to blade

vibration and the frequency of these fluctuations modulate between the blade's fundamental frequency in air and in water.

- *Comparisons for $J_A = 1.0$*

The second set of comparisons is for $J_A = 1.0$. In the experiment, V_A was kept constant at 12 m/s. Thus, a higher J_A implies lower propeller rotational frequency. The predicted ventilated surface sections are shown in Fig. 3.18. It is worth mentioning that the ventilated cavities detach primarily from the propeller leading edge for this case, and the thickness of the ventilated cavities are non-negative everywhere.

The predicted individual blade force and moment coefficients for $J_A = 1.0$ are shown in Fig. 3.19 along with experimental data from [Olofsson 1996]. Note that there are less fluctuations in the experimental data compared to $J_A = 0.8$ as a result of the slower rotational speed. In addition, there are less discrepancies between the predicted and measured values.

- *Comparisons for $J_A = 1.2$*

The last set of comparisons is for $J_A = 1.2$. Comparisons of the predicted and observed ventilated cavitation patterns at three different blade angles are shown in Figs. 3.20 to 3.22. Notice the good agreement between the predicted and observed detachment locations and ventilation patterns for all three cases.

The predicted and measured individual blade force and moment coefficients for $J_A = 1.2$ are shown in Fig. 3.23. Notice that there are much less amplified fluctuations due to the slower propeller rotation speed. In addition, the predicted force

coefficients by the present method agree well with experimental measurements.

3.6.4 Discussion of Results

In general, the predicted ventilation patterns and blade forces agree well with experiments. However, there are some discrepancies between the predicted and measured individual blade forces, particularly at low J_A or high rotational speeds. The discrepancies may be attributed to:

- Inadequate simulation of the blade entry phenomena. At the instant of impact, a very strong jet is developed near the blade leading edge, which results into very high slamming forces. In the current formulation, the presence of the jet cannot be captured due to the application of the negative image method. In other words, a nonlinear free surface model should be applied to capture the development of the jet, so that the added hydrodynamic force can be directly evaluated.
- Inability of the current method to capture the increase in free surface elevation. The overall free surface rises due to the cavity displacement effect [Olofsson 1996]. As a result, the actual immersion of the propeller increases, which in turn adds to the hydrodynamic blade load. This effect is most evident in Fig. 3.17. Due to the particular design of the propeller, the actual in-water phase should range from 90° to 270° [Olofsson 1996]. However, the experimental data in Fig. 3.17 show that the blade carries load from 70° to 290° . This is a clear indication that the added forces are due increase in

overall free surface elevation.

- Inability of the current method to model the effect of blade vibrations. Blade vibration is a resonance phenomenon which affects the blade shapes and loadings. It occurs when the frequency content of the hydrodynamic blade loads has a significant energy content at the blade's natural frequencies of vibration. As a result, the blade no longer behaves like a rigid body, and vibrations/displacement are amplified. Blade vibration can significantly contribute to the inertial load, as well as the gravitational load due to the change in the blade's mass center relative to the hub [Olofsson 1996]. The effect of blade vibration is evident via the "humps" (amplified fluctuations superimposed on the basic load) observed in the experimental data shown in Figs. 3.17 to 3.23. It was also observed during the experiments that the frequencies of these fluctuations modulate between the blade's fundamental frequency in air and in water [Olofsson 1996]. However, the current model assumes rigid body motion. Thus, the effects of blade vibrations cannot be captured.

Tunnel Data

Total length	m	25
Height between centre lines	m	12
Water content	m ³	394
Length of test section	m	4.0
Width/height of test section	m	0.8/1.5 ^{*)}
Max. water velocity	m/s	12
Max. diameter of propeller	m	0.3
Min. static pressure	kPa	5
Impeller pump power	kW	1000

*) Water-filled height 0.8 m.

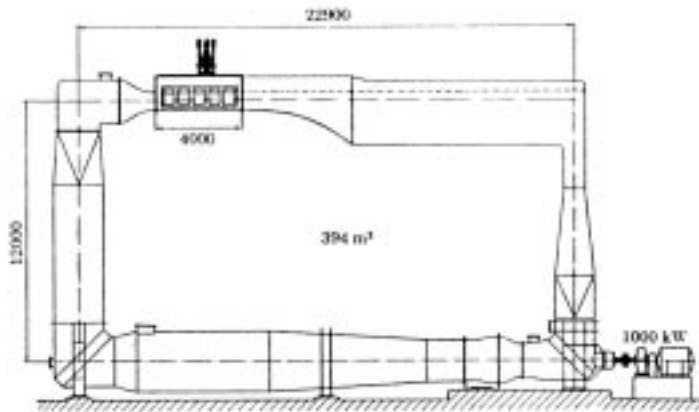


Figure 3.10: The data and outline of the KaMeWa free surface cavitation tunnel. Taken from [Olofsson 1996].

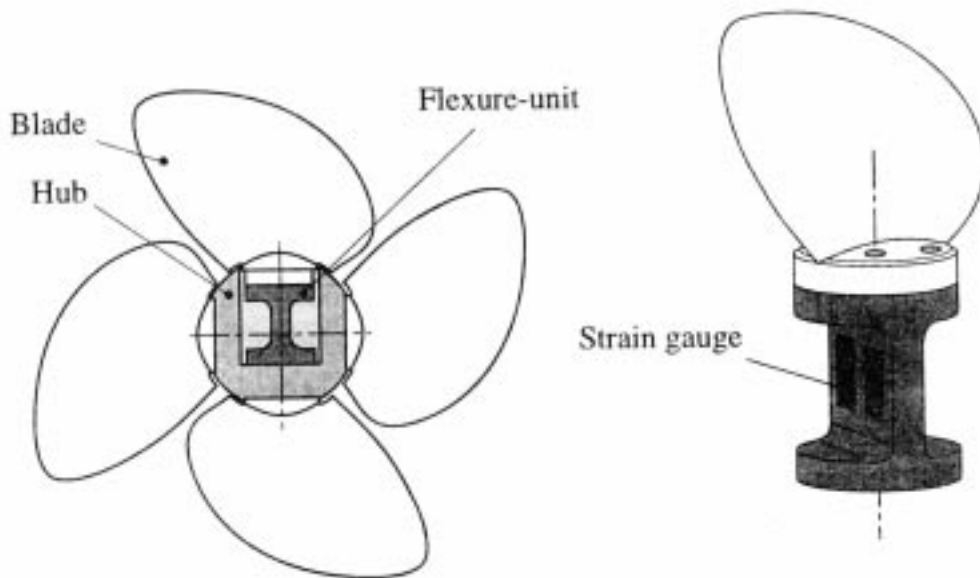


Figure 3.11: The flexure-unit used to measure the reaction load. Taken from [Olofsson 1996].

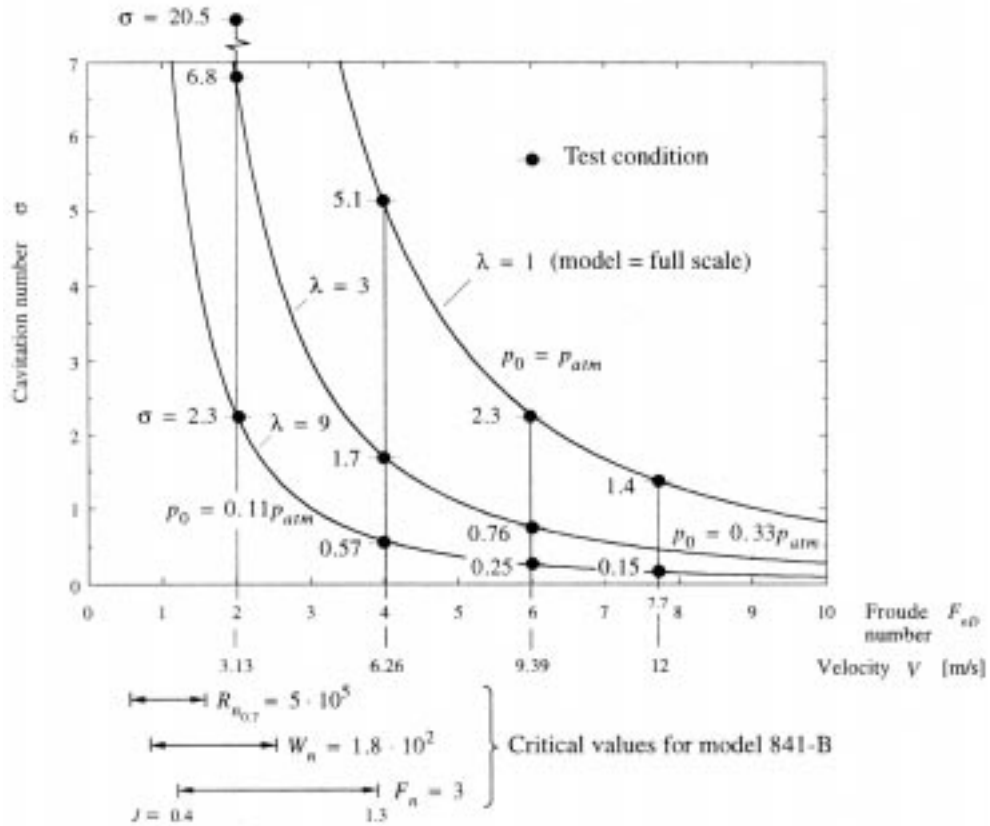


Figure 3.12: Test conditions that simultaneously satisfy cavitation and Froude number scaling. Note that the non-dimensional constants are defined as follows: $F_{nD} = V/\sqrt{gD}$. $\sigma = \sigma_v = (P_o - P_v)/(0.5\rho V^2)$. $R_n = nD^2/\nu$. $W_n = nD/\sqrt{\sigma_k/\rho D}$. σ_k is the capillarity constant of water, and $V = V_A$. Taken from [Olofsson 1996].

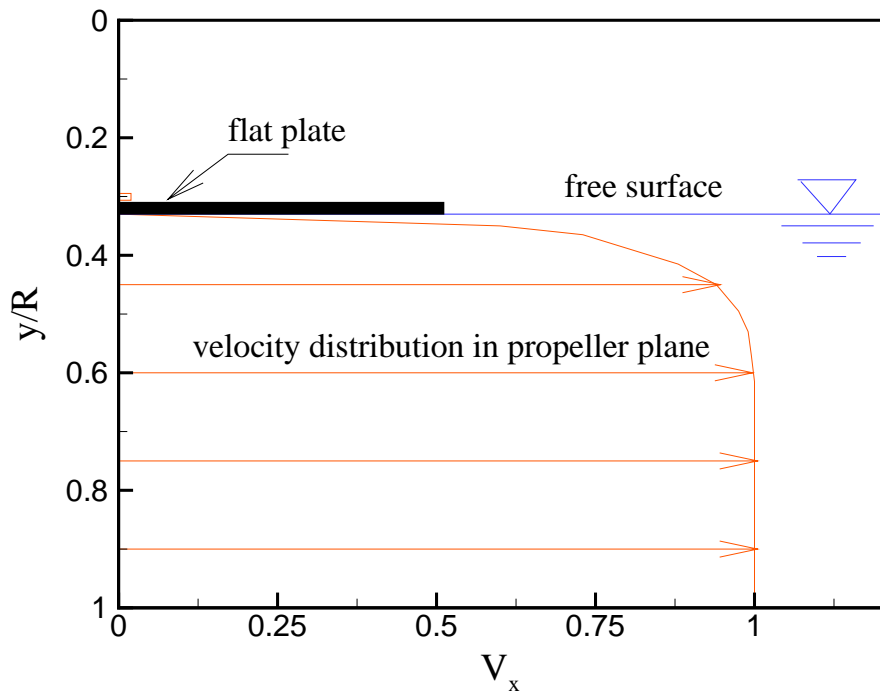


Figure 3.13: Axial velocity distribution at the propeller plane. Propeller model 841-B. $h/D = 0.33$. Reproduced from a similar figure presented in [Olofsson 1996].

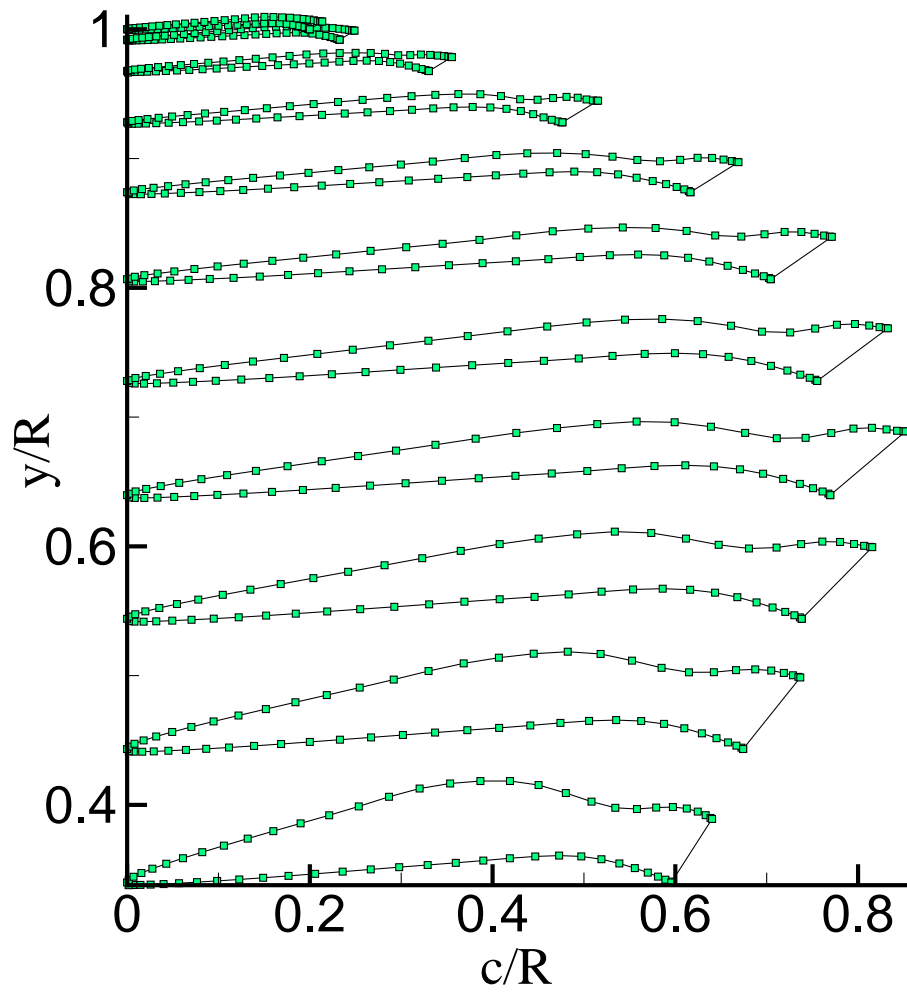


Figure 3.14: Blade section geometry of propeller model 841-B. Note that the fish tail design at the blade trailing edge is to facilitate backing conditions.

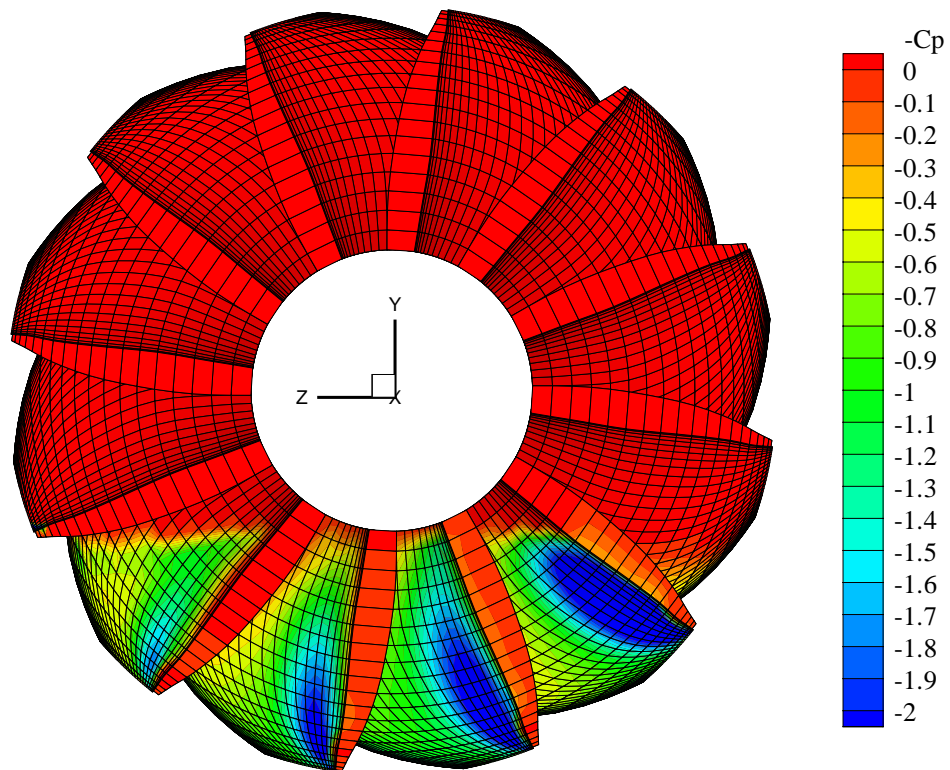


Figure 3.15: Predicted pressure contours for $J_A = 0.8$. Propeller model 841-B. 4 Blades. $h/D = 0.33$. 60x20 panels. $\Delta\theta = 6^\circ$.

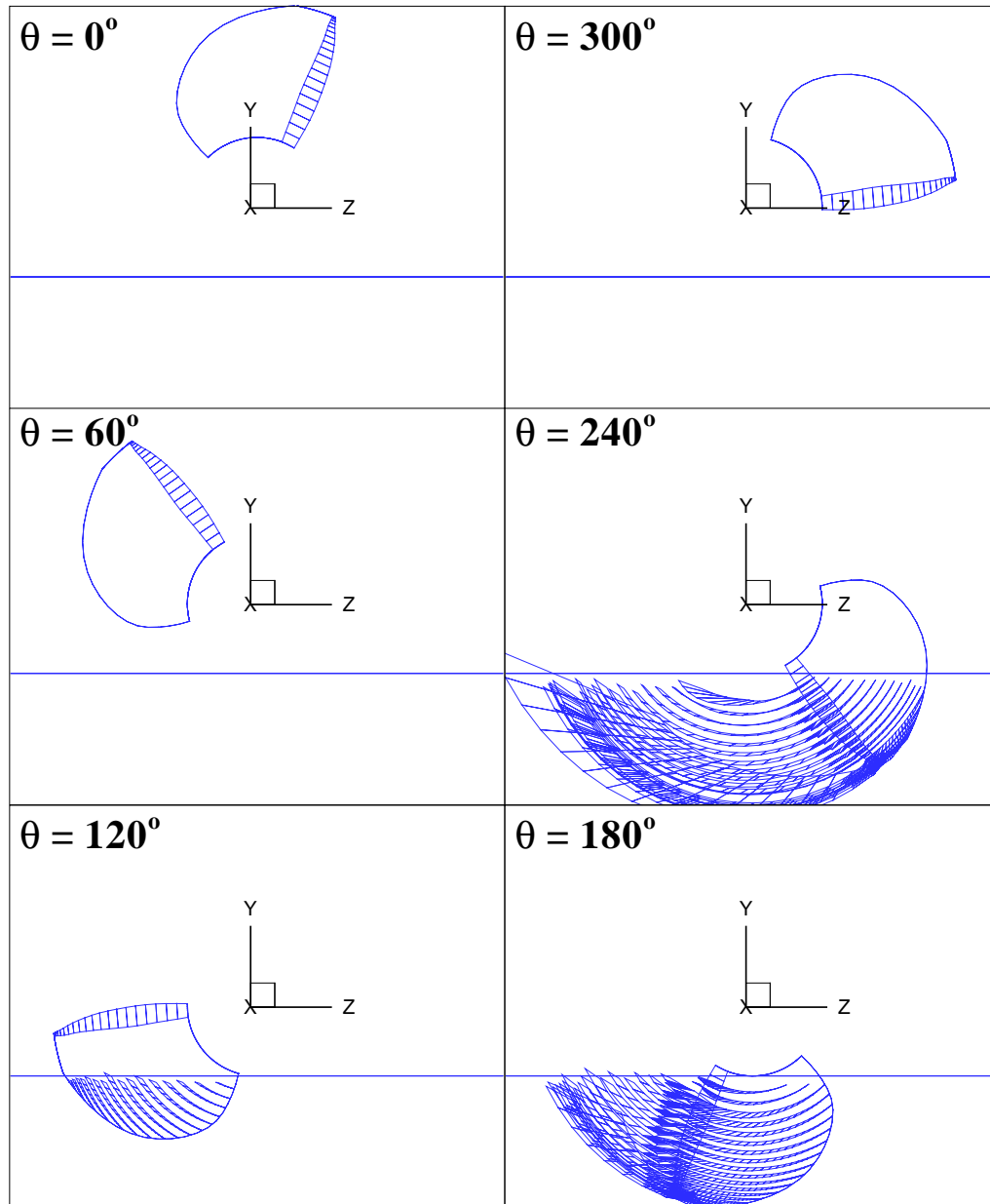


Figure 3.16: Predicted ventilated cavity patterns for $J_A = 0.8$. Propeller model 841-B. 4 Blades. $h/D = 0.33$. 60×20 panels. $\Delta\theta = 6^\circ$.

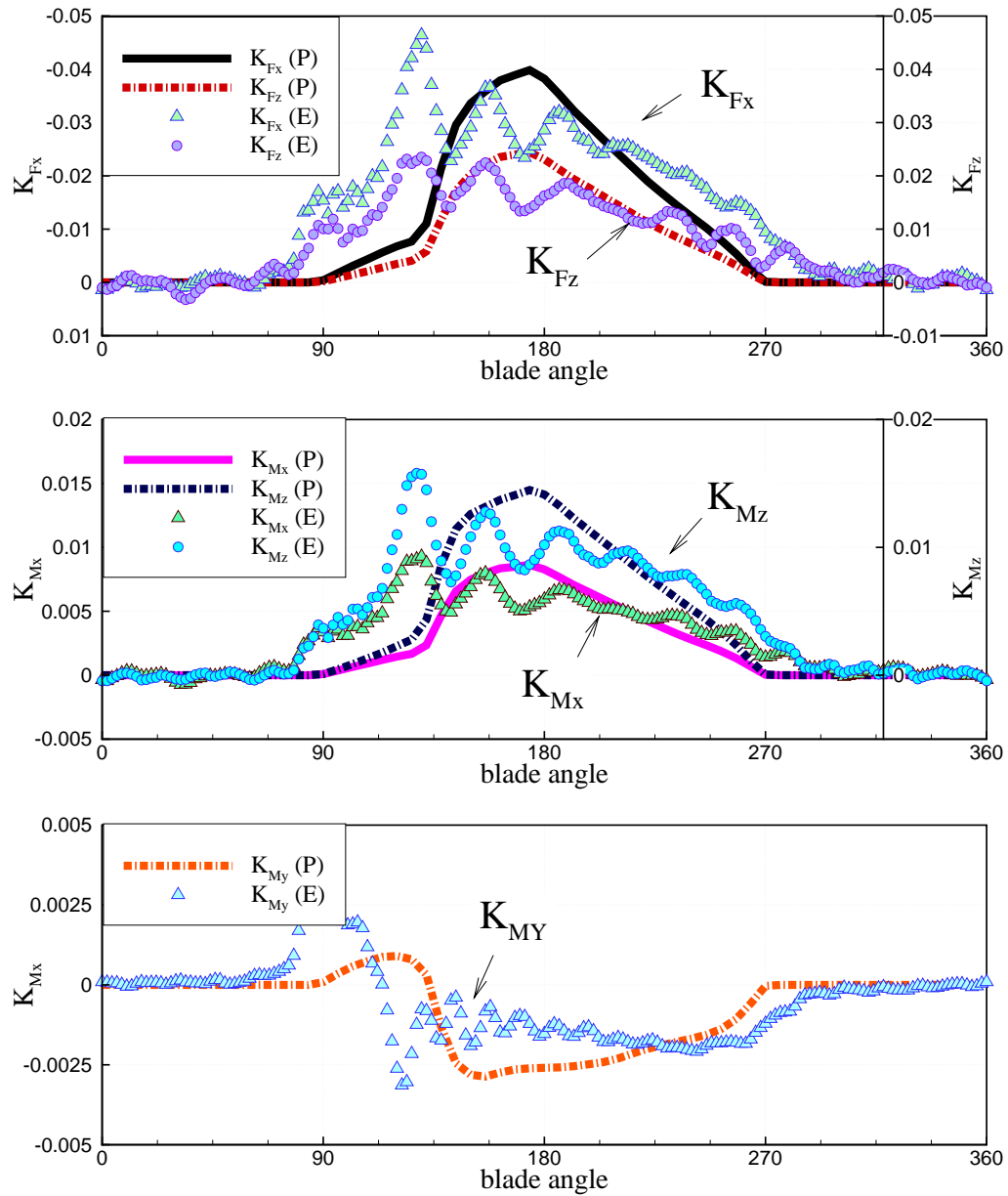


Figure 3.17: Comparison of predicted (P) and measured (E) blade forces for $J_A = 0.8$. Propeller model 841-B. 4 Blades. $h/D = 0.33$. 60x20 panels. $\Delta\theta = 6^\circ$.

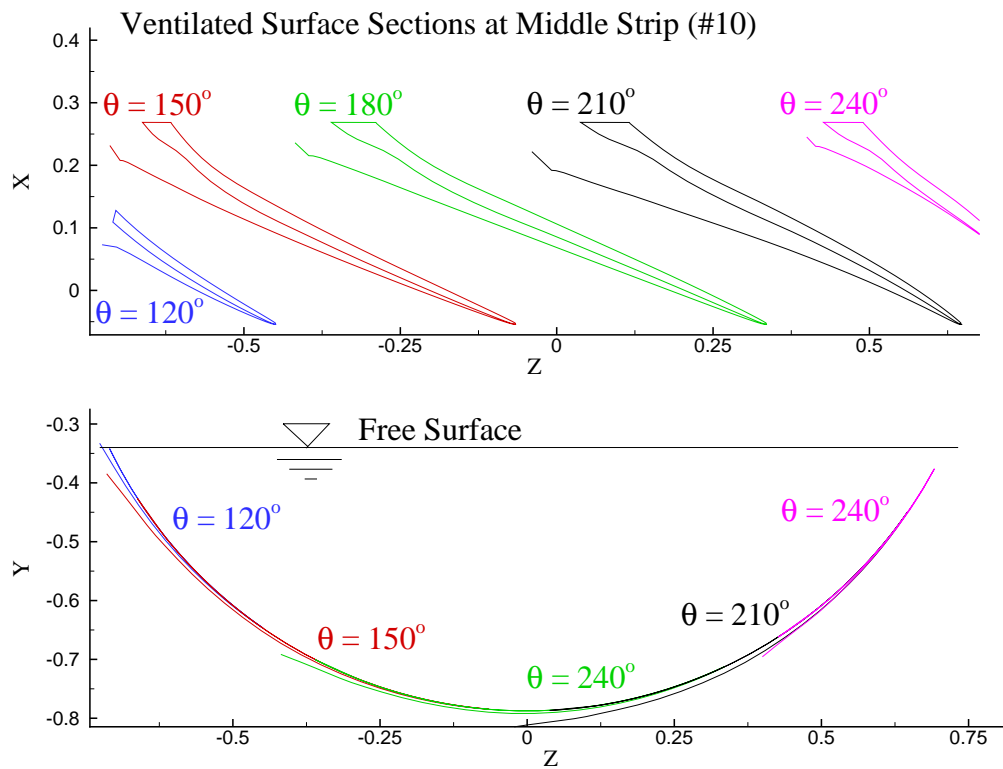


Figure 3.18: Predicted pressure contours for $J_A = 1.0$. Propeller model 841-B. 4 Blades. $h/D = 0.33$. 60x20 panels. $\Delta\theta = 6^\circ$.

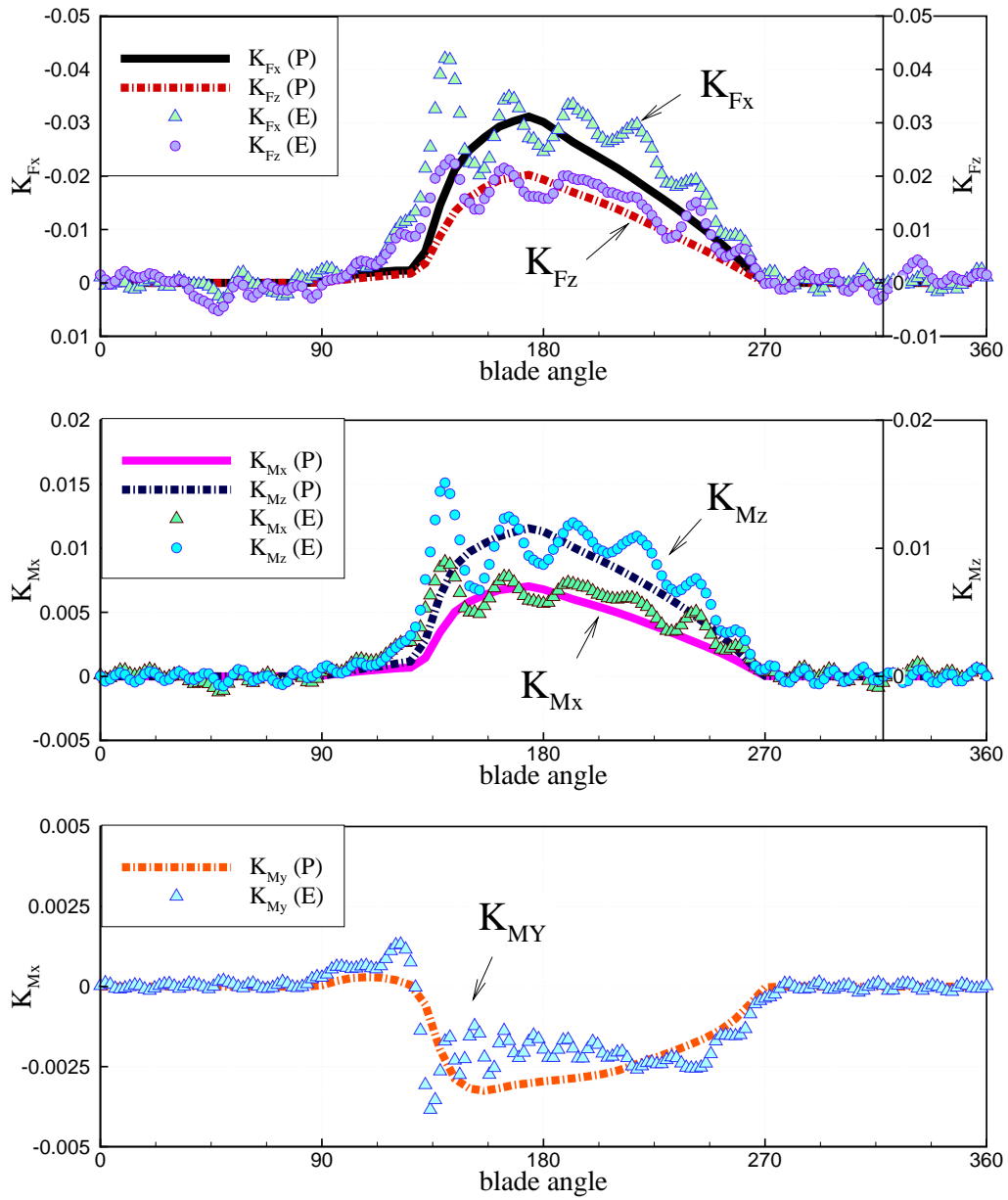


Figure 3.19: Comparison of predicted (P) and measured (E) blade forces for $J_A = 1.0$. Propeller model 841-B. 4 Blades. $h/D = 0.33$. 60x20 panels. $\Delta\theta = 6^\circ$.

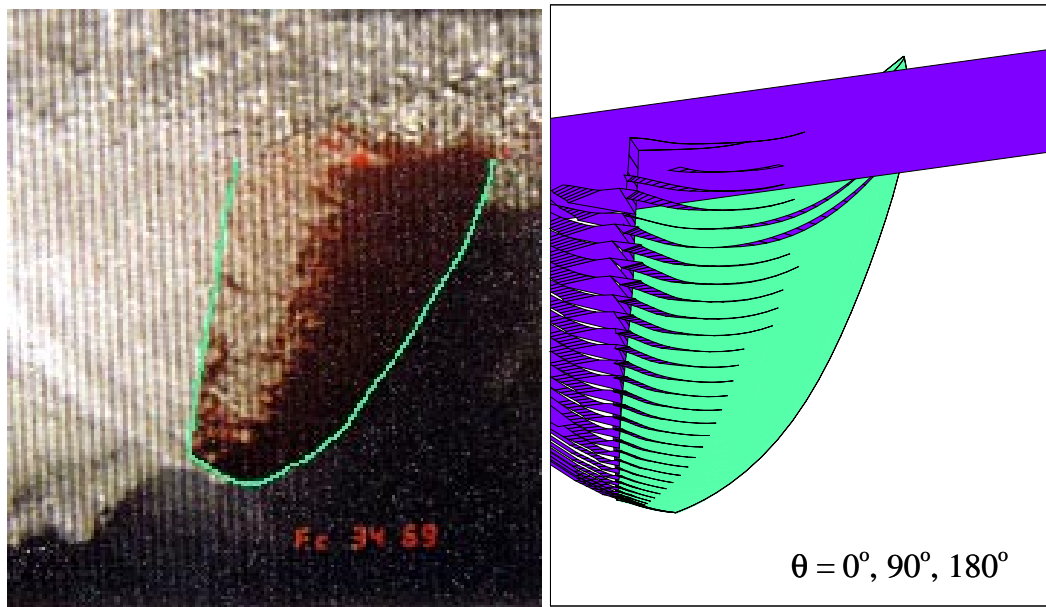


Figure 3.20: Comparison of the observed (top) and predicted (bottom) ventilated cavity patterns for $J_A = 1.2$. Propeller model 841-B. 4 Blades. $h/D = 0.33$. 60x20 panels. $\Delta\theta = 6^\circ$.

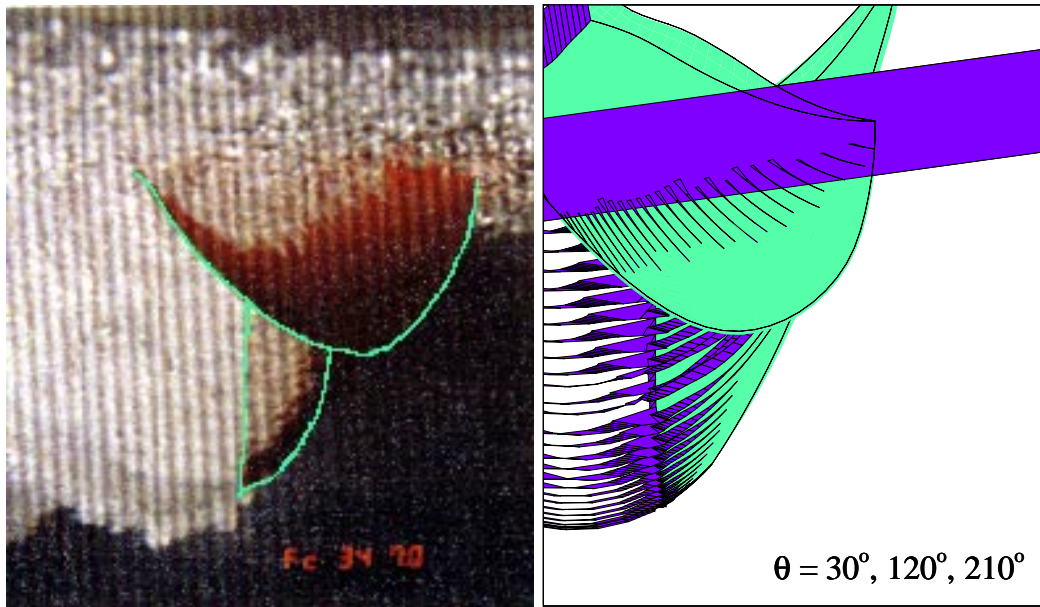


Figure 3.21: Comparison of the observed (top) and predicted (bottom) ventilated cavity patterns for $J_A = 1.2$. Propeller model 841-B. 4 Blades. $h/D = 0.33$. 60x20 panels. $\Delta\theta = 6^\circ$.

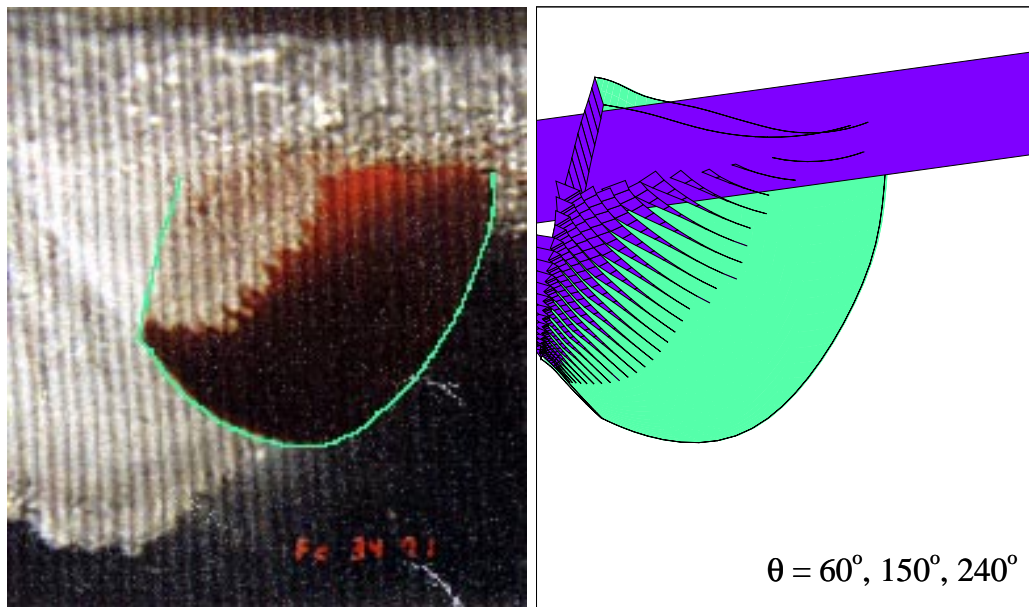


Figure 3.22: Comparison of the observed (top) and predicted (bottom) ventilated cavity patterns for $J_A = 1.2$. Propeller model 841-B. 4 Blades. $h/D = 0.33$. 60x20 panels. $\Delta\theta = 6^\circ$.

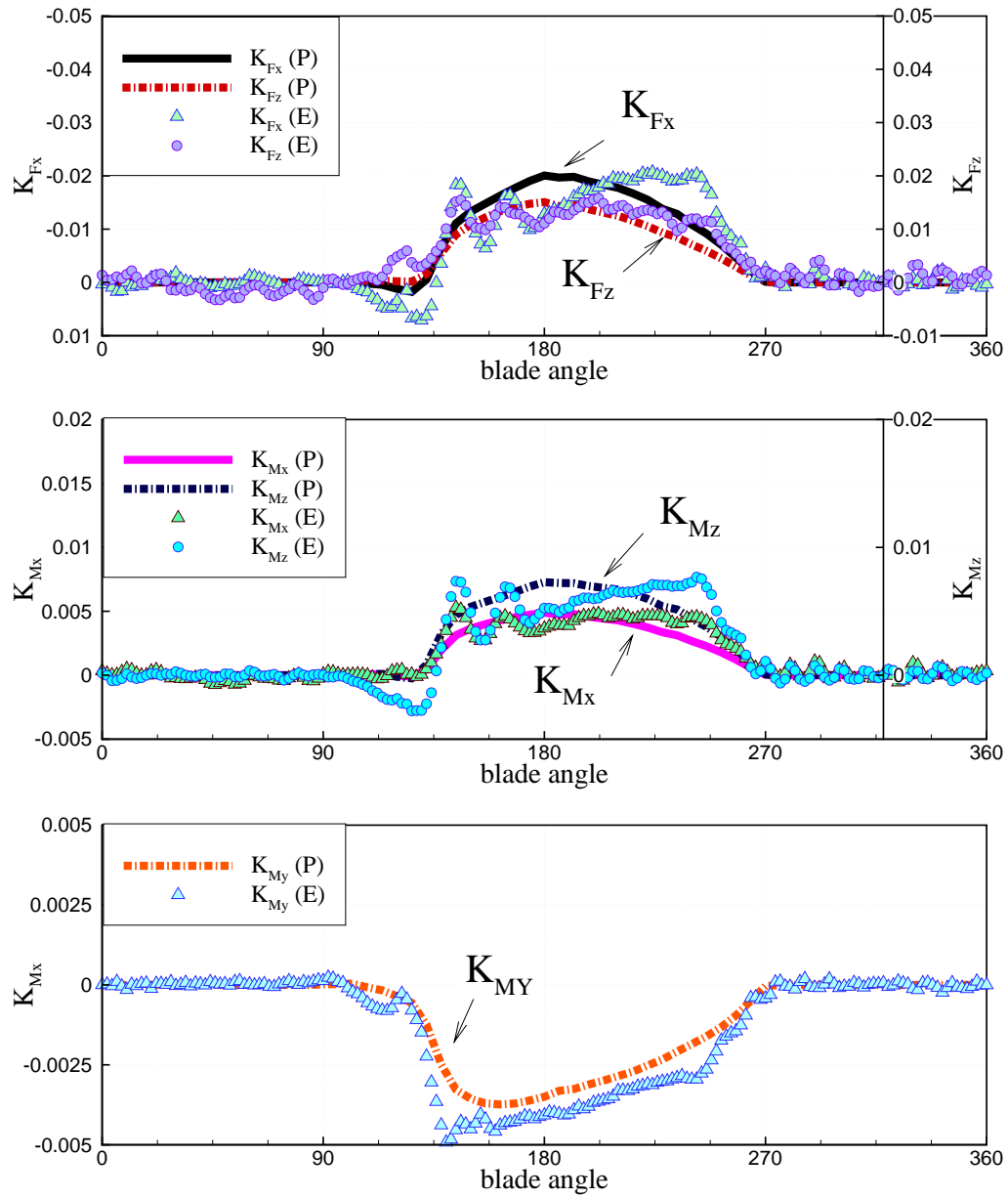


Figure 3.23: Comparison of predicted (P) and measured (E) blade forces for $J_A = 1.2$. Propeller model 841-B. 4 Blades. $h/D = 0.33$. 60×20 panels. $\Delta\theta = 6^\circ$.

3.7 Summary

A 3-D boundary element method, PROPCAV, has been extended for the analysis of partially submerged propellers. An overview of the formulation and solution method was described. Comparisons with experimental measurements for propeller model 841-B were presented. In general, the predicted ventilated cavity planforms and propeller loadings compare well with experimental measurements and observations. The method also appeared to converge quickly with number of panels. However, there were some discrepancies between the predicted and measured blade forces at the blade entry and exit phase, particularly at high speeds. In addition, the current method cannot capture the effect of blade vibration. Thus, the author is in the process of developing a fully nonlinear 2-D boundary element method to predict the added hydrodynamic forces associated with jet sprays during the entry phase. An overview of the formulation and initial results for the 2-D study are presented in the next chapter. The author also plans to study the effect of blade vibration via hydro-elastic coupling.

Chapter 4

Surface-Piercing Hydrofoils

4.1 Introduction

In order to quantify the added hydrodynamic forces associated with jet sprays generated at the blade entry and exit phase, a systematic 2-D study has been initiated. The exact nonlinear free surface boundary conditions are used and the effect of Froude number will be studied. The predicted forces on the wetted part of the hydrofoil will be compared to those obtained using the negative image method.

The planned progression of the 2-D study is shown in Fig. 4.1:

1. Vertical water entry of a symmetric wedge.
2. Oblique water entry of a surface-piercing hydrofoil.
3. Vertical water exit of a symmetric wedge.
4. Oblique water exit of a surface-piercing hydrofoil.
5. Water entry and exit of a surface-piercing hydrofoil.

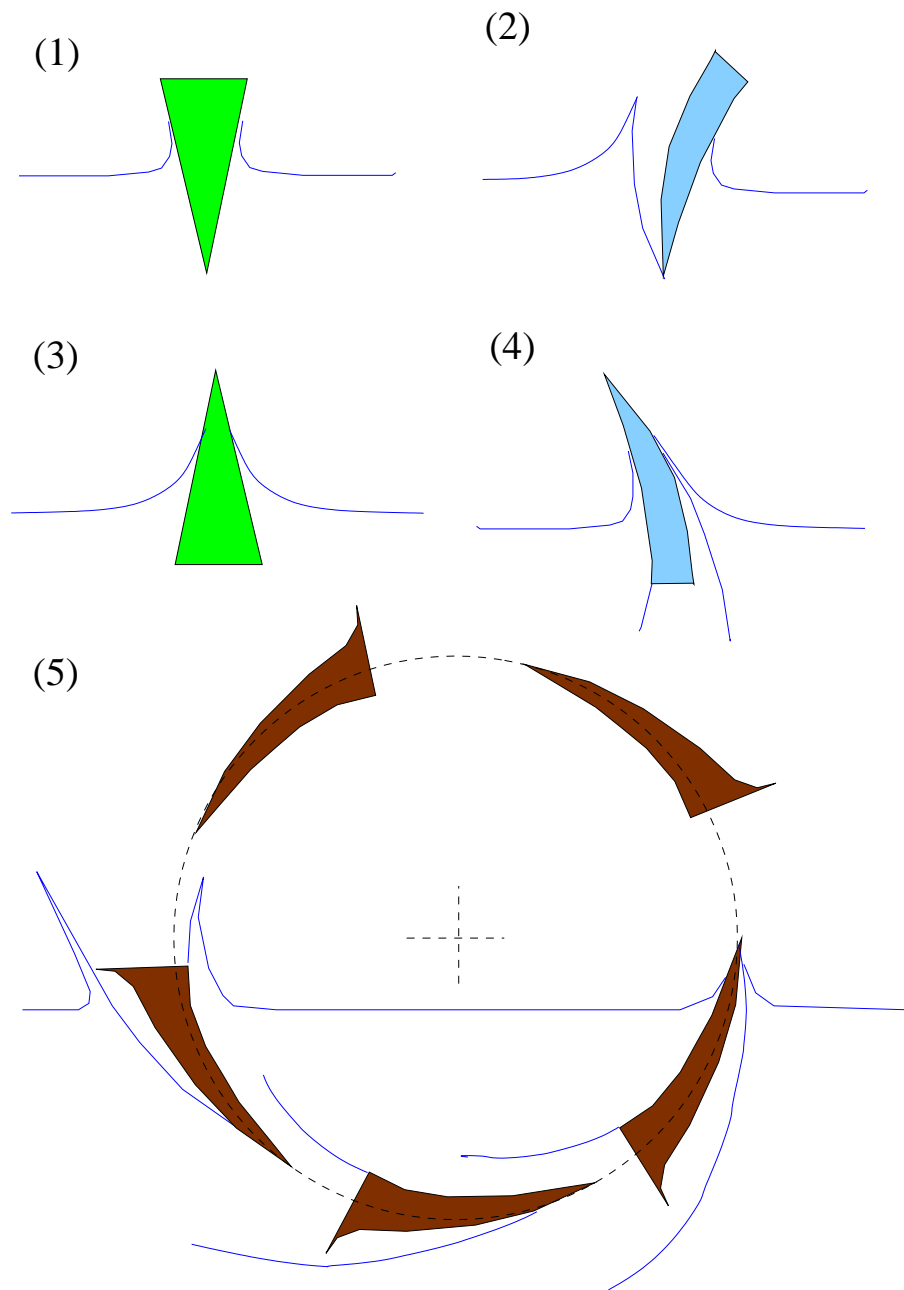


Figure 4.1: Planned progression of the 2-D nonlinear study for the water entry and exit problem of a surface-piercing hydrofoil.

4.2 Objectives

The objectives of the 2-D study are to:

1. Quantify the added hydrodynamic forces due to nonlinearity of the free surface and ventilated cavity surface.
2. Quantify the effect of Froude number.
3. Find a simplified approach to approximate the added hydrodynamic forces and, incorporate these forces into the current 3-D model.

4.3 Previous Work

The problem of a 2-D rigid wedge entering the water was first studied by [Von Karman 1929] and [Wagner 1932]. Both assumed that the velocity field around the wetted part of the body can be approximated with the flow field around an infinitely long flat plate. The model in [Von Karman 1929] assumed that the free surface is flat, while the model in [Wagner 1932] accounted for the deformation of the free surface. However, the similarity method of [Wagner 1932] reduced the unsteady problem to a steady one. Since then, the slamming problem on a 2-D body has been extensively studied by [Makie 1969; Cox 1971; Yim 1974]. In particular, [Yim 1974] applied a linearized theory to study the water entry and exit of a thin foil and a symmetric wedge with ventilation. Later, [Wang 1977, 1979] also applied linear theory to study the vertical and oblique entry of a fully ventilated foil into a horizontal layer of water with arbitrary thickness. The method of [Wang 1977,

1979] was later extended by [Furuya 1984, 1985] for the performance prediction of surface-piercing propellers.

More recently, the 2-D wedge entry problem was thoroughly investigated by [Zhao and Faltinsen 1993, 1998]. They applied a boundary element method with constant source and dipole distributions. The exact nonlinear free surface boundary condition was used. A special model was used to treat the thin jet that develops at the intersection between the free surface and the body. The method was verified by comparisons with similarity solutions by [Dobrovol'skaya 1969] and asymptotic analysis by [Wagner 1932]. Similar methods were also developed by [Lin and Ho 1994; Falch 1994; Fontaine and Cointe 1997]. However, the focus of the previous investigations was on slamming loads on ship hulls with small dead rise angles and no ventilation.

4.4 Formulation

The first step for the proposed 2-D analysis involves analyzing the flow around a rigid hydrofoil entering the water at an arbitrary angle of attack. The formulation is similar that presented in [Zhao and Faltinsen 1993], which was derived for the vertical water entry of a symmetric wedge without ventilation.

4.4.1 Problem Definition

Consider a rigid, 2-D hydrofoil entering into initially calm water of an unbounded domain at a constant velocity \vec{V} and angle attack α , as shown in Fig. 4.2. For incompressible, inviscid, and irrotational flow, the perturbation potential ϕ ,

defined with respect to the undisturbed free surface coordinates (x, y) shown in Fig. 4.2, at any time t satisfies Laplace's equation in the fluid domain:

$$\nabla^2 \phi(x, y, t) = 0 \quad (4.1)$$

Thus, the perturbation potential on the boundary, $S(t)$, of the computation domain, is represented by Green's third identity:

$$\pi \phi(x, y, t) = \int_{S(t)} \left[-\phi(\zeta, \eta, t) \frac{\partial G(\zeta, \eta, t)}{\partial n(\zeta, \eta, t)} + \frac{\partial \phi(\zeta, \eta, t)}{\partial n(\zeta, \eta, t)} G(\zeta, \eta, t) \right] dS(\zeta, \eta, t) \quad (4.2)$$

where $G = \ln r$, $r = \sqrt{(x - \zeta)^2 + (y - \eta)^2}$, and $S(t) = S_{WB}(t) \cup S_F(t) \cup S_\infty$ (defined in Fig. 4.2). Notice that $S_F(t)$ includes the free surface and the ventilated surface as a whole. \vec{n} is the unit vector normal to the integration surface, which points into the fluid domain. It should be noted that for this problem, the perturbation potential (ϕ) is the same as the total potential (Φ) since the system is defined with respect to the undisturbed free surface coordinates (x, y) .

4.4.2 Boundary Conditions

- *Kinematic Boundary Condition on S_F :*

The kinematic free surface condition requires fluid particles on the free surface and ventilated surface to remain on the surface:

$$\frac{\partial \eta}{\partial t} + \frac{\partial \phi}{\partial x} \frac{\partial \eta}{\partial x} = \frac{\partial \phi}{\partial y} \quad (4.3)$$

where $\eta(x, t)$ is the vertical coordinate of the fluid particle, as shown in Fig. 4.2.

- *Dynamic Boundary Condition on S_F :*

On the exact free surface and ventilated surface, the pressure should be constant and equal to the atmospheric pressure:

$$\frac{\partial \phi}{\partial t} + \frac{1}{2} \left[\left(\frac{\partial \phi}{\partial x} \right)^2 + \left(\frac{\partial \phi}{\partial y} \right)^2 \right] + g\eta = 0 \quad (4.4)$$

- *Combined Kinematic and Dynamic Boundary Condition on S_F :*

Equations 4.3 and 4.4 can be combined to form a system of three equations using the definition of substantial derivative, $\frac{D}{Dt} = \frac{\partial}{\partial t} + \nabla \phi \cdot \nabla$:

$$\begin{aligned} \frac{D\zeta}{Dt} &= \frac{\partial \phi}{\partial x} \\ \frac{D\eta}{Dt} &= \frac{\partial \phi}{\partial y} \\ \frac{D\phi}{Dt} &= \frac{1}{2} \left[\left(\frac{\partial \phi}{\partial x} \right)^2 + \left(\frac{\partial \phi}{\partial y} \right)^2 \right] - g\eta \end{aligned} \quad (4.5)$$

which can be written as:

$$\frac{D\vec{F}}{Dt} = \vec{G} \quad (4.6)$$

where

$$\begin{aligned}\vec{F} &= \begin{Bmatrix} \zeta \\ \eta \\ \phi \end{Bmatrix} \\ \vec{G} &= \begin{Bmatrix} \frac{\partial \phi}{\partial x} \\ \frac{\partial \phi}{\partial y} \\ \frac{1}{2} \left[\left(\frac{\partial \phi}{\partial x} \right)^2 + \left(\frac{\partial \phi}{\partial y} \right)^2 \right] - g\eta \end{Bmatrix}\end{aligned}\quad (4.7)$$

$\zeta(x, t)$ and $\eta(x, t)$ are the horizontal and vertical coordinates of the fluid particle, which at $t = 0$ was located on the undisturbed free surface at $(x, t = 0)$, as shown in Fig. 4.2.

- *Kinematic Boundary Condition on S_{WB} :*

The kinematic boundary condition requires the following condition to be satisfied on the wetted body surface:

$$\left(\nabla \phi - \vec{V} \right) \cdot \vec{n} = 0 \quad (4.8)$$

- *Kinematic Boundary Condition on S_{∞} :*

The kinematic boundary condition on the infinite boundary requires zero normal velocity across the boundary:

$$\frac{\partial \phi}{\partial n} = 0 \quad (4.9)$$

- *Initial Boundary Condition on S_F :*

The initial boundary condition on the free surface are set as follows:

$$\left. \begin{aligned} \phi(x, y, 0) &= 0 \\ \eta(x, 0) &= 0 \\ \zeta(x, 0) &= x \end{aligned} \right\} \text{ at } t = 0 \quad (4.10)$$

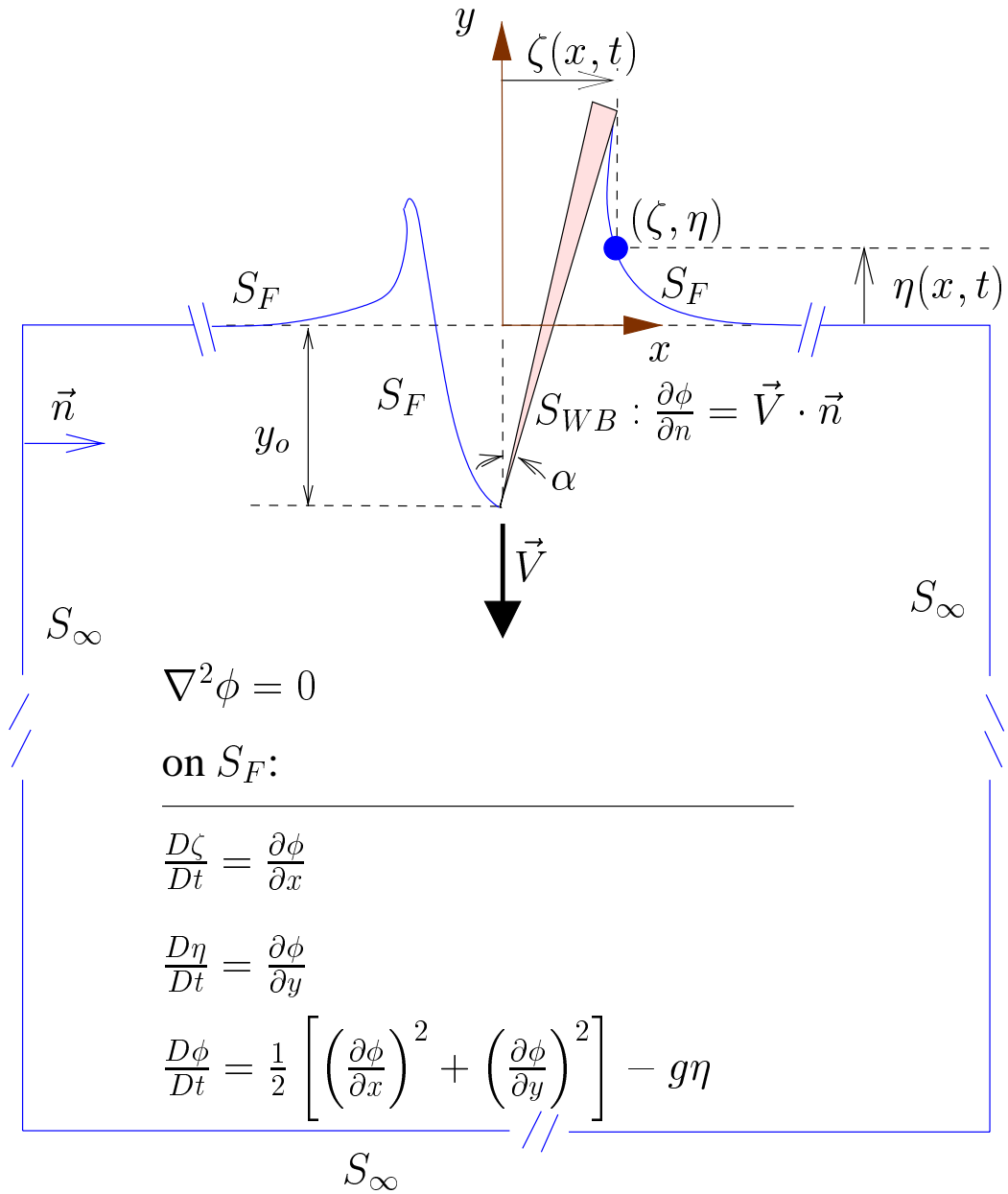


Figure 4.2: Definition of coordinate system and control surface for the water entry problem of a 2-D rigid hydrofoil.

4.5 Numerical Implementation

The integral surface, S , is discretized into a number of straight segments. In order to avoid singularities at intersection points, $\frac{\partial\phi}{\partial n}$ and ϕ for each panel are approximated with constant and linear strength distributions, respectively. The values of $\frac{\partial\phi}{\partial n}$ are assigned at the panel mid-points, and the values of ϕ are computed at the panel end points.

At each time step, Green's formula (Eqn. 4.2) is solved with respect to the unknown ϕ on S_{WB} and S_{∞} , and the unknown $\frac{\partial\phi}{\partial n}$ on S_F . The known values of $\frac{\partial\phi}{\partial n}$ on the wetted body boundary and infinite boundaries are given by Eqns. 4.8 and 4.9. The geometry and the known values of ϕ on the free surface and ventilated surface are determined by solving Eqn. 4.6 using an Adams-Bashforth-Moulton predictor-corrector method.

As the foil enters the water, thin jets with high velocity develop near the body. In order to have an accurate description of the jets, the size of the panels need to decreased, which could result in a dramatic reduction in the time step size. To avoid this problem, the current method follows the technique described in [Zhao and Faltinsen 1993]. The free surface panel adjacent to the solid body is cut when the slope of the free surface is parallel to the body contour. The threshold limit for ϵ (shown in Fig. 4.3) is $\pi/9$. When the threshold limit is reached, the free surface panel adjacent to the body is replaced by a "jet" panel that is perpendicular to the body contour. In order to avoid instabilities, the values of ϕ and $\frac{\partial\phi}{\partial n}$ are assumed to be known on the jet panel. The value of ϕ at the intersection between the body and the free surface is obtained via cubic extrapolation of the potentials on the adjacent

wetted body panels. The value of $\frac{\partial\phi}{\partial n}$ at the midpoint of the jet panel is obtained via cubic extrapolation of the tangential velocity at the adjacent wetted body panels.

A schematic representation of the known and unknown for the 2-D foil entry problem is shown in Fig. 4.3.

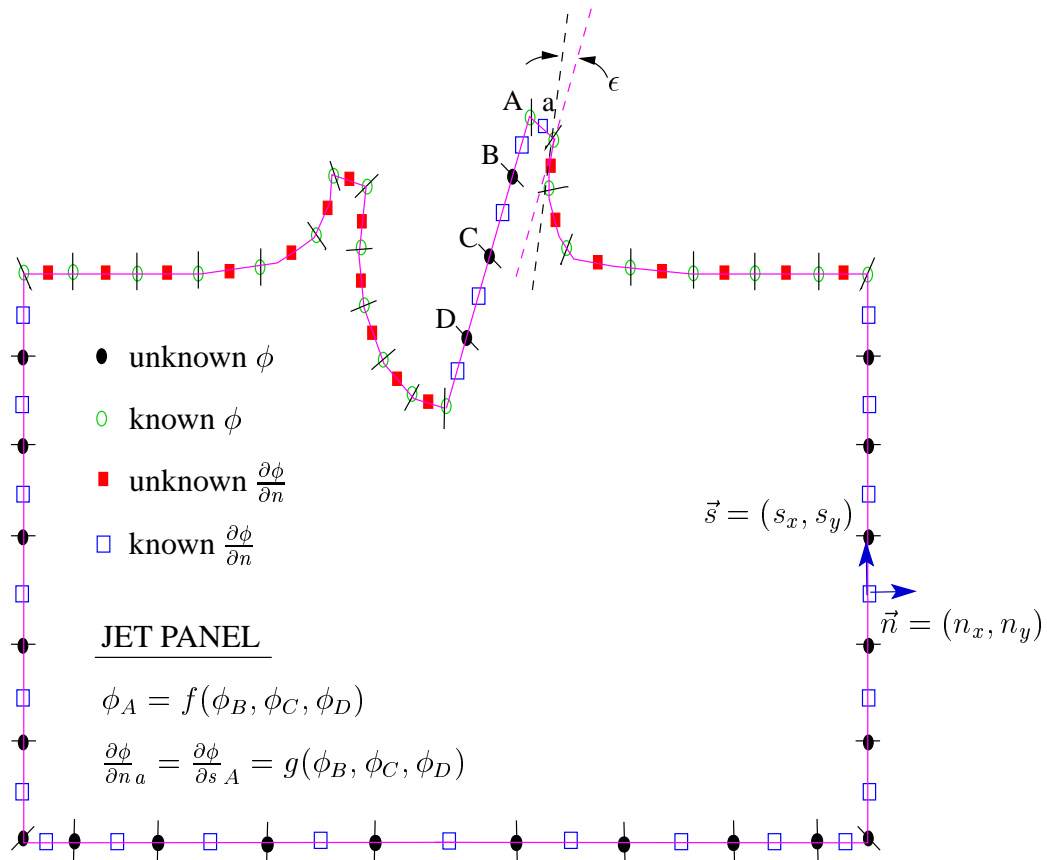


Figure 4.3: A schematic representation of the known and unknown for the 2-D rigid foil entry problem.

4.5.1 Time-Integration Scheme

In the time integration, the new particle position and new values of ϕ on the free surface and ventilated surface are calculated by time stepping the fluid particle at the mid-points of the old elements. As explained in [Zhao and Faltinsen 1993], the details of the new element procedure is very important in order to conserve fluid mass, particularly in regions of high curvature. In the current scheme, a cubic spline method is used to: (1) calculate the position and potential of particles at panel mid-points based on the existing values at panel endpoints, and (2) calculate the position and potential at panel endpoints based on the updated positions of panel mid-points. It should be noted that the cubic spline method is only employed for regions of high curvature, i.e. regions near the jet and ventilated surface. The time stepping procedure used to solve Eqn. 4.6 is explained below.

• *Predictor step for time $t + 1$:*

1. Compute ζ , η , and ϕ at panel mid-points on S_F at time $t + 1$ using a second-order explicit Adams-Bashforth predictor method:

$$\vec{F}_{i+\frac{1}{2},t+1}^p = \vec{F}_{i+\frac{1}{2},t} + \frac{\Delta t}{2} \left[3\vec{G}_{i+\frac{1}{2},t} - \vec{G}_{i+\frac{1}{2},t-1} \right] \quad (4.11)$$

2. Refine the panel distribution in highly curved regions. Calculate $\vec{F}_{i+\frac{1}{2},t}^p$, $\vec{G}_{i+\frac{1}{2},t}$, and $\vec{G}_{i+\frac{1}{2},t-1}$ at new panel midpoints.
3. Apply Eqns. 4.8 and 4.9 to determine the known values of $\frac{\partial \phi^p}{\partial n}_{i+\frac{1}{2},t+1}$ on the wetted body boundary and infinite boundary, respectively.

4. Solve Green's formula, Eqn. 4.2, to obtain $\phi_{i,t+1}^p$ and $\frac{\partial \phi^p}{\partial n}_{i+\frac{1}{2},t+1}$ everywhere.

5. Calculate velocities at panel mid-points:

$$\begin{aligned}\frac{\partial \phi^p}{\partial x}_{i+\frac{1}{2},t+1} &= \left[\frac{\partial \phi}{\partial s} s_x + \frac{\partial \phi}{\partial n} n_x \right]_{i+\frac{1}{2},t+1}^p \\ \frac{\partial \phi^p}{\partial y}_{i+\frac{1}{2},t+1} &= \left[\frac{\partial \phi}{\partial s} s_y + \frac{\partial \phi}{\partial n} n_y \right]_{i+\frac{1}{2},t+1}^p\end{aligned}\quad (4.12)$$

where $\vec{s} = (s_x, s_y)$ and $\vec{n} = (n_x, n_y)$ are the tangential and normal unit vectors, respectively. Note that values of ϕ are known at the panel endpoints and values of $\frac{\partial \phi}{\partial n}$ are known at the panel mid-points. Thus, $\frac{\partial \phi}{\partial s}$ is calculated as follows:

$$\frac{\partial \phi^p}{\partial s}_{i+\frac{1}{2},t+1} = \frac{\phi_{i+1,t+1}^p - \phi_{i,t+1}^p}{s_{i+1,t+1}^p - s_{i,t+1}^p}\quad (4.13)$$

where $s_{i+1,t+1}^p$ is the arclength of panel endpoint $i + 1$ at time $t + 1$ for the predictor step.

6. Calculate $\vec{G}_{i+\frac{1}{2},t+1}^p$ on S_F .

• *Corrector Step for Time $t + 1$:*

1. Compute ζ , η , and ϕ at panel mid-points on S_F at time $t+1$ using a third-order implicit Adams-Moulton corrector method:

$$\vec{F}_{i+\frac{1}{2},t+1} = \vec{F}_{i+\frac{1}{2},t} + \frac{\Delta t}{12} \left[5\vec{G}_{i+\frac{1}{2},t+1}^p + 8\vec{G}_{i+\frac{1}{2},t} - \vec{G}_{i+\frac{1}{2},t-1} \right]\quad (4.14)$$

2. Refine the panel distribution in highly curved regions. Calculate $\vec{F}_{i+\frac{1}{2},t+1}$ and $\vec{G}_{i+\frac{1}{2},t}$ at new panel midpoints.

3. Apply Eqns. 4.8 and 4.9 to determine the known values of $\frac{\partial\phi}{\partial n}_{i+\frac{1}{2},t+1}$ on the wetted body boundary and infinite boundary, respectively.
4. Solve Green's formula, Eqn. 4.2, to obtain $\phi_{i,t+1}$ and $\frac{\partial\phi}{\partial n}_{i+\frac{1}{2},t+1}$ everywhere.
5. Calculate velocities, $\frac{\partial\phi}{\partial x}_{i+\frac{1}{2},t+1}$ and $\frac{\partial\phi}{\partial y}_{i+\frac{1}{2},t+1}$, at panel mid-points.
6. Calculate $\vec{G}_{i+\frac{1}{2},t+1}$ on the free surface.

4.5.2 Pressure and Impact Force Calculation

The pressure at the wetted body surface is calculated at panel mid-points of each time t via Bernoulli's Equation:

$$\left(\frac{P}{\rho}\right)_{i+\frac{1}{2},t} = -\frac{\partial\phi}{\partial t}_{i+\frac{1}{2},t} - g\eta_{i+\frac{1}{2},t} - \frac{1}{2} \left[\left(\frac{\partial\phi}{\partial x}\right)^2 + \left(\frac{\partial\phi}{\partial y}\right)^2 \right]_{i+\frac{1}{2},t} \quad (4.15)$$

where $\frac{\partial\phi}{\partial t}_{i+\frac{1}{2},t}$ is calculated as follows:

$$\frac{\partial\phi}{\partial t}_{i+\frac{1}{2},t} = \frac{D\phi}{Dt}_{i+\frac{1}{2},t} - \left[\left(\frac{\partial\phi}{\partial x}\right)^2 + \left(\frac{\partial\phi}{\partial y}\right)^2 \right]_{i+\frac{1}{2},t} \quad (4.16)$$

and

$$\frac{D\phi}{Dt}_{i+\frac{1}{2},t} = \frac{1}{2\Delta t} \left(\phi_{i+\frac{1}{2},t+1} - \phi_{i+\frac{1}{2},t-1} \right) \quad (4.17)$$

Once the pressure has been computed, the impact force can be calculated by integrating the pressure over the wetted area on the solid body.

4.6 Preliminary Results

4.6.1 Vertical Entry of a Symmetric Wedge

In order to validate the method, the predictions for the 2-D wedge entry problem are first compared with those presented in [Zhao and Faltinsen 1993]. Note that the formulation for the water entry problem of 2-D symmetric wedge is the same as that explained in above with the following exceptions:

- The wedge is symmetric with respect to the y -axis.
- There is no ventilated cavity surface. Thus, S_F only includes the free surface.

For surface-piercing hydrofoil/propeller applications, the dead-rise angle is often very high (i.e. $\alpha < 10^\circ$). Thus, the case of $\alpha = 9^\circ$ (highest dead-rise angle presented in [Zhao and Faltinsen 1993]) is selected for validation studies. The predicted free surface elevation and pressure distribution on the body are shown in Fig. 4.4. The current method compares very well with predictions by [Zhao and Faltinsen 1993], which is also shown in Fig. 4.4.

4.6.2 Oblique Entry of a Flat Plate

To further validate the method, numerical predictions for the oblique entry of a flat plate are also presented. The predicted pressure distributions for $\alpha = 5^\circ$ and 8° are shown in Figs. 4.5 and 4.6, respectively. Also shown in Figs. 4.5 and 4.6 are the results obtained using the method of [Savineau and Kinnas 1995], which applied the linearized free surface boundary conditions. As expected, the current

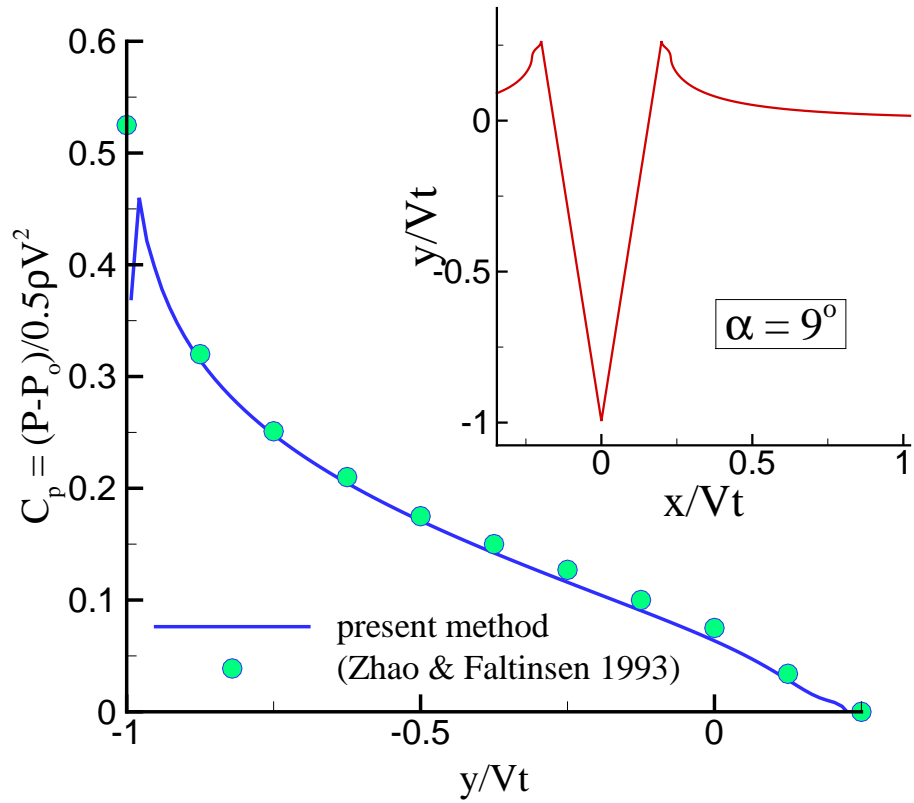


Figure 4.4: Predicted free surface elevation and pressure distribution during water entry of a 2-D wedge. $\alpha = 9^\circ$.

method predicted higher forces and increased wetted area compared to [Savineau and Kinnas 1995].

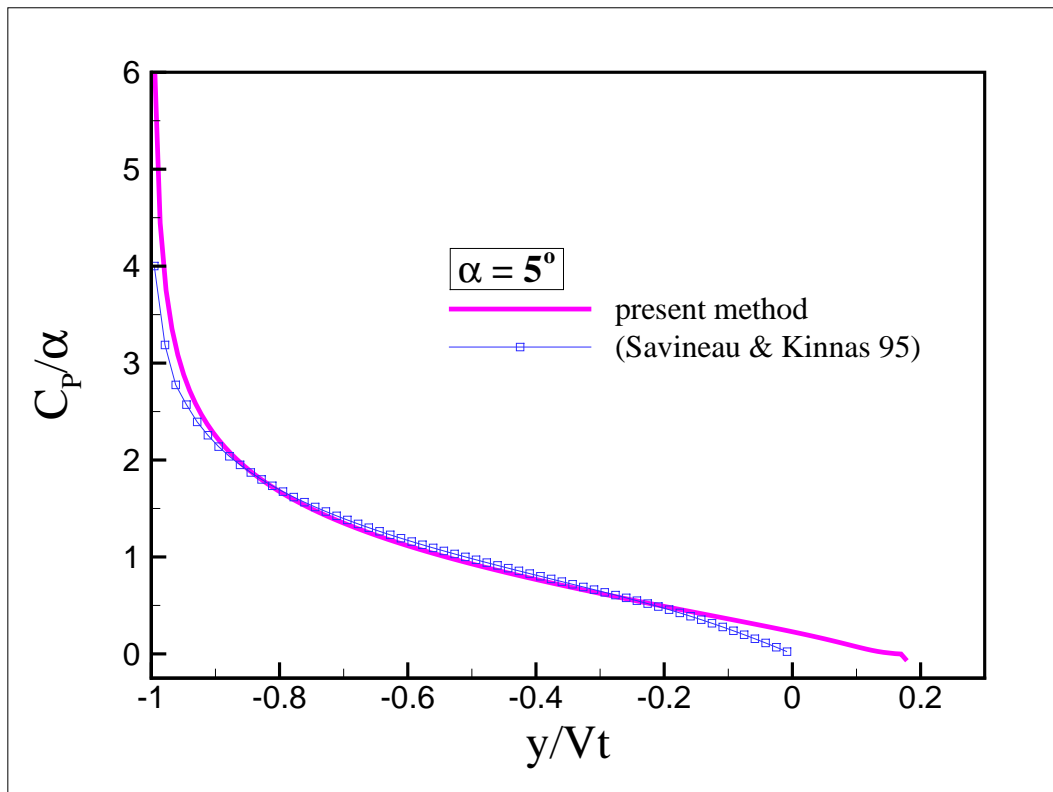


Figure 4.5: Pressure distribution on the wetted body surface predicted by the present method and by the method of [Savineau and Kinnas 1995]. Flat plate. $\alpha = 5^\circ$.

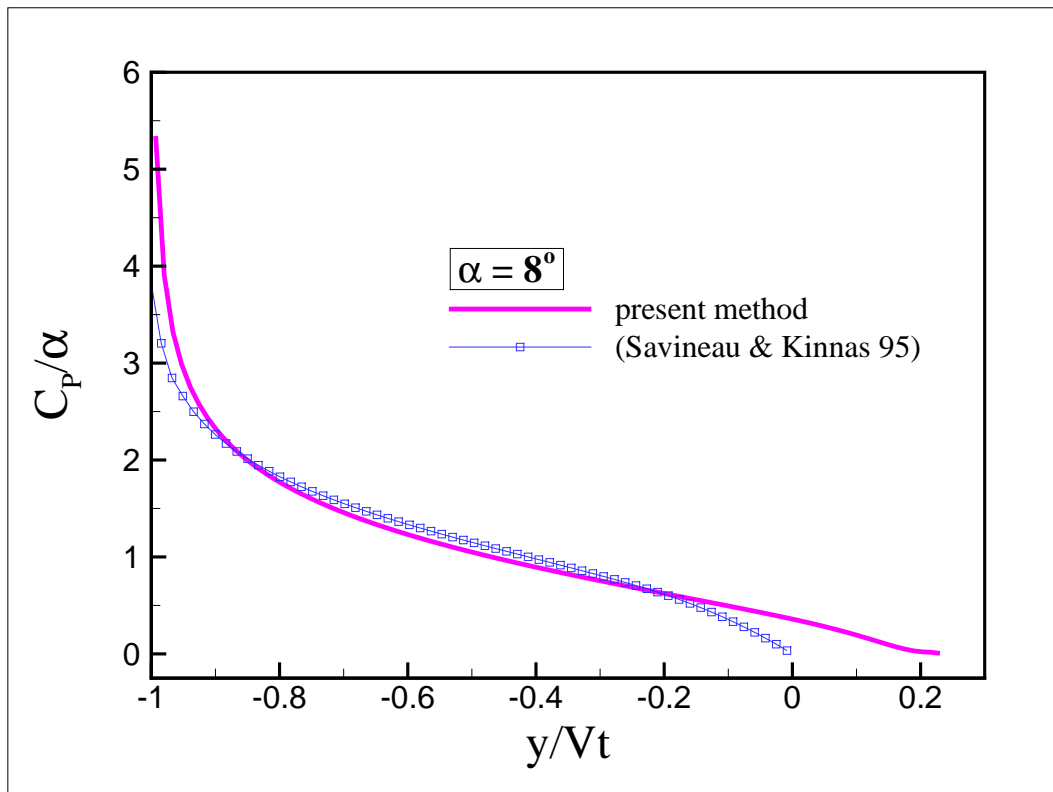


Figure 4.6: Pressure distribution on the wetted body surface predicted by the present method and by the method of [Savineau and Kinnas 1995]. Flat plate. $\alpha = 8^\circ$.

4.7 Summary

A 2-D study using the exact free surface boundary conditions has been initiated to quantify the added hydrodynamic forces associated with jet sprays during the entry phase. An overview of the formulation and preliminary results for the water entry problem was presented. For the problem of a rigid wedge entering the free surface, the predicted results compared well with the those presented in [Zhao and Faltinsen 1993]. The method also predicted reasonable pressure distributions for the problem of a flat plate entering the free surface with ventilation. However, additional studies are needed to study the stability and convergence characteristics of the method. Furthermore, the method needs to be extended to analyze the problem of a hydrofoil exiting the free surface.

Chapter 5

Conclusions

5.1 Conclusions

In conclusion, a 3-D boundary element method has been extended to predict the performance of supercavitating and surface-piercing propellers. In the past, the BEM was only able to predict the performance of unsteady partial back cavitation on conventional fully submerged propellers. Contributions of this work include:

- Development of an algorithm to search for alternating or simultaneous face and back cavitation on submerged propellers. This is the first method that can predict such complicated, yet realistic, combinations of cavity patterns in steady and unsteady flow conditions. As demonstrated in the example using a 3-D hydrofoil, the cavity detachment location, as well as the presence of face cavitation, can significantly affect the hydrodynamic forces.
- Development of the first 3-D BEM to simulate the unsteady separated region behind blade sections with non-zero trailing edge thickness. The present method is applicable to fully wetted, partially cavitating, and supercavitating conditions in steady and unsteady flows.
- Development of the first 3-D BEM to predict the hydrodynamic performance

of surface-piercing propellers. The method is able to simulate unsteady ventilation patterns, with leading edge or midchord detachment, on a surface-piercing propeller. The predicted hydrodynamic blade force coefficients are also in general good agreement with experimental measurements.

- Development of the first 2-D BEM with exact free surface boundary conditions to solve the water entry problem of a surface-piercing hydrofoil. This is the first step to understand the fluid mechanics as the foil enters and exits the free surface. The ultimate objective is to predict the added hydrodynamic forces on a surface-piercing propeller due to nonlinear free surface effects.

The method was validated extensively in the case of 3-D hydrofoils and propellers, and the results were found to converge quickly with time and space discretizations. The numerical predictions also compared well with experimental measurements and observations. However, additional studies are needed to model the effect of jet sprays and blade vibration for surface-piercing propellers.

5.2 Discussions and Recommendations

5.2.1 Alternating or Simultaneous Face and Back Cavitation

Although alternating or simultaneous face and back cavitation are becoming more and more common in recent propeller designs, the author is not aware of any published experimental results. To truly validate the method, systematic comparisons should be made between the predicted and measured cavitation patterns and blade forces. Additional studies are also needed to test the sensitivity of method

to different space and time discretizations for a wide range of propeller geometries and operating conditions. In the case of unsteady face and back cavitation, the following concerns should also be addressed:

- The hydroelastic response of the propeller, particularly in the case of alternating face and back cavitation.
- A more comprehensive wake model, such as the one presented in [Lee 2002], should be incorporated to the current method. At this time, the wake is aligned with the circumferentially averaged inflow. However, most propellers that exhibit face and back cavitation patterns are subjected to inclined inflow. In that case, the time-invariant wake model may be an oversimplification.

5.2.2 Supercavitating Propellers

For supercavitating propellers, the current method assumes the pressure to be constant and equal to the vapor pressure on the separated region behind non-zero thickness blade trailing edge sections. Based on this assumption, the method is able to predict the extent and thickness of the separated region in steady and unsteady flow conditions. However, additional studies are needed to determine the effect of prescribed separated region pressure on the predicted blade forces in the case of fully wetted and partially cavitating flow. Under the current algorithm, it is actually possible to prescribe a different pressure, such as that measured in experiment or computed using viscous flow analysis, on the separated region. A more careful study is also needed to predict how the pressure changes along the trailing edge

when one part of the blade is wetted or partially cavitating, and another is supercavitating. Additional validation and convergence are also needed before this method can be reliably use for the design and analysis of supercavitating propellers. The two concerns listed in Section 5.2.1 for the prediction of face and back cavitation should also be addressed for supercavitating propellers.

5.2.3 Surface-Piercing Propellers

Although the current performance prediction of surface piercing propellers are in reasonable agreement with experiments, considerable research are required before the method can be reliably use in the design and analysis of surface-piercing propellers:

- Modeling of the partially submerged panels. This can be accomplished by using a method similar to the split-panel technique.
- Modeling of the jet sprays. Complete the current 2-D nonlinear study of surface-piercing hydrofoils, and find a simplified approach to incorporate the results into the 3-D model. A possible algorithm is provided below:
 1. Solve the 3-D problem using the negative image method.
 2. Apply the 2-D algorithm to each radial blade section, assuming the incident angle is determined by the sectional geometry and global flow velocities (i.e. inflow velocity and propeller induced velocities).
 3. Perform the same 2-D calculation using the negative image method.

4. Calculate the difference between the 2-D fully nonlinear solution from that obtained using the 2-D negative image method. Apply the calculated corrections to the sectional lift and drag coefficients in the 3-D model using the assumed incidence angles. This can be a fast, but reasonable, approach for the design of surface-piercing propellers.
- Modeling of the blade vibration via hydroelastic coupling. A possible algorithm is provided below:
 1. Perform the hydrodynamic analysis (using the current 3-D BEM) assuming the blade the rigid.
 2. Perform the structural analysis (using a 3-D finite element method) with the unsteady pressures obtained from (1) as input.
 3. Perform the hydrodynamic analysis using the deformed blade geometry from (2). Note that the distortion on each blade may be different. In addition, the blade deformation at each blade angle may also be different. Furthermore, the effect of the unsteady blade motion should also be included in the hydrodynamic analysis. This effect can be approximated by modifying the kinematic boundary conditions:

$$\frac{\partial \phi}{\partial n} = -\vec{q}_{in} \cdot \vec{n} + \frac{\partial \eta_c}{\partial t} \quad (5.1)$$

where η_c is the vertical coordinate of the mean-camber line with respect to the nose tail line.

4. Perform the structural analysis based on the new blade geometry and pressure distributions.

5. Repeat steps (3) and (4) until the blade forces converge.
- Coupling the method with an unsteady Euler solver to obtain a more realistic effective wake velocity.
 - Include a more realistic wake alignment model, especially for cases with non-zero shaft yaw and inclination angle.

Bibliography

- Achkinadze, A. S. and Fridman, G. M. (1995). On some aspects of design of supercavitating foils and propellers. variation and asymptotic approach. In *PROPCAV '95: An International Conference on Propeller Cavitation*, pages pp. 163–174, Newcastle Upon Tyne, United Kingdom.
- Acosta, A. (1955). A note on partial cavitation of flat plate hydrofoils. Technical Report No. E-19.9, California Institute of Technology, Hydrodynamics Laboratory.
- Allison, J. (1978). Propellers for high-performance craft. *Marine Technology*, 15(4):pp. 335–380.
- Angell, B., Long, R., Weaver, W., and Hibbert, J. (1979). Cavitation resistant coatings for naval use. In *International Conference on Erosion by Liquid and Solid Impact*, Cambridge, England.
- Arakeri, H. (1975). Viscous effects on the position of cavitation separation from smooth bodies. *Journal of Fluid Mechanics*, vol 68(No. 4):pp 779–799.
- Barnaby, S. W. (1897). On the formation of cavities in water by screw propellers at high speed. *Transactions of Institute of Naval Architecture*, 38.
- Barr, R. A. (1970). Supercavitating and superventilated propellers. *Transactions of SNAME*, 78:pp. 417–450.

- Batchelor, G. K. (1967). *An Introduction to Fluid Dynamics*. Cambridge University Press.
- Birkhoff, G. and Zarantonello, E. (1957). *Jets, Wakes and Cavities*. Academic Press Inc., New York.
- Boswell, R. (1971). Design, cavitation performance and open-water performance of a series of research skewed propellers. Technical Report 3339, DTNSRDC.
- Brandt, H. (1973). Modellversuche mit schiffspropellern an der wasseroberfläche. *Schiff und Hafen*, 25(5):pp. 415–422.
- Breslin, J., Van Houten, R., Kerwin, J., and Johnsson, C.-A. (1982). Theoretical and experimental propeller-induced hull pressures arising from intermittent blade cavitation, loading, and thickness. *Trans. SNAME*, 90.
- Brewer, W. and Kinnas, S. (1997). Experiment and viscous flow analysis on a partially cavitating hydrofoil. *Journal of Ship Research*, 41(3):pp. 161–171.
- Brillouin, M. (1911). Les surfaces de glissement de Helmholtz et la resistance des fluides. *Annales de Chimie and de Physique*, vol. 23:pp. 145–230.
- Caponnetto, M. and Brizzolara, S. (1995). Theory and experimental validation of a surface panel method for the analysis of cavitating propellers in steady flow. In *PROPCAV '95: An International Conference on Propeller Cavitation*, page pp. 239, Newcastle Upon Tyne, United Kingdom.

- Choi, J. (2000). *Vortical Inflow – Propeller Interaction Using Unsteady Three-Dimensional Euler Solver*. PhD thesis, Department of Civil Engineering, The University of Texas at Austin.
- Choi, J.-K. and Kinnas, S. (2000a). Non-axisymmetric effective wake prediction by using an unsteady three-dimensional Euler solver. In *Propellers/Shafting 2000 Symposium*, pages 1–14 (paper No. 14), Virginia Beach, VA. Soc. Naval Arch. & Marine Engrs.
- Choi, J.-K. and Kinnas, S. (2000b). An unsteady 3-D Euler solver coupled with a cavitating propeller analysis method. In *23rd Symposium on Naval Hydrodynamics*, Val de Reuil, France.
- Choi, J.-K. and Kinnas, S. (2001). Prediction of non-axisymmetric effective wake by a 3-D Euler solver. *Journal of Ship Research*, 45(1):13–33.
- Coleman, e. a. (1987). Acoustic cavitation generated by an extracorporeal shock-wave lithotripter. *Ultrasound in Medicine and Biology*, 13:pp. 69–76.
- Cox, B. (1971). *Hydrofoil Theory for Vertical Water Entry*. PhD thesis, Department of Naval Architecture, MIT.
- Cox, G. (1968). Supercavitating propeller theory - the derivations of induced velocity. In *The 7th Symposium on Naval Hydrodynamics*, Rome.
- Cumming, R. A., Morgan, W. B., and Boswell, R. J. (1972). Highly skewed propellers. In *Transactions*. Society of Naval Architects and Marine Engineers.

- Dobrovol'skaya, Z. N. (1969). On some problems of similarity flow of fluid with a free surface. *Journal of Fluid Mechanics*, 36:pp. 805–829.
- Dyson, P. K. (2000). *The Modelling, Testing and Design, of a Surface Piercing Propeller Drive*. PhD thesis, Department of Mechanical and Marine Engineering, Plymouth University.
- Dyson, P. K., Chudley, J., and Grieve, D. (2000). An experimental programme to determine the mean and time varying loads imposed by surface piercing propellers. Sydney. Sea Australia 2000.
- Falch, S. (1994). Slamming of flat-botomed bodies calculated with exact free surface boundary conditions. *Naval Hydrodynamics*, pages pp. 251–267.
- Fine, N. and Kinnas, S. (1993). The nonlinear numerical prediction of unsteady sheet cavitation for propellers of extreme geometry. In *Sixth International Conference On Numerical Ship Hydrodynamics*, pages 531–544, University of Iowa, Iowa.
- Fine, N. E. (1992). *Nonlinear Analysis of Cavitating Propellers in Nonuniform Flow*. PhD thesis, Department of Ocean Engineering, MIT.
- Fontaine, E. and Cointe, R. (1997). Asymptotic theories of incompressible water entry. In *AGARD Report 827*, Kiev, Ukraine. High Speed Body Motion in Water.
- Foster, T. (1989). Coated propellers: Reducing the current demand of ships. *Materials Performance*, 28(3):pp. 21–26.

- Franc, J. and Michel, J. (1985). Attached cavitation and the boundary layer: Experimental investigation and numerical treatment. *Journal of Fluid Mechanics*, vol. 154:pp 63–90.
- Furuya, O. (1975a). Nonlinear calculation of arbitrarily shaped supercavitating hydrofoils near a free surface. *Journal of Fluid Mechanics*, vol. 68:pp 21–40.
- Furuya, O. (1975b). Three-dimensional theory on supercavitating hydrofoils near a free surface. *Journal of Fluid Mechanics*, 71:pp. 339–359.
- Furuya, O. (1984). A performance prediction theory for partially submerged ventilated propellers. In *Fifteenth Symposium on Naval Hydrodynamics*, Hamburg, Germany.
- Furuya, O. (1985). A performance prediction theory for partially submerged ventilated propellers. *Journal of Fluid Mechanics*, 151:pp. 311–335.
- Geurst, J. and Timman, R. (1956). Linearized theory of two-dimensional cavitation flow around a wing section. *IX International Congress of Applied Mechanics*.
- Greeley, D. and Kerwin, J. (1982). Numerical methods for propeller design and analysis in steady flow. *Trans. SNAME*, vol 90.
- Griffin, P., Kosal, M., and Kinnas, S. (1998). User's manual for MPUF-3A v. 1.0-mid-chord cavity detachment. Technical Report No. 98-2, Ocean Engineering Group, UT Austin.

- Hadler, J. and Hecker, R. (1968). Performance of partially submerged propellers. In *The 7th ONR Symposium on Naval Hydrodynamics*, Rome, Italy.
- Hecker, R. (1973). Experimental performance of a partially submerged propeller in inclined flow. Lake Buena Vista, FL. SNAME Spring Meeting.
- Jessup, S. (1990). Measurement of multiple blade rate unsteady propeller forces. Technical Report DTRC-90/015, David Taylor Research Center.
- Jessup, S. (1996). private communication.
- Jessup, S., Berberich, W., and Remmers, K. (1994). Cavitation performance evaluation of naval surface ship propellers with standard and advanced blade sections. In *Twentieth Symposium on Naval Hydrodynamics*, pages 101–116, University of California, Santa Barbara.
- Jiang, C. and Leehey, P. (1977). A numerical method for determining forces and moments on supercavitating hydrofoils of finite span. In *Second Int'l Conf. Numer. Ship Hydrodynamics*, Berkeley.
- Kamiirisa, H. and Aoki, D. (1994). Development of supercavitating propeller for outboard motors. In *Second International Symposium on Cavitation*, Tokyo, Japan.
- Kato, H. (1996). *Cavitation*, chapter 5, pages 233–277. Computational Mechanics Publications. in *Advances in Marine Hydrodynamics*.

- Kehr, Y. Z. (1999). On the development of a new-series of propeller for high-speed crafts. In *Fifth International Conference on FAST Sea Transportation*, Seattle, Washington.
- Kerwin, J., Kinnas, S., Wilson, M., and McHugh, J. (1986). Experimental and analytical techniques for the study of unsteady propeller sheet cavitation. In *Proceedings of the Sixteenth Symposium on Naval Hydrodynamics*, pages 387–414, Berkeley, California.
- Kerwin, J. and Lee, C.-S. (1978). Prediction of steady and unsteady marine propeller performance by numerical lifting-surface theory. *Trans. SNAME*, vol 86.
- Kikuchi, Y., Kato, H., Yamaguchi, H., and Maeda, M. (1994). Study on a supercavitating foil. In *Second International Symposium on Cavitation*, pages 127–132, Tokyo, Japan.
- Kim, Y.-G. and Lee, C.-S. (1996). Prediction of unsteady performance of marine propellers with cavitation using surface-panel method. In *21st Symposium on Naval Hydrodynamics*, Trondheim, Norway.
- Kim, Y.-G., Lee, C.-S., and Suh, J.-C. (1994). Surface panel method for prediction of flow around a 3-d steady or unsteady cavitating hydrofoil. In *Second International Symposium on Cavitation*, pages 113–120, Tokyo, Japan.
- Kinnas, S. (1985). Non-linear corrections to the linear theory for the prediction of the cavitating flow around hydrofoils. Technical Report 85-10, MIT, Department of Ocean Engineering.

- Kinnas, S. (1991). Leading-edge corrections to the linear theory of partially cavitating hydrofoils. *Journal of Ship Research*, 35(1):pp. 15–27.
- Kinnas, S. (1992). A general theory for the coupling between thickness and loading for wings and propellers. *Journal of Ship Research*, 36(1):pp. 59–68.
- Kinnas, S. (1998). Prediction of unsteady sheet cavitation. In *Third International Symposium on Cavitation*, pages 19–36, Grenoble, France.
- Kinnas, S., Choi, J., Lee, H., and Young, J. (2000). Numerical cavitation tunnel. In *NCT50, International Conference on Propeller Cavitation*, Newcastle upon Tyne, England.
- Kinnas, S. and Fine, N. (1989). Theoretical prediction of the midchord and face unsteady propeller sheet cavitation. In *Proceedings of the Fifth International Conference on Numerical Ship Hydrodynamics*, Hiroshima, Japan.
- Kinnas, S. and Fine, N. (1990). Non-Linear Analysis of the Flow Around Partially or Super-Cavitating Hydrofoils by a Potential Based Panel Method. In *Proceedings of the IABEM-90 Symposium of the International Association for Boundary Element Methods*, pages 289–300, Rome, Italy.
- Kinnas, S. and Fine, N. (1992). A nonlinear boundary element method for the analysis of unsteady propeller sheet cavitation. In *Nineteenth Symposium on Naval Hydrodynamics*, pages 717–737, Seoul, Korea.

- Kinnas, S. and Fine, N. (1993). A numerical nonlinear analysis of the flow around two- and three-dimensional partially cavitating hydrofoils. *Journal of Fluid Mechanics*, 254:151–181.
- Kinnas, S. and Hsin, C.-Y. (1992). A boundary element method for the analysis of the unsteady flow around extreme propeller geometries. *AIAA Journal*, 30(3):688–696.
- Kinnas, S., Kosal, E., and Young, J. (1999). Computational techniques for the design and analysis of super-cavitating propellers. In *FAST'99 - 5th International Conference on Fast Sea Transportation*, Seattle, WA.
- Kinnas, S. and Mazel, C. (1992). Numerical vs. experimental cavitation tunnel (a supercavitating hydrofoil experiment). In *23rd American Towing Tank Conference*, University of New Orleans.
- Kinnas, S., Mishima, S., and Brewer, W. (1994). Nonlinear analysis of viscous flow around cavitating hydrofoils. In *Twentieth Symposium on Naval Hydrodynamics*, pages 446–465, University of California, Santa Barbara.
- Kinnas, S. and Pyo, S. (1999). Cavitating propeller analysis including the effects of wake alignment. *Journal of Ship Research*, 43(1):pp. 38–47.
- Kosal, E. (1999). Improvements and enhancements in the numerical analysis and design of cavitating propeller blades. Master's thesis, UT Austin, Dept. of Civil Engineering. Also, UT Ocean Eng. Report 99-1.

- Kruppa, C. F. L. (1992). Testing surface piercing propellers. In *Hydrodynamics : Computations, Model Tests, and Reality*, pages pp. 107–113.
- Kudo, T. and Kinnas, S. (1995). Application of vortex/source lattice method on supercavitating propellers. In *24th American Towing Tank Conference*, College Station, TX.
- Kudo, T. and Ukon, Y. (1994). Calculation of supercavitating propeller performance using a vortex-lattice method. In *Second International Symposium on Cavitation*, pages 403–408, Tokyo, Japan.
- Lauterborn, W. and Bolle, H. (1975). Experimental investigations of cavitation-bubble collapse in neighborhood of a solid boundary. *Journal of Fluid Mechanics*, 72:pp. 391–&.
- Lee, C.-S. (1979). *Prediction of Steady and Unsteady Performance of Marine Propellers with or without Cavitation by Numerical Lifting Surface Theory*. PhD thesis, M.I.T., Department of Ocean Engineering.
- Lee, C.-S., Kim, Y.-G., and Lee, J.-T. (1992). A potential-based panel method for the analysis of a two-dimensional super- or partially- cavitating hydrofoil. *Journal of Ship Research*, 36(2):pp. 168–181.
- Lee, H., Gu, H., Kakar, K., and Kinnas, S. (2001). MPUF-3A (version 2.0) user's manual and documentation. Technical Report No. 01-5, Ocean Engineering Group, UT Austin.

- Lee, H. and Kinnas, S. (2001a). Modeling of unsteady blade sheet and developed tip vortex cavitation. In *CAV 2001: Fourth International Symposium on Cavitation*, Pasadena, CA. California Institute of Technology.
- Lee, H. and Kinnas, S. (2001b). MPUF-3A (version 1.2) user's manual and documentation. Technical Report No. 01-2, Ocean Engineering Group, UT Austin.
- Lee, H. and Kinnas, S. (2002). Fully unsteady wake alignment for propellers in non-axisymmetric flows. Submitted for publication.
- Lee, H. S. (2002). *Modeling of Developed Tip Vortex Cavitation and Unsteady Wake Alignment*. PhD thesis, Department of Civil Engineering, The University of Texas at Austin.
- Leehey, P. (1971). Supercavitating hydrofoil of finite span. In *IUTAM Symposium on Non-Steady Flow of Water at High Speeds*, pages 277–298, Leningrad.
- Lemonnier, H. and Rowe, A. (1988). Another approach in modelling cavitating flows. *Journal of Fluid Mechanics*, vol 195.
- Lin, M. C. and Ho, T. Y. (1994). Water-entry for a wedge in arbitrary water depth. *Engineering Analysis with Boundary Elements*, 14:pp. 179–185.
- Makie, A. (1969). The water entry problem. *Q. J. Mech. Appl. Maths.*, 22:pp. 1–17.
- Matsuda, N., Kurobe, Y., Ukon, Y., and Kudo, T. (1994). Experimental investigation into the performance of supercavitating propellers. *Papers of Ship Research Institute*, 31(5).

- Miller, W. and Szantyr, J. (1998). Model experiments with surface piercing propellers. *Ship Technology Research*, 45:pp. 14–21.
- Mishima, S. and Kinnas, S. (1997). Application of a numerical optimization technique to the design of cavitating propellers in non-uniform flow. *Journal of Ship Research*, 41(2):pp. 93–107.
- Mishima, S., Kinnas, S., and Egnor, D. (1995). The CAVitating PROpeller EXperiment (CAPREX), Phases I & II. Technical report, Department of Ocean Engineering, MIT.
- Morgan, W. (1966). The testing of hydrofoils for fully-cavitating or ventilated operations. In *The 11th ITTC*, Tokyo, Japan.
- Morino, L. and Kuo, C.-C. (1974). Subsonic Potential Aerodynamic for Complex Configurations : A General Theory. *AIAA Journal*, vol 12(no 2):pp 191–197.
- Mueller, A. (1998). Development of face and mid-chord cavitation models for the prediction of unsteady cavitation on a propeller. Master's thesis, UT Austin, Dept. of Civil Engineering.
- Mueller, A. and Kinnas, S. (1997). Cavitation predictions using a panel method. In *ASME Symposium on Marine Hydrodynamics and Ocean Engineering*, volume 14, pages 127–137, Dallas, TX.
- Mueller, A. and Kinnas, S. (1999). Propeller sheet cavitation predictions using a panel method. *Journal of Fluids Engineering*, 121:282–288.

- Nishiyama, T. (1970). Lifting line theory of supercavitating hydrofoil of finite span. *ZAMM*, 50:645–653.
- Oberembt, H. (1968). Zur bestimmung der instationären flügelkräfte bei einem propeller mit aus dem wasser herausschlagenden flügeln. Technical report, Inst. für Schiffbau der Universität Hamburg, Bericht Nr. 247.
- Olofsson, N. (1996). *Force and Flow Characteristics of a Partially Submerged Propeller*. PhD thesis, Department of Naval Architecture and Ocean Engineering, Chalmers University of Technology, Göteborg, Sweden.
- Olofsson, N. (2001). Letter to the author and dr. s. a. kinnas.
- Parson, C. A. (1897). The application of the compound steam turbine to the purpose of marine propulsion. *Transactions of Institute of Naval Architecture*, 38.
- Peck, J. G. and H., M. D. (1974). Inclined-shaft propeller performance characteristics. Technical Report Report 4127, Naval Ship Research and Development Center.
- Pellone, C. and Peallat, J. (1995). Non-linear analysis of three-dimensional partially cavitating hydrofoil. In *CAV'95 International Symposium on Cavitation*, pages 433–440, Deauville, France.
- Pellone, C. and Rowe, A. (1981). Supercavitating hydrofoils in non-linear theory. In *Third International Conference on Numerical Ship Hydrodynamics*, Paris, France. Basin d'essais des Carènes.

- Rains, D. A. (1981). Semi-submerged propellers for monohull displacement ships. In *Propeller '81 Symposium*, pages pp. 15–40, Virginia Beach, VA. Society of Naval Architects and Marine Engineers.
- Reynolds, O. (1873). *Transactions of Institute of Naval Architecture*, 1:pp. 56.
- Reynolds, O. (1874). On the effect of immersion on screw propellers. *Transactions of Institute of Naval Architecture*, 2.
- Riabouchinsky, D. (1926). On some cases of two-dimensional fluid motion. In *Proceedings of London Math Society*, number 25, pages pp. 185–194.
- Rose, J. C. and Kruppa, C. F. L. (1991). Surface piercing propellers - methodical series model test results. In *FAST'91*, Norway.
- Rose, J. C., Kruppa, C. F. L., and Koushan, K. (1993). Surface piercing propellers - propeller/hull interaction. In *FAST'93*, pages pp. 867–881, Japan.
- Roshko, A. (1955). On the wake and drag of bluff bodies. *Journal of the Aeronautical Sciences*, 22:pp. 124–132.
- Russel, A. (1958). Aerodynamics of wakes, existence of unsteady cavities. *Engineering*, 186:pp. 701–702.
- Savineau, C. and Kinnas, S. (1995). A numerical formulation applicable to surface piercing hydrofoils and propellers. In *24th American Towing Tank Conference*, Texas A&M University, College Station, TX.

- Scherer, J. (1977). Partially submerged and supercavitating propellers. In *The 18th ATTC*, Annapolis.
- Shen, Y. (1975). General scaling problems on fully cavitating and ventilated flows. In *The 17th ATTC*, Pasadena.
- Shiba, H. (1953). Air-drawing of marine propellers. Technical Report 9, Transportation Technical Research Institute.
- Suhrbier, K. and Lecoffre, Y. (1986). Investigation of the influences of test techniques, water speed and nuclei seeding on the characteristics of a high speed model propeller in a cavitation tunnel and correlation with full scale measurements. In *International Symposium on Cavitation*, Sendai, Japan.
- Tabbara, M., Blacker, T., and Belytschko, T. (1994). Finite element derivative recovery by moving least squares interpolants. *Computational Methods in Applied Mechanical Engineering*, 117:pp. 211–223.
- Tachmindji, A. J. and Morgan, W. B. (1958). The design and estimated performance of a series of supercavitating propellers. In *Proceedings of the Second Office of Naval Research Symposium on Naval Hydrodynamics*, pages pp. 489–532.
- Tachnimdji, A. and Morgan, W. (1958). The design and estimated performance of a series of supercavitating propellers. In *The Second Office of Naval Research Symposium on Naval Hydrodynamics, ACR-38*, pages pp. 489–532.
- Treadgold, D., Jones, A., and Wilson, K. (1979). Pressure distribution measured in the rae 8ft * 6ft transonic wind tunnel on rae 'a' in combination with an ax-

- isymmetric body at mach numbers of 0.4, 0.8 and 9.9. Technical Report AR-138, AGARD.
- Tulin, M. (1953). Steady two-dimensional cavity flows about slender bodies. Technical Report 834, DTMB.
- Tulin, M. (1955). Supercavitating flow past foils and struts. In *Symposium on Cavitation in Hydrodynamics*, NPL, Tendington, England.
- Tulin, M. (1980). An analysis of unsteady sheet cavitation. In *The 19th ATTC Conference*, pages pp. 1049–1079.
- Tulin, M. B. (1962). Supercavitating propellers - history, operating characteristics, mechanisms of operation. In *Fourth Symposium on Naval Hydrodynamics*, pages pp. 239–286.
- Uhlman, J. (1978). A partially cavitating hydrofoil of finite span. *Journal of Fluids Engineering*, 100(3):pp. 353–354.
- Uhlman, J. (1987). The surface singularity method applied to partially cavitating hydrofoils. *Journal of Ship Research*, vol 31(No. 2):pp. 107–124.
- Uhlman, J. (1989). The surface singularity or boundary integral method applied to supercavitating hydrofoils. *Journal of Ship Research*, vol 33(No. 1):pp. 16–20.
- Ukon, Y., Kudo, T., Kurobe, Y., Matsuda, N., and Kato, H. (1995). Design of high performance supercavitating propellers based on a vortex lattice method.

- In *An International Conference on Propeller Cavitation (PROPCAV '95)*, The University of Newcastle Upon Tyne, England, U.K.
- Van Houten, R. (1982). The numerical prediction of unsteady sheet cavitation on high aspect ratio hydrofoils. In *14th Symposium on Naval Hydrodynamics*.
- Venning, E. and Haberman, W. L. (1962). Supercavitating and propeller performance. *Transactions of SNAME*, 70:pp. 354–417.
- Villat, H. (1914). Sur la validité des solutions de certain problem d'hydrodynamique. *Journal de Mathematiques*, vol 6(No. 10):pp 231–290.
- Von Karman, T. (1929). The impact of seaplane floats during landing. Technical report, NACA TN321.
- Vorus, W. and Mitchell, K. (1994). Engineering of power boat propellers. In *Propellers/Shafting '94 Symposium*, pages 1–16 (paper No. 12), Virginia Beach, VA. Society of Naval Architects & Marine Engineers.
- Vorus, W. S. and Chen, L. (1987). An extension of the 'malkus hypothesis' to the turbulent base flow of blunt sections. *Journal of Fluid Mechanics*, 184:pp. 551–569.
- Wagner, H. (1932). Über stoss- und gleitvorgänge an der oberfläche von flüssigkeiten. *Z. Angew. Math. Mech.*, 12(4):pp. 192–215.
- Wang, D. (1977). Water entry and exit of a fully ventilated foil. *Journal of Ship Research*, 21:pp. 44–68.

- Wang, D. (1979). Oblique water entry and exit of a fully ventilated foil. *Journal of Ship Research*, 23:pp. 43–54.
- Wang, G., Jia, D., and Sheng, Z. (1990a). Hydrodynamic performance of partially submerged ventilated propeller. *Shipbuilding of China*, (2).
- Wang, G., Jia, D., and Sheng, Z. (1992). Study on propeller characteristics near water surface. In *The 2nd Symposium on Propeller and Cavitation*, pages pp. 161–168, Hangzhon, China.
- Wang, G., Zhu, X., and Sheng, Z. (1990b). Hydrodynamic forces of a three-dimensional fully ventilated foil entering water. *Journal of Hydrodynamics*, 5(2).
- Wang, S. Y. (1995). *Systemtische Analyse von Modellversuchen mit teilgetauchten Propellern*. PhD thesis, Technischen Unversitaet Berlin (D83).
- Widnall, S. (1966). Unsteady loads on supercavitating hydrofoils. *Journal of Ship Research*, 9:pp. 107–118.
- Wu, T. and Wang, D. (1964). A wake model for free-streamline flow theory. part 2. cavity flows past obstacles of arbitrary profile. *Journal of Fluid Mechanics*, vol 18:pp 65–93.
- Yim, B. (1974). Linear theory on water entry and exit problems of a ventilating thin wedge. *Journal of Ship Research*, 18(1):pp. 1–11.
- Yim, B. (1976). Optimum propellers with cavity-drag and frictional drag effects. *Journal of Ship Research*, Volume 20.

- Yim, B. and Higgins, L. (1975). A nonlinear design theory for supercavitating cascades. In *ASME Cavity Flow Symposium*, pages pp. 85–94.
- Young, Y. and Kinnas, S. (2001). A BEM for the prediction of unsteady midchord face and/or back propeller cavitation. *Journal of Fluids Engineering*.
- Young, Y., Lee, H., and Kinnas, S. (2001a). PROPCAV (version 1.2) user's manual and documentation. Technical Report No. 01-4, Ocean Engineering Group, UT Austin.
- Young, Y., Lee, H., and Kinnas, S. (2001b). PROPCAV (version 2.0) user's manual and documentation. Technical Report No. 01-7, Ocean Engineering Group, UT Austin.
- Zhao, R. and Faltinsen, O. (1993). Water entry of two-dimensional bodies. *Journal of Fluid Mechanics*, 246:pp. 593–612.
- Zhao, R. and Faltinsen, O. (1998). Water entry of axisymmetric bodies with and without flow separation. In *22nd Symposium on Naval Hydrodynamics*, Washington, D.C.

Vita

Yin Lu Young was born in Canton, China on September 4, 1975. She is the daughter of Kwan Luk and Kam Lin Young. She moved with her family to Oahu, Hawaii on March 8, 1987. She graduated from Castle High School in 1993. She attended University of Southern California from 1993-1996 and received a B.S. in Civil Engineering. She enrolled at The University of Texas at Austin in 1996, where she completed her M.S. in Civil Engineering with emphasis on Structural Engineering in 1998. She continued at The University of Texas at Austin for her doctoral study in the Ocean Engineering Group at the Civil Engineering Department.

Permanent address: 47-403A Ahuimanu Road
Kaneohe, Hi 96744

This dissertation was typeset with L^AT_EX[†] by the author.

[†]L^AT_EX is a document preparation system developed by Leslie Lamport as a special version of Donald Knuth's T_EX Program.